ADSORPTION OF METHANE REFORMER OFF-GAS COMPONENTS IN A COLUMN PACKED WITH Cu, Al, Ti AND Zn BASED ORGANIC FRAMEWORKS

A Thesis Submitted to
the Graduate School of Engineering and Sciences of
İzmir Institute of Technology
in Partial Fulfillment of the Requirements for the Degree of

MASTER OF SCIENCE

in Chemical Engineering

by
Gaye KANALTI

December 2016
İZMİR

We approve the thesis of **Gaye KANALTI**

Examining Committee Members:

_____
Prof. Dr. Fehime ÇAKICIOĞLU ÖZKAN
Department of Chemical Engineering, İzmir Institute of Technology

_____
Prof. Dr. Mehmet POLAT
Department of Chemical Engineering, İzmir Institute of Technology

_____
Prof. Dr. Şerife Şeref HELVACI
Department of Chemical Engineering, Ege University

30 December 2016

_____
Prof. Dr. Fehime ÇAKICIOĞLU ÖZKAN
Supervisor, Department of Chemical
Engineering
İzmir Institute of Technology

_____   _____
Prof. Dr. Fehime ÇAKICIOĞLU ÖZKAN   **Prof. Dr. Bilge KARAÇALI**
Head of the Department of Chemical   Dean of the Graduate School of
                                                      Engineering and Sciences

ACKNOWLEDGEMENTS

ABSTRACT

ADSORPTION OF METHANE REFORMER OFF-GAS COMPONENTS IN A COLUMN PACKED WITH Cu, Al, Ti AND Zn BASED ORGANIC FRAMEWORKS

Within the past decade, CO_2 emissions from fossil fueled power plants has accelerated rapidly as a result of the increase in energy consumption associated with industrial development all over the world. Beyond the necessity of reduction in CO_2 emissions, concerning on the crude oil reserves depletion induced the urgent need of transition to more efficient, renewable, cleaner and cheaper fuel, hydrogen. In the world, most of the hydrogen is produced by hydrogen-rich stream methane reformer (SMR) off gas streams composed of 80-60% H_2, 15-25% CO_2, 3-6% CH_4 and 1-3% CO, thereby separation of SMR components became more of an issue. In this study, adsorption based separation of SMR components were investigated in a column packed with copper (CuTPA, (S_{Lang}: 776 m^2g^{-1})), aluminum (AlTPA, (S_{Lang}: 1330 m^2g^{-1})), titanium (TiTPA, (S_{Lang}: 1835 m^2g^{-1})) and zinc (ZnTPA, (S_{Lang}: 1023 m^2g^{-1})) based organic frameworks (MOFs). The pure gas adsorption studies on equimolar CO_2/H_2, CH_4/H_2 and CO/H_2 systems and the equimolar mixture of CO_2/CH_4 system were carried out and the experimental breakthrough curves were obtained at three different feed flow rates (10, 20 and 30 mL/min) at three column pressure (1, 5 and 10 bar) at 303 K. The highest adsorption capacities of all MOFs were achieved at 30 mL/min of feed rate and 10 bar operating pressure, at these conditions the non-adsorptive behavior of hydrogen on the aforementioned MOFs was ensured. The amounts of CO_2 adsorbed were calculated as 1.61, 5.54, 5.20 and 2.11 mmolCO_2/g, while adsorbed CH_4 amounts were 1.50, 3.16, 3.25 and 1.90 mmol CH_4/g and the adsorbed CO amounts were 1.47, 2.59, 1.91 and 1.83 mmol CO/g on CuTPA, AlTPA, TiTPA and ZnTPA, respectively. The highest selectivity for CO_2 over CH_4 was attained on TiTPA as 8.0 at 10 mL/min feed rate of CO_2/CH_4 mixture at atmospheric column pressure and 303 K. The experimental adsorption isotherms of SMR components were fitted well with Langmuir and virial models and the best fitted model parameters were evaluated for each MOF.

ÖZET

METAN REFORMER ÇIKIŞ GAZI BİLEŞENLERİNİN Cu, Al, Ti VE Zn TEMELLİ ORGANİK KAFES YAPILARI İLE DOLGULU KOLONDA ADSORPSİYONU

Son on yıl içinde, enerji santrallerinden salınan CO_2 miktarı endüstriyel gelişmelere bağlı olarak artan enerji tüketiminin sonucunda dünya çapında hızla yükselmiştir. CO_2 salınımın azaltılması gerekliliğinin yanı sıra, ham petrol kaynaklarındaki düşüş daha verimli, temiz ve ucuz yenilenebilir yakıt olan hidrojene geçişi zorunlu bir hale getirmiştir. Dünya çapında, hidrojen genellikle hidrojence zengin, 80-60% H_2, 15-25% CO_2, 3-6% CH_4 ve 1-3% CO oranlarındaki metan reformer (SMR) çıkış gazı akımlarından üretilmektedir, bundan dolayı SMR bileşenlerinin ayrılması önem arz etmektedir. Bu çalışmada, adsorpsiyon yöntemi ile SMR gazı bileşenlerinin ayrıştırılması bakır (CuTPA, (S_{Lang}: 776 m^2g^{-1})), alüminyum (AlTPA, (S_{Lang}: 1330 m^2g^{-1})), titanyum (TiTPA, (S_{Lang}: 1835 m^2g^{-1})) ve çinko temelli organik kafes yapıları (MOFs) ile doldurulmuş kolonda incelenmiştir. Saf bileşen adsorpsiyon çalışmaları eş molar CO_2/H_2, CH_4/H_2 ve CO/H_2 sistemleri üzerinde ve ikili gaz karışım çalışmaları CO_2/CH_4 sistemi üzerinde üç farklı besleme hızında (10, 20 ve 30 mL/dk) ve üç farklı kolon basıncında (1, 5 ve 10 bar) ve 303 K' de elde edilen salınım eğrileri ile gerçekleştirilmiştir. Bütün MOF' ların en yüksek adsorplama kapasitesine 30 mL/dk besleme hızında ve 10 bar kolon basıncında ulaştığı, bu koşullarda hidrojenin sözü edilen MOF' lar üzerinde adsorplanmadığı kesinleştirilmiştir. CuTPA, AlTPA, TiTPA ve ZnTPA tarafından adsorplanan CO_2 miktarları sırasıyla 1.61, 5.54, 5.20 ve 2.11 $mmolCO_2/g$ olarak hesaplanırken, CH_4 miktarları 1.50, 3.16, 3.25 ve 1.90 mmol CH_4/g ve CO miktarları ise 1.47, 2.59, 1.91 ve 1.83 mmol CO/g olarak bulunmuştur. CO_2' in CH_4 üzerindeki en yüksek seçimli adsorpsiyonu TiTPA üzerinde 8 olarak 10 mL/dk akış hızında atmosfer basıncında 303 K' de ulaşılmıştır. SMR bileşenlerinin deneysel adsorpsiyon izotermleri Langmuir ve virial modellerle uyuşmuş ve en uygun model parametreleri her bir MOF için değerlendirilmiştir.

TABLE OF CONTENTS

LIST OF FIGURES

LIST OF TABLES

CHAPTER 1

INTRODUCTION

In recent years, the large scale emission of CO_2 has accelerated rapidly due to increasing population and energy consumption associated with industrial development all over the world. Flue gases from fossil fueled power plants, industrial processes and transportation are major sources of CO_2 emissions to the atmosphere and are responsible for accumulation of greenhouse gases consequently resulted in global climate change (Davison 2007, Ipcc 2014, Dechamps and Pilavachi 2004). Especially, flue gas from fossil fuel based power plants discharges around 40% of total CO_2 into the atmosphere annually and plays important role in long-term global average temperature rise up to 2.4° C by 2050 (IEA 2010).

Beyond the necessity of reduction in the CO_2 emission, nowadays one of the greatest challenge facing the mankind involves the critical acceleration in the crude oil reserves depletion and difficulties in their extraction and processing, leading to a great cost increase (Benes et al. 2015, Miller and Sorrell 2014). Consequently, the dynamics of relationship between politics and economy could be greatly distressed and ascending concerns on the "energy security" and "energy independence" concepts may become the foremost issue throughout the world, potentially resulted in global energy crisis (Littlefield 2013, Frankel 2013, Zou et al. 2016). To this respect, making transition to a future of more efficient, renewable, cleaner and cheaper fuel is an urgent need. Such a fuel is hydrogen that is considered as "fuel of future" (Edwards et al. 2008, Nowotny et al. 2005, Jain 2009) due to ideal alternative energy carrier nature with high conversion efficiency, lightweight, environmental and climatic cleanness and great abundance (Winter 2009, Oriňáková and Oriňák 2011). A typical flue gas of steam methane reformer (SMR), consists of 15–25% CO_2, 3–6% CH_4, 1–3% CO (Sircar and Golden 2000), is the largest and generally the most economical way of hydrogen production (Armor 1999) resulted in hydrogen rich (70-80 %) off-gas (Sircar and Golden 2000). The focus of attention regarding both environmental and energy-related concerns, upgrading flue gas is the key strategy for conversion of waste gas into high purity-useful components (Agarwal, Biegler, and Zitney 2010), therefore the technologies for separation/purification of off-gas streams has become more of an issue.

To date, the separation/purification of gas streams have been carried out through absorption, cryogenic distillation, membrane separation and adsorption. Among these technologies, adsorption based gas separation by porous solid adsorbents received great attention due to its less energy intensive nature and hence of comparatively low operating cost, high efficiency with ease of application (Wang et al. 2011, Wiersum et al. 2013, Songolzadeh, Soleimani, and Takht Ravanchi 2015, Ferreira et al. 2015, Rada et al. 2015). Porous solids including zeolites and activated carbons have been widely used for adsorption based separation and purification of gas mixtures (Sircar, Golden, and Rao 1996, Esteves et al. 2008, Grande et al. 2013, Kacem, Pellerano, and Delebarre 2015, Álvarez-Gutiérrez et al. 2016, Bacsik et al. 2016, Sigot et al. 2016). Within the past decades, great deal of research effort has been focused on the development of a new class of coordination polymers named Metal Organic Frameworks (MOFs) recognized as a promising alternative to the conventional adsorbents. MOFs are highly ordered crystalline materials composed of metal centers linked by organic ligands with extraordinary versatility in different coordination numbers and geometries (Yaghi et al. 1998, Batten 1998, Kitagawa, Kitaura, and Noro 2004, Rowsell and Yaghi 2004, Hill et al. 2005, Cheetham, Rao, and Feller 2006). Owing to their tunable structural properties, structural regularity combined with functionality, high surface areas, high porosity and volume, and open metal sites make these robust MOFs attractive for many potential applications in adsorption based gas storage and separation (Ferey et al. 2003, Wiersum et al. 2013, Anbia and Sheykhi 2012, Peter et al. 2013, Yang, Sitprasert, et al. 2015, Abid et al. 2016) , catalysis (Ferey 2008, Czaja, Trukhan, and Muller 2009, Chughtai et al. 2015), drug delivery (Huxford, Rocca, and Lin 2010, Keskin and Kızılel 2011, Ahmad et al. 2015), water treatment (Dias and Petit 2015, Li et al. 2016, Luo et al. 2017), sensing (Kumar, Deep, and Kim 2015, Ren and Lu 2015, Liu and Yin 2016) and electrochemical energy storage (Ke, Wu, and Deng 2015, Wang, Han, et al. 2016, Zhao et al. 2016).

Although great number of studies were conducted on different synthesis routes and effect of synthesis parameters on the morphological and structural properties of MOFs, but the works related to the adsorption of SMR components in pure forms and in binary mixtures on MOF materials are very scarce. The objective of the study was to investigate the adsorption of pure SMR components (CO_2, CH_4 and CO) in CO_2/H_2, CH_4/H_2 and CO/H_2 streams and the binary mixture of CO_2/CH_4 on four different MOFs: copper based MOF (CuTPA), aluminum based MOF (AlTPA), titanium based MOF (TiTPA) and zinc based MOF (ZnTPA) at room temperature up to 10 bar.

In this study following chapters comprise information on the MOFs (Chapter 2), followed by adsorption based gas separation and purification processes (Chapter 3), experimental studies conducted in this thesis (Chapter 4), results and discussions (Chapter 5), and followed by the conclusions (Chapter 6).

CHAPTER 2

METAL ORGANIC FRAMEWORKS (MOFs)

2.1. Structure and Properties of MOFs

The intense current interest has been directed toward the synthetic approaches to the assembly of coordination complexes; inorganic metal clusters and organic ligand. Metal organic frameworks (MOFs), also referred as "porous coordination polymers" (Kitagawa, Kitaura, and Noro 2004, Ling et al. 2011, Safarifard and Morsali 2015), are crystalline materials which constituted by a tridimensional array of metal ions or clusters linked by rigid organic ligands (Figure 2.1) that are typically di-, tridentate ligands such as BDC (TPA or BDC: 1,4-benzenedicarboxylic acid or terephthalate) and BTC (BTC: 1,3,5-benzenetricarboxylic acid). One of the most remarkable features of MOFs is that frequently their structural character, chemical, and physical properties can be controlled by the diversity of organic linkers and the coordination geometry of metal building blocks (Loiseau et al. 2005, Dhakshinamoorthy and Garcia 2014, Cui et al. 2015, Andirova et al. 2016). Hence, MOFs can be engineered to a large extent and can be synthesized by flexible rational design via controlling the architecture and functionalization of the pores for many potential applications.
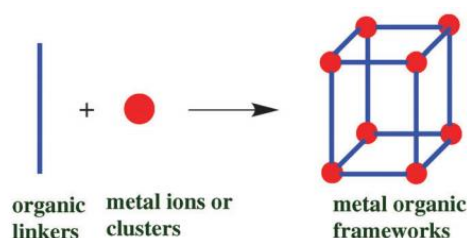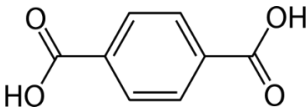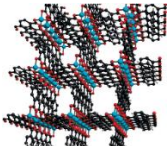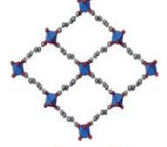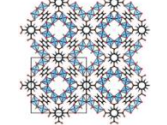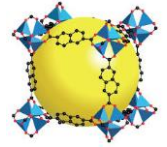
Figure 2.1. Illustration of the building blocks and structure of MOFs
(Source: adapted from Dhakshinamoorthy and Garcia (2014))

Most of metals used in the construction of the framework structures are d-block transition metals (Cu, Al, Ti, Zn, Fe, Co, Ni, Cr, Mn, Ag etc.) by virtue of d-block electrons demonstrating high functionality in complex forming capacity and acid-base

interactions (Sherif 1970, Kitagawa, Kitaura, and Noro 2004, Zhang, Yang, and Ma 2006, Ahmed and Jhung 2014, Cui et al. 2015). These metal ions can act as Lewis acid sites by binding with substrates or reagents resulted in improvement of the interactions between adsorbent and adsorbate (by acid-base interaction of π-complexation, and so on) (Ahmed and Jhung 2014, Dhakshinamoorthy and Garcia 2014). Table 2.1 illustrates the effect of metal selection on the MOF structures, composed of four different metal ions (Cu, Al, Ti and Zn) and BDC (TPA) as the common organic ligand. Furthermore, the geometry of the ligand and degree of flexibility is also important in construction of MOF structures. Various MOFs with different porosities and pore sizes can be created by altering the length of the organic linker (Seki and Mori 2002, Rosi et al. 2003, Cheetham, Rao, and Feller 2006, Hendon et al. 2013). Increasing the chain length of bridging ligands and adding functional groups can in principle lead to larger channels and pores, consequently resulted in MOFs with enhanced performances for specific applications, especially in gas separation and purification processes (Ma and Lin 2008, Rada et al. 2015, Abid et al. 2016).

Table 2.1. Effect of metal source on the MOF structures

MOFs	Metal sources	Organic linker	Structures	Ref.
CuTPA	$Cu(NO_3)_2 \cdot 3H_2O$			Carson et al. (2009)
AlTPA	$Al(NO_3)_3 \cdot 9H_2O$	BDC (1,4-benzenedicarboxylic acid)		Li et al. (2013)
TiTPA	$Ti(OiPr)_4$			Hendon et al. (2013)
ZnTPA	$Zn(NO_3)_2 \cdot 6H_2O$			Rosi et al. (2003)

2.2. Synthesis of MOFs

In the synthesis of MOFs two methods are adopted, namely conventional and unconventional methods. Solvothermal synthesis is conventional one, whereas electrochemical, mechanochemical, sonochemical and microwave-assisted syntheses are alternative unconventional pathways (Aaron 2012, Stock and Biswas 2012, Lee, Kim, and Ahn 2013). In literature, specific for each of synthesis routes, numbers of synthesis parameters that directly influence MOF properties have been studied in detail, but here only the general approaches to these synthesis methods were explained.

Conventional solvothermal methods are performed by electrical heating a mixture of organic linker and metal salt in a solvent system that usually contains formamide functionality (Tranchemontagne, Hunt, and Yaghi 2008). Additionally, hydrothermal synthesis eliminates the solvent necessity but the low solubility of organic ligands in water is the main challenge (Huang et al. 2003, Sanchez-Sanchez et al. 2015). Although both solvo/hydrothermal synthesis give good quality MOF crystals with high yield, they require thermally stable reactants and reaction times take from several hours to days (Lee, Kim, and Ahn 2013, Khan and Jhung 2015, Crane, Anderson, and Conway 2015).

As one of the unconventional methods, electrochemical synthesis of MOFs was first reported in 2005 by researchers at BASF (Mueller et al. 2006). An electrode is used as the metal source and placed in ligand solution under appropriate voltage to dissolve the metal salt and release metal ions. Immediate reaction of ions between linkers are observed and the MOF is formed in very short reaction times under milder conditions (Al-Kutubi et al. 2015, Yang, Du, et al. 2015). The solid-state approach to the synthesis of MOFs is the mechanochemical synthesis; mechanical breakage of intramolecular bonds by grinding or milling attain at room temperature under solvent-free conditions (Lee, Kim, and Ahn 2013). However, resulted MOFs with non-uniform crystals with different shapes attributing to crushing and grinding effects are still challenging (Singh, Hardi, and Balema 2013). In sonochemical synthesis, powerful ultrasound radiation (20 kHz-10 MHz) is applied to molecules causing a reaction to occur at very high local temperatures (~5000 K) and pressures (~1000 bar) (Lee, Kim, and Ahn 2013, Andirova et al. 2016). Even tough, this route resulted in high reaction rate and MOFs having fine small particle sizes, the sophisticated equipment is needed and generation of extremely hot spots makes this technology problematic to scale up (da Silva et al. 2016, Armstrong et al. 2017). Microwave-assisted approach is based on the interaction between applied

electric field and polar solvent causes rapid heating of liquid phase. Large heat generation caused by microwave provides energy to speed up the crystallization reaction. Although phase selectivity, narrow pore size distribution can be achieved by this method (Lee, Kim, and Ahn 2013), working with microwaves raises some concerns with respect to safety and reproducibility. The reproducibility greatly varies with the brand of the instrument and the size and geometry of the microwave cage, also even a slight change in reaction conditions can adversely affect the morphology and phase purity of MOFs (Klinowski et al. 2011).

2.3. Applications of MOFs

The crucial role of heterogeneous catalysis in many chemical processes is a clear fact in industry. However, the critical concern for catalytic processes is the shape and size selectivity which is typically controlled by porous nature of the catalyst. The highly ordered structure of MOFs provides uniform pores and porosity with unique structural and chemical features. MOFs having high surface areas and porosities offer very high density of fully exposed active sites per volume which resulted in enhanced activity and effective catalytic system (Ferey 2008, Czaja, Trukhan, and Muller 2009). Also, compared to zeolites MOFs can be constructed in much more chemical varieties with multi-functionality and flexibility. Therefore, use of MOFs in catalysis is increasing continuously. Chughtai et al. (2015) summarized the chemical reactions including aldol condensation, oxidation reactions, epoxide formation, hydrogenation, Suzuki coupling, ring-opening, alkylation of amines, cyclopropanation reactions, Friedel–Crafts reactions, cyclization reactions, Friedlander reaction, acetalization, hydroformylation, and polymerization where MOFs were used as catalyst.

Furthermore, MOFs displays many desired characteristics as drug carriers, comprising high surface areas and large pore sizes for controlled drug release (Keskin and Kızılel 2011) and drug encapsulation, and biodegradability as a result of relatively labile metal–ligand bonds for grafting of drug molecules. Huxford, Rocca, and Lin (2010) reviewed that the bulk MOF powders can absorb and release large amount of therapeutics including ibuprofen, procainamide, and nitric oxide. Besides, MOFs have been also investigated for biochemical and biomedical applications, including biomimetic catalysis,

biosensors, and in biomedicines, but issues related to the stability in a physiological environment and synthesizing biocompatible MOFs still present (Ahmad et al. 2015).

Access to clean freshwater become a key challenge for the upcoming decades. Water-stable MOFs are arising to be one of the most favorable adsorbents for water purification due to large number of active sites accompanied with high surface areas (Dias and Petit 2015, Li et al. 2016). Liquid- phase adsorption based performances of MOFs were reported for pollutants; heavy metal ions such as Hg^{2+}, Pb^{2+}, As^{3+}, Cd^{2+}, Ba^{2+} and Cr^{6+} (Luo et al. 2017, Li et al. 2016), aromatic compounds such as thiophene, pyrrole, nitrobenzene and naphthalene (Bhadra et al. 2015), organic dyes such as methyl orange, methylene blue and Rhodamine B (Dias and Petit 2015) and pharmaceuticals such as nitrofurazone and nitrofurantoin antibiotics, furosemide and sulfasalazine (Cychosz and Matzger 2010, Wang, Lv, et al. 2016).

Also, MOFs are considered an excellent candidate for sensor applications due to capability of detecting changes in luminescence by interaction of the analytes with a metal though chemical bonding and with ligands through host-guest chemistry (Kumar, Deep, and Kim 2015). Luminescent MOF-based sensing approaches include anion sensing for Hg^{2+}, Cu^{2+}, Ag^{2+}, Zn^{2+} and Fe^{2+}/Fe^{3+} ions, explosive molecule sensing for 2,4-dinitrotoluene (DNT) and 2,4,6-trinitrotoluene (TNT), gas detection for H_2S, O_2 and NH_3, HCl vapors, and biosensors for detecting nucleic acid, protein, antibody and enzyme (Ren and Lu 2015). Also, conductive MOFs can be used as electrochemical sensors in photonics and microelectronics as a consequence their tunable conductive nature (Kumar, Deep, and Kim 2015, Liu and Yin 2016).

In addition, MOFs have attracted increasing attention in clean energy applications; fuel cells, batteries and supercapacitors. MOFs can be directly used as electrocatalyst in fuel cells and as electrodes in lithium ion batteries (LIBs) and supercapacitors due to their large internal surface area and porosity that can favor electrochemical reaction, interfacial transport and provide short diffusion paths for ions. Metal ions in MOF structures act as redox active sites during electrochemical processes (Ke, Wu, and Deng 2015, Wang, Lv, et al. 2016), but the common issue is degree of electronic conductivity as a result of existence of organic linkers (Zhao et al. 2016).

Among all the potential application areas as mentioned above, the most advanced researches that have performed on MOFs used as adsorbents for adsorption based selective gas separation and purification processes. The separation of CO_2 from other

light gases such that from methane for natural gas purification and from flue gases has been highlighted for economic and environmental point of views. Using MOFs as adsorbents for adsorption of pure CO_2 component and mixtures involved with CO_2 (i.e., CO_2/CH_4) has become one of the most important topic in literature. The adsorption performance of MOFs; HKUST-1, MOF-2, MOF-505, MOF-74, IRMOF-11 and MOF-177 (Millward and Yaghi 2005), ZnDABCO (Mishra et al. 2012), MIL-53(Cu) (Anbia and Sheykhi 2013), Basolite A100 (Ferreira et al. 2015), MIL-53(Al) and MIL-96(Al) (Abid et al. 2016), MIL-125(Ti) and CeBTC (Mounfield Iii et al. 2016) were studied over wide range of pressure and temperature for selective CO_2 capture and storage. Moreover, hydrogen is regarded as alternative energy resource and consisted as a major fuel of the future for automotive sector instead of fossil fuels. However, the hydrogen-based energy cycles still suffers from purification and effective storage conditions. MOFs (HKUST-1, MOF-5, NOTT-112) presenting large pore volume and flexible structures is a promising candidate for H_2 adsorption, as well as H_2 storage at 77 K and elevated pressures (Sun et al. 2006, Yan et al. 2009, Lin et al. 2012). Additionally, the ability to separate hydrocarbons mixtures is an important technology in the petroleum and petrochemical industry, for the removal of impurities for fuel purification and the isolation of compounds for further reaction. In this respect, MOFs (UiO-66(Zr), HKUST-1, MIL-125(Ti), MIL-53 (Al, Cr)) with different pore structures and various degree of pore openings have studied many times for the selective separation of n-hexane and its branched isomers which are the superior Research Octane Numbers (RONs) of the dibranched for gasoline production. The selectivity towards n-hexane over branched isomers was found dominant for MOFs having one-dimensional pore (Trung et al. 2008, Ling et al. 2011, Ramsahye et al. 2014).

CHAPTER 3

ADSORPTION BASED GAS SEPARATION AND PURIFICATION

In this chapter, widely used gas separation and processes such that distillation, absorption and membrane based processes are compared to adsorption based processes. Following with brief information on adsorption phenomena, adsorption isotherm models which are vital for the understanding the adsorption process and quantitative knowledge of the adsorbate/adsorbent system are presented. Then, adsorption based gas separation processes carried out in adsorbent packed bed are mainly objected, dynamic behavior of the packed bed is examined. Traditional adsorbents such as silica gel, activated alumina and activated carbons are investigated in brief, followed by detailed literature review on copper, aluminum, titanium and zinc based MOFs used as adsorbents in gas separation and purification processes.

3.1. Gas Separation and Purification Processes

Because of its widespread applicability and scalability, distillation has assumed a dominant role in separation technology for years. Although the costs of and adsorption separation process and a distillation unit are comparable, much higher separation factors are commonly attainable in an adsorption system (Ruthven 1984). A comparison between distillation and adsorption in the chemical industries has been made by determination of relative volatility. The ease of separation by distillation is basically measured by relative volatility, for an ideal binary mixture is simply the ratio between the vapor pressures of the two components. Relative volatility of light component i over heavy component j, $\propto_{ij}$, is given in Equation 3.1 (Yang 1997, Skogestad 2008).

$$\propto_{ij} = \frac{p_i^0(T)}{p_j^0(T)} \tag{3.1}$$

Here, $p_i^0(T)$ and $p_j^0(T)$ is the pure component's saturated vapor pressures for light and heavy component, respectively. The criteria for when to use adsorption process become practical is the relative volatility at about 1.25 or less. In this case, the adsorption process becomes much more economic option. For purification processes involving light gases cryogenic distillation, which is liquefaction followed by distillation, is frequently used. But the cost comparison between cryogenic distillation and adsorption is much more favorable to adsorption even when the relative volatility is high (Ruthven 1984).

The principal necessity for an economic adsorption process relies on the adsorbent with sufficiently high selectivity, high capacity and life. Processes depending on equilibrium selectivity, the separation factor, $\propto_{AB}$, is defined as in Equation 3.2 (Ruthven 1984, Ruthven, Farooq, and Knaebel 1994, Wiersum et al. 2013).

$$\propto_{AB} = \frac{X_A/X_B}{Y_A/Y_B} \tag{3.2}$$

where X_A and Y_A are, respectively the mole fractions of component A in adsorbed and fluid phase at equilibrium. The separation factor is analogous to relative volatility, however two given components the relative volatility is constant whereas the separation factor varies depending on the adsorbent (Ruthven 1984, Yang 1997).

In addition to distillation, gas separation and capture technologies include absorption and membrane based processes. Absorption with amines is a selective technology especially for CO_2 separation from flue gas, CO_2 recovery rates of 98% and product purity in excess of 99% can be achieved (CCP 2008). But, it has many problems of corrosion and the cost of operation by virtue of large amounts of energy requirement in solvent regeneration (Millward and Yaghi 2005, Cavenati, Grande, and Rodrigues 2006). Gas separation through membranes is simple and environmentally benign (Basu, Cano-Odena, and Vankelecom 2011). Polymeric membranes are widely available but possess a trade-off between selectivity and throughput and high degree of separation usually cannot be achieved. Hence, multiple stages and recycle of streams is necessary, caused to increased complexity, energy consumption and costs (Li, Kuppler, and Zhou 2009, Basu, Cano-Odena, and Vankelecom 2011, Songolzadeh, Soleimani, and Takht Ravanchi 2015).

3.2. Adsorption Based Gas Separation and Purification Processes

3.2.1. Adsorption

The process where molecules from the gas phase or from the solution bind on a surface of certain porous solids is known as *adsorption*. The molecules that bind to the surface are called the *adsorbate* while the substance that holds the adsorbate on its surface is called *adsorbent*. If no structural/compositional defects are present, an ideal perfect homogenous adsorbent surface is obtained. However, such an ideal surface is very rarely encountered (Masel 1996). Real solid surfaces are made up of a combination of flat regions, corners, edges and vacancies, resulted in a heterogeneous distribution of surface active sites (Figure 3.1).

Owing to their valence unsaturation, namely as open/unsaturated metal sites, species with such defects have surface highly reactive sites capable of taking up molecules from the gas phase, providing enhanced adsorption capacities and selectivities for specific compounds (Tranchemontagne, Hunt, and Yaghi 2008, Karra and Walton 2010, Chowdhury et al. 2012, Bolis 2013, Furukawa et al. 2013).
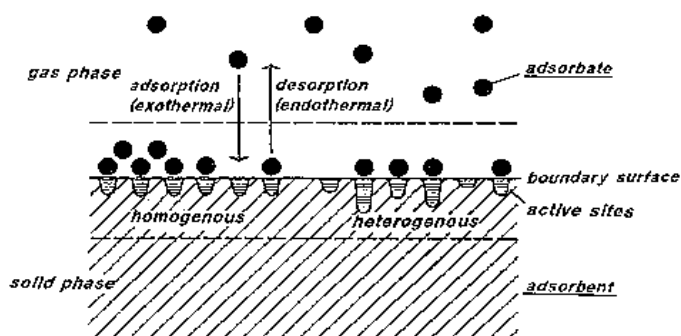
Figure 3.1. Basic concept of adsorption phenomena
(Source: adopted from Masel (1996))

Fundamentals of adsorption can be distinguished (Table 3.1) between physical adsorption, involving only relatively weak intermolecular forces, and chemisorption which related to the formation of a strong chemical bond between adsorbate and adsorbent surface. Almost all adsorptive separation processes depend on physical adsorption rather than chemisorption and directed by van der Waals forces (dispersion-repulsion) and

electrostatic interactions comprising polarization, dipole and quadrupole interactions. The van der Waals contribution is always present while the electrostatic contributions are significant only in the case of adsorbents having ionic structure (Ruthven 1984).

Table 3.1. General features which distinguish physical adsorption and chemisorption (Source: adapted from Ruthven (1984))

Physical adsorption	Chemisorption
Low heat of adsorption	High heat of adsorption
(<2 or 3 times latent heat of evaporation)	(>2 or 3 times latent heat of evaporation)
Only significant at relatively low temperatures	Possible over a wide range of temperature
Rapid, non-activated and reversible	Activated, may be slow and irreversible
No electron transfer although polarization of sorbate may occur	Electron transfer leading to bond formation between sorbate and surface
Non specific	Highly specific
Monolayer or multilayer formation	Monolayer formation only
No dissociation of adsorbed species	May involve dissociation

3.2.2. Adsorption Isotherms

In the adsorption of gases, at low pressures relatively few molecules are adsorbed, and only a fraction of the solid is covered. When all sites become occupied, the adsorbed molecules are said to form monolayer. Further increase in pressure causes multilayer adsorption. A common assumption that for adsorption on an energetically uniform surface at sufficiently low concentrations such that all molecules are isolated from their neighbors. In this low coverage regime, Henry's law is applicable (Tykodi 1958, Barrer and Rees 1961, Ruthven 1984).

Henry's law corresponds to an equation of state (Equation 3.3) with applying ideal gas law (Ruthven 1984),

$$\pi a = RT \tag{3.3}$$

Then, defining π as spreading pressure and a is the molar surface area, A is the specific surface area, n_i is the amount adsorbed based on solid mass Equation 3.4 is formed,

$$a = \frac{A}{n_i} \tag{3.4}$$

The differential form of Gibbs adsorption isotherm is stated in Equation 3.5 and the detailed derivation can be found in Ruthven (1984),

$$a \left(\frac{\partial \pi}{\partial p} \right)_T = \frac{RT}{p} \tag{3.5}$$

Combining Equation 3.4 and 3.5 results in Equation 3.6,

$$\left(\frac{\partial \pi}{\partial p} \right)_T = \frac{RT}{ap} = \frac{\pi}{p} \tag{3.6}$$

Integration of Equation 3.4 at constant temperature gives Equation 3.7 and the integration constant depends only temperature,

$$\pi = \text{constant } (T)p \tag{3.7}$$

Henry's law constant, K, is obtained in Equation 3.8, by considering Equation 3.7 and 3.3 together,

$$n_i = \frac{\pi A}{RT} = Kp \tag{3.8}$$

At low pressures (low coverage), adsorption isotherms become linearly dependent of pressure as in Equation 3.8, since in this regime gas molecules interact with the surface, interactions between adsorbed molecules are negligible. Hence, values of Henry's law constant directly indicate the average interaction energy of a single adsorbed molecule with the solid surface, consequently adsorption affinity of the adsorbate (Bottani et al. 1994, Maurer, Mersmann, and Peukert 2001, Rowsell and Yaghi 2004).

At higher concentrations the linear relationship (Equation 3.8) becomes curved and Brunauer et al. (1940) divided the isotherms for physical adsorption into five classes as shown in Figure 3.2.
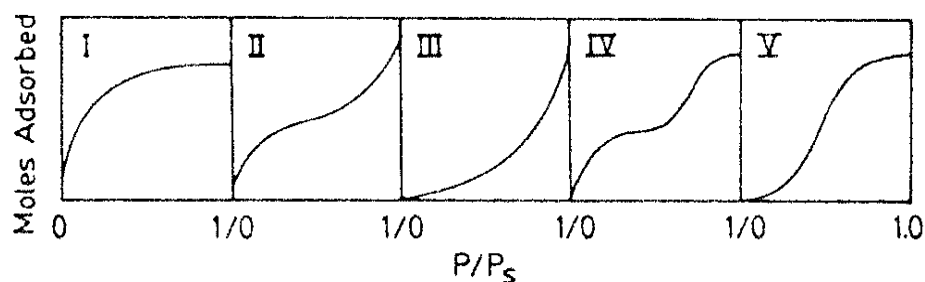
Figure 3.2. The Brunauer classification of adsorption isotherms
(Source: adopted from Ruthven (1984))

Microporous adsorbents having pore sizes not very much greater than the molecular diameter of the adsorbate molecules follow type I isotherm, because in case of such adsorbents definite saturation limit corresponding to complete filling of micropores is observed. Types I and II are the most frequently encountered in separation processes. Type II and III are observed for adsorbents with wide range of pore sizes and there is a continuous loading from monolayer to multilayer. Type III behavior is shown where the adsorbate-surface interaction is weaker than the adsorbate-adsorbate interactions. Type IV indicates the formation of two layers on a pore wall very much wider than the molecular diameter of the adsorbate. Type V is occasionally observed if intermolecular attractions are dominant (Ruthven, Farooq, and Knaebel 1994, Yang 1997).

The performance of an adsorbent can be represented by adsorption isotherm curves which are measured by a series of experiments in labs. To understand and predict the adsorption performances and to express the adsorbent capacities and, consequently to design effective design of adsorption process with minimum number of experiments as much as possible, modelling the adsorption isotherms is essential. Many models have been developed to interpret different types of isotherms, among them Langmuir and Virial isotherm models were included in this chapter, the detailed testing procedure of these models and results were given in the following chapters of this study.

The *Langmuir isotherm* is the simplest and still most useful model for monolayer adsorption for microporous adsorbents. The model is developed based on four assumptions i) molecules are adsorbed at a fixed number of well-defined localized sites, ii) each site can hold one and only one molecule, causing monolayer of finite number of adsorption sites, iii) all sites the surface are energetically uniform, iv) there is no interaction between molecules adsorbed on neighboring sites. An equation of state for the adsorbed phase at higher concentrations was proposed by Ruthven (1984) as,

$$\pi(a\text{-}\beta)=RT \tag{3.9}$$

Considering analogy of p(V-b)=NRT and Gibbs isotherm stated in Equation 3.5 give Equation 3.10 and 3.11, respectively.

$$\left(\frac{\partial \pi}{\partial a}\right)_T = \frac{RT}{\left(a\text{-}\beta^2\right)} \tag{3.10}$$

$$\frac{dp}{P} = -\frac{ada}{\left(a\text{-}\beta^2\right)} \tag{3.11}$$

Assuming $\beta \ll 2A$ for low concentrations and neglecting β^2 term stated in Equation 3.11,

$$bp = \frac{2\beta/A}{1\text{-}2\beta/A} = \frac{\theta}{1\text{-}\theta} \tag{3.12}$$

or similarly,

$$q = \frac{q_s bp}{1+bp} \tag{3.13}$$

Defining θ as the fractional coverage and taking $\theta=2\beta/A$, Equation 3.12 is obtained and it corresponds to the Langmuir isotherm model. The Langmuir model is applicable for number of practical purposes because it fits type I and initial portion of type II isotherms in (Figure 3.2) which are mostly encountered. If p is small enough, Equation 3.12 reduced to linear form θ=bP, also called Henry's law form where b acts as Henry's law constant; if p is large, θ approaches to 1.0 indicting monolayer coverage (Ruthven 1984, Yang 1997). The commonly quoted form of Langmuir model is stated in Equation 3.13, where q and q_s are the adsorbed gas amount and fixed number of surface site, respectively.

The *virial isotherm* model gives the best fit at low and medium range pressures (up to 60 bar) and small discrepancies at high pressures (Zhang, Talu, and Hayhurst 1991). From the mathematical standpoint, the virial isotherm equation has a polynomial form where the number of terms in this equation can be adjusted depending on the desired level of accuracy (Taqvi and LeVan 1997). The virial model regarded the nonideality of the system emerged as a result of adsorbate-adsorbate interactions (Haydel and Kobayashi 1967).

The adsorbed layer obeys the general EOS of virial form (Ruthven 1984) in Equation 3.14,

$$\frac{\pi a}{RT}=1+\frac{B'}{a}+\frac{C'}{a^2}+\frac{D'}{a^3}+\ldots \tag{3.14}$$

Derivation of Equation 3.14 gives Equation 3.15,

$$\left(\frac{\partial \pi}{\partial a}\right)_T=-RT\left(\frac{1}{a^2}+\frac{2B'}{a^3}+\frac{3C'}{a^4}+\frac{4D'}{a^5}+\ldots\right) \tag{3.15}$$

Considering Gibbs isotherm stated in Equation 3.5,

$$\ln p=\text{constant}(T)-\ln a+\frac{2B'}{a}+\frac{3C'}{2a^2}+\frac{4D'}{3a^3}+\ldots \tag{3.16}$$

Combining Equation 3.16 with Equation 3.4 and Equation 3.14 gives the exponential equation,

$$p=n_i \exp\left(K-\ln a+\frac{2B'}{A}n_i+\frac{3C'}{2A^2}n_i^2+\frac{4D'}{3A^3}n_i^3+\ldots\right) \tag{3.17}$$

Equation 3.17 reduces to final form of virial isotherm in Equation 3.18,

$$p=n_i \exp(K+Bn_i+Cn_i^2+Dn_i^3+\ldots) \tag{3.18}$$

K is the Henry's law constant whose value is directly related to the gas-solid interactions only, however the virial coefficients B, C and D stand for the adsorbate-adsorbate interactions.

The non-linear form of Langmuir (Equation 3.13) and virial (Equation 3.18) models were used to fit the experimental isotherm data, rather than linear forms. Because it was seen that modeling of isotherm by linear analysis might cause the inconsistency between the predictions and experimental data. In the endeavor to reliable prediction of adsorption parameters, many researchers have been advocated to investigate the applicability of linear or non-linear isotherm models in describing a number of adsorption systems, (Boulinguiez, Le Cloirec, and Wolbert 2008, Subramanyam and Das 2009, Belhachemi and Addoun 2011, Chen 2013, Subramanyam and Das 2014, Chen 2015) and it was found that the non-linear isotherm forms are more powerful and viable in modeling the adsorption isotherm data.

3.2.3. Gas Separation and Purification Processes in Adsorbent Packed Beds

Adsorption gas separation and purification processes can be distinguished from one another accordance to the purpose of the process (Ruthven 1984). For removal of low-concentration (less than 10% by weight) impurities from fluid streams, purification processes such as drying of air, natural gas, sweetening of natural gas and plant cycle gases are applicable, whereas separation processes are driven in case of major bulk mixtures separated into two or more streams such as production of O_2 and N_2 from air, separation of n-paraffins from iso-paraffins and aromatics and H_2 from industrial gases (Yang 1997).

Large scale adsorptive processes may be divided into two broad groups, i) cyclic batch system in which the adsorbent packed bed is saturated and regenerated in a cyclic manner ii) continuous flow systems, involving continuous countercurrent contact between feed an adsorbent by moving-bed adsorbers (Figure 3.3).
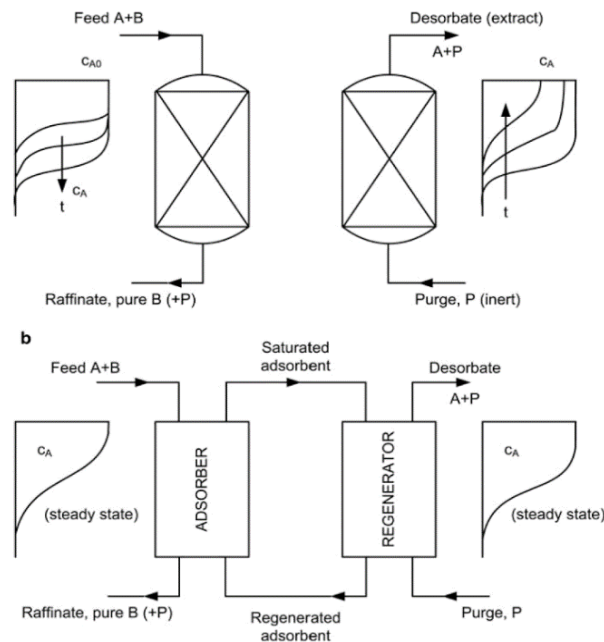
Figure 3.3. Two basic modes of operation i) fixed cyclic batch two-bed system, ii) moving continuous countercurrent system with adsorbent recirculation. Concentration profiles through the bed are indicated. A is the more strongly adsorbed species (Source: adopted from Wilcox (2012))

Although countercurrent contact maximizes the driving force for mass transfer, consequently provides more efficient usage of adsorbent, but suffer from sorbent attrition and necessity of circulation of adsorbent makes process more complex and reduces operational flexibility (Ruthven 1984, Wilcox 2012). On the other hand, fixed cyclic adsorption processes which rely upon the adsorbent packed beds offers great flexibility at both design and operational stages (Khajuria and Pistikopoulos 2013).

Fixed bed adsorption processes differ from each other based on regeneration method of the adsorbent during desorption such that purge gas stripping, thermal swing and pressure swing adsorption. The difference between the modes of adsorption operations is stated in Figure 3.4. In purge gas stripping the packed bed is regenerated at constant pressure and temperature by purging with a nonadsorbing inert gas. In thermal swing adsorption (TSA), the adsorbent is regenerated by heating the bed at elevated temperature, while during pressure swing adsorption (PSA) the bed is purged at low pressure and constant pressure (Ramaswamy, Huang, and Ramarao 2013). The comparison between purge gas stripping, TSA and PSA operation is tabulated in Table 3.2.
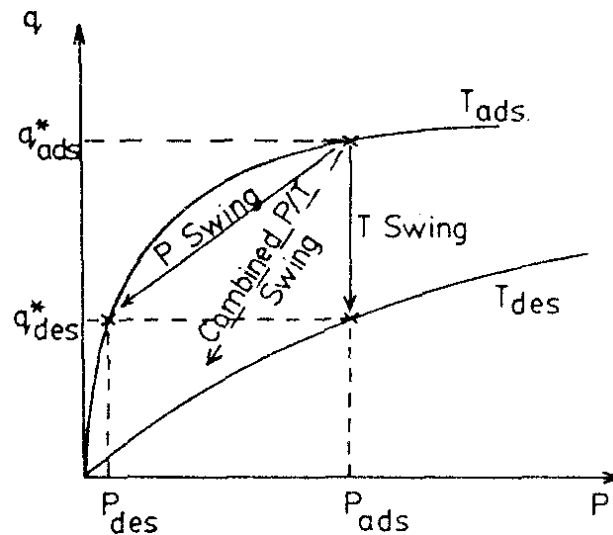
Figure 3.4. Schematic isotherms showing pressure swing, thermal swing and combined pressure-temperature swing operation for an adsorption process
(Source: adopted from Ruthven (1984))

Table 3.2. Summary of factors governing choice of regeneration method for packed bed adsorption (Source: adopted from Ruthven (1984) and Thomas and Crittenden (1998))

Method	Advantages	Disadvantages	Applications
Purge gas stripping	Essentially at constant T and P	Only for weakly adsorbed species. Purge flow is high	Used in a combination with TSA and/or PSA
Temperature swing adsorption (TSA)	Good for strongly adsorbed species. Desorbate recovered at high concentrations	Thermal ageing of sorbent. Heat loss leads to thermal inefficiency	Drying of gases. Drying of solvents
Pressure swing adsorption (PSA)	Good for relatively weak adsorbed species required in high purity	Very low P may be required	Hydrogen recovery. Air separation

3.2.4. Dynamic Behavior of Adsorbent Packed Beds

An understanding of the dynamic behavior of adsorption processes is crucial for rational process design and optimization (Do 1998). To analyze packed bed dynamics, it is convenient to classify adsorption equilibria as favorable, linear or unfavorable depending on the shape of dimensionless diagram (Figure 3.5) where $q_{0-}q_0'$ and $c_{0-}c_0'$ stand for changes in adsorbed and fluid phase, respectively. The direction of mass transfer direction is from fluid to adsorbed phase, the adsorbed phase concentration is always greater than the fluid phase concentration in the favorable case (Ruthven, Farooq, and Knaebel 1994).
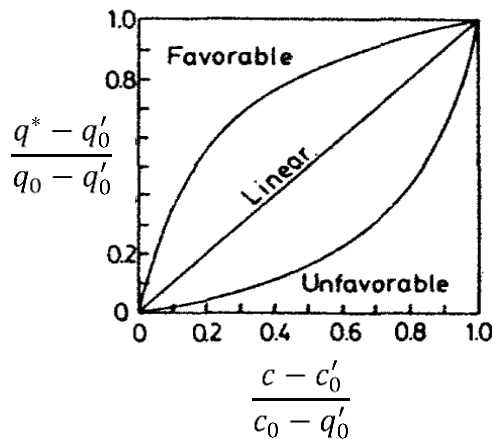
Figure 3.5. Equilibrium diagram showing the favorable, unfavorable and linear systems (q^*: equilibrium adsorbed amount) (Source: adopted from Ruthven (1984))

Considering Figure 3.2, the Brunauer classification of adsorption isotherms types I, II and IV describe favorable equilibrium (Figure 3.5) whereas type III and V represent unfavorable ones. Among these, adsorbents that exhibit type I behavior are preferred for adsorption based gas separation processes carried out in a packed bed (Ramaswamy, Huang, and Ramarao 2013).

In fixed bed adsorbers, the adsorption process is represented by breakthrough curves. A gas feed is passed through an adsorbent packed bed where its composition is changed with time depend on the properties of the adsorbent, the composition of the feed, and the operating conditions (feed flow rate, bed pressure etc.). Plot of change in the ratio C/C_0 (outlet adsorbate concentration/ adsorbate feed concentration) with time is denominated as breakthrough curve (Figure 3.6).

Most of the mass transfer takes place near the inlet of the bed, where the gas feed first contacts the adsorbent. If the solid contains no adsorbate at first, the gas phase concentration drops exponentially to zero before the end of the bed is reached. With time, the adsorbent near the inlet is nearly saturated, and most of the mass transfer shifts further from the bed inlet. In case of the real dynamic behavior of packed bed, the concentration gradient is S shaped and the region where most of the change in concentration occurs is called the mass transfer zone (MTZ). In ideal case, the axial or radial mass transfer resistances are neglected and mass transfer resistances can be minimized. Then, MTZ moves downwards through the bed until the breakthrough occurs. When this zone reaches the bottom of the bed, the adsorbate cannot be adsorbed any longer and this moment is called as breakpoint (t_b, C_b). When the MTZ leaves the bed, the bed is completely saturated at t_s (time required to saturation of the adsorbent) and the effluent leaves the bed at same concentration as feed ($C/C_0 = 1.0$). Finally, the adsorptive gas flow is stopped and the adsorbent is regenerated by flowing an inert gas through the bed (M. A. S. D. Barros 2013).
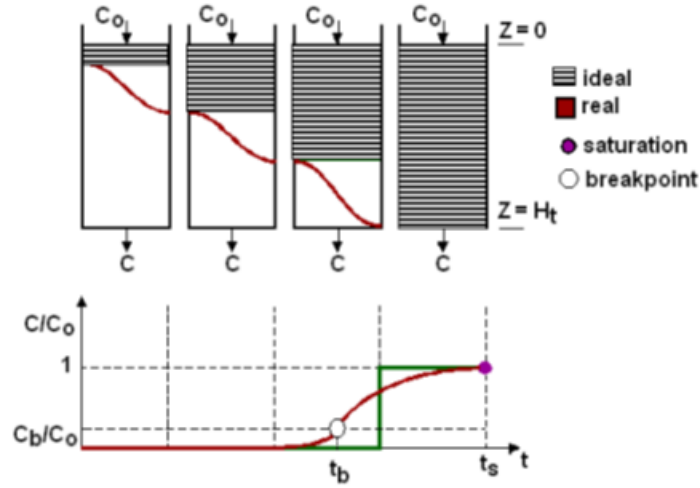
Figure 3.6. Breakthrough curve in fixed beds C_o is the concentration of the inlet solution, C_b is the concentration of the breakthrough, t_b is the breakpoint time and t_s is the saturation time (Source: adopted from M. A. S. D. Barros (2013))

M. A. S. D. Barros (2013) highlighted that operating the fixed bed with minimum mass transfer resistances is quite advantageous, it maximizes the adsorption process as more adsorption sites are available to the dynamic process. In this respect, several operational parameters such as the length of unused bed, operational ratio, in the breakthrough should be checked for describing the dynamic behavior of adsorbent packed column, efficiently.

The time equivalent to usable capacity of the bed (t_u) and the time equivalent to total stoichiometric capacity of the packed-bed (t_t) if the entire bed reaches equilibrium are obtained by a mass balance around the bed (Geankoplis 1993) and they are calculated by Equation 3.19 and 3.20, respectively.

$$t_u = \int_0^{t_b} \left(1 - \frac{C}{C_0}\right) \tag{3.19}$$

$$t_t = \int_0^{t_s} \left(1 - \frac{C}{C_0}\right) \tag{3.20}$$

If time t is assumed to be the time equivalent to the usable capacity of the bed (t_u) up to t_b, the ratio of t_u/t_t gives the fraction of total bed capacity of length utilized up to breakpoint.(Geankoplis 1993). Hence, the length of unused bed (H_{UNB}) is the unused fraction times the total length (H_t) Equation 3.21 is obtained,

$$H_{UNB} = \left(1 - \frac{t_u}{t_t}\right) H_t \tag{3.21}$$

H_{UNB} is the key design parameter when scaling up adsorbers. The total length is split into the required length of an ideal bed process and a segment of unused bed that is the length leftover at breakthrough. Also, as regards to scaling-up processes it is frequently assumed to be constant (McCabe, Smith, and Harriott 1985). A constant H_{UNB} can be obtained as a consequence of constant mass transfer zone for ideal adsorption systems (M. A. S. D. Barros 2013).

One of the most important factor for investigating the cyclic adsorption processes is the cycle time associated with the concept of the packed bed dynamics. In the scope of packed bed dynamics not only the aforementioned parameters such as breakthrough time, saturation time and length of unused bed, but also time required to pressurize the bed at a desired value is a critical operation parameter for cyclic processes, especially for PSA (Cen and Yang 1986, Lopes, Grande, and Rodrigues 2011, Ahn et al. 2012, Kim, Nam, and Kang 2015, Khunpolgrang et al. 2015). The cycle time is the combination of the time allotted for the pressurization of packed bed, time to breakpoint and the time for desorption/depressurization (Silva, Da Silva, and Rodrigues 2000, Arvind, Farooq, and Ruthven 2002, Dantas et al. 2011, Ferreira et al. 2015)(Silva 2000, Arvind 2002, Dantas 2011, You 2012, Ferreira 2015). Reducing the cycle time is the primary means of achieving more production form a given quantity of material as reducing adsorbent inventory and cost, since shorter cycles result in small beds, hence decrease in the process plant size as the cycling becomes more rapid (Todd and Webley 2006, Chai, Kothare, and Sircar 2011). However, working capacity of the adsorbent and the product recovery often decreases as the cycle time is decreased (Yang et al. 1997, Grande and Rodrigues 2005, Rezaei and Webley 2009, Rezaei and Webley 2010, Mohammadi et al. 2016).

3.3. Adsorbents

The search for a suitable adsorbent is the first step in the development of an adsorption separation process. The recognition of the ability of porous solids to reversibly adsorb large volumes dates back to eighteenth century however, large scale application of adsorption as a means of separating mixtures into two or more streams by an adsorbent packed bed column is relatively recent.

3.3.1. Traditional Adsorbents

Traditional adsorbents such as silica gel, activated alumina and activated carbons, the broad distribution of micropore size is present depending on the synthesis. Particularly for activated carbons, variations in the pore size distribution, pore structure and active surface area differ depending on wide variety of resources (e.g., bituminous coal, lignite, petroleum, coke pitch) (Davini 2002). These classical adsorbents possess high open porosity and high specific surface area with an advantage of the low cost, but they have disordered structure. Besides, the broad pore size distribution makes many channels or cavities are often unnecessary, leading to poor storage and separation capacity for a specific guest (Kitagawa, Kitaura, and Noro 2004, Choi, Drese, and Jones 2009).

By contrast, zeolite framework consists of an assemblage of SiO_4 and AlO_4 tetrahedra joined together in regular crystalline arrangements. The feature distinguishes the zeolites from the traditional adsorbents is that the micropore structure and size are controlled by crystal nature without any virtual distribution of pore size (Ruthven 1984). Zeolites offer high crystallinity with regular channels or cavities but a low porosity with moderately high surface areas.

On the other hand, as mentioned in previous chapter, MOFs which recently emerged as a new class of porous hybrid materials constructed from inorganic and organic building blocks, and are preferred over traditional adsorbents such as activated carbon and zeolites due to their unique characteristics. Table 3.3 compares characteristics of zeolites, MOFs and activated carbons.

Table 3.3. Comparison between the structural, physical, and chemical properties of zeolites, mesoporous silica and alumina, and MOFs (Source: adapted from Ranocchiari and Bokhoven (2011))

	Zeolites	MOFs	Activated carbon
Nature	Crystalline	Crystalline	Amorphous
Homogenous active sites	✓	✓	✗
Pore sizes	Very discrete	Adjustable	Varied
Surface area	$< 600 \ m^2g^{-1}$	Up to $10\ 400 \ m^2g^{-1}$	$400\text{-}1200 \ m^2g^{-1}$
Diffusivity	Low	Low to high	High
Thermal stability	High	Low to medium	Medium
Chemical versatility	Low	High	Medium-low

3.3.2. Metal Organic Frameworks in Adsorption Based Gas Separation and Purification Processes

To date, many researches on the application of metal organic frameworks in regard to adsorption based separation/purification have been published. The adsorptive gas separation/purification studies on metal terephthalates; copper, aluminum, titanium and zinc terephthalates were demonstrated in Table 3.4, 3.5, 3.6 and 3.7, respectively.

Copper based frameworks (CuMOFs) can be synthesized by various organic ligands resulted in different structural and textural characteristics that enable the application of CuMOFs in CH_4, natural gas and H_2 storage, separation of binary mixtures and sensing as in Table 3.4. Copper terephthalate (MIL-53(Cu), CuTPA) synthesized with metal source of $Cu(NO_3)_2 \cdot 3H_2O$ and BDC ligand used for the first time as an adsorbent for methane gas adsorption by (Anbia and Sheykhi 2012) with 8.52 mmolg^{-1} of CH_4 uptake capacity at 298 K and 35 bar. Incorporating MIL-53(Cu) to multi-walled carbon nanotubes (MWCNTs) resulted in MWCNT@MIL-53-Cu structure with enhance CH_4 adsorption capacity to 13.72 mmolg^{-1} (Anbia and Sheykhi 2013). Also, for the first time MIL-53(Cu) were investigated for natural gas storage purposes by Anbia et al. (2014), the adsorbed amounts were found in the order of $CH_4 \gg CO_2 > H_2$ at whole pressure range up to 30 bar at 298 K with high selectivity of CH_4 over CO_2 (11.5).

Moreover, H_2 storage studies on copper based MOFs CuTATB, NOTT-112 and HKUST-1 showed that gravimetric H_2 uptake was directly related to the aromatic rings on the organic linkers and pore sizes of the adsorbents, as smaller pore size increases the hydrogen binding, allowing a single H_2 molecule to interact with multiple aromatic rings. At 77 K and elevated pressures, the H_2 storage performance of copper MOFs was found promising; the H_2 uptakes of CuTATB, NOTT-112 and HKUST-1 were calculated as 1.9 wt%, 2.3 wt% and 1.95 wt%, respectively (Sun et al. 2006, Yan et al. 2009, Lin et al. 2012).

The separation of small gas molecules, especially achieving high-purity acetylene from C_2H_2/CH_4 and C_2H_2/CO_2 mixtures possesses great importance for petrochemical industry. In that content, UTSA-15 and ZJU-26, as the members of CuMOF family, consisted of different metal sources and organic linkers, were used as adsorbents in the separation acetylene from binary mixtures. High selectivity of acetylene over methane (55.6) was accomplished by UTSA-15 at 296 K and 1 bar, while ZJU-26 offered only 1.72 acetylene selectivity to CO_2 (Chen et al. 2011, Duan et al. 2013).

Great deal of efforts have been directed towards the application of MOFs in CO_2 capture due to the concerns on global warming. In this point of view, adsorption of CO_2, CH_4, N_2 single components (Karra et al. 2013, Yang et al. 2012) and their binary mixtures CO_2/CH_4, CO_2/N_2 and CH_4/N_2 (Wu et al. 2014, Yang, Sitprasert, et al. 2015, Li et al. 2014) on various copper organic frameworks were investigated in detail. Cu based organic framework HKUST-1 showed better performance than zinc based MOF-5 as a result of unsaturated Cu metal sites found in HKUST-1 porous structure. Karra et al. (2013) reported the H_2O adsorption and the impact of exposure on the structural degradation of MOF-14, it was shown that water exposure on MOF-14 caused 54% loss in the surface area.

Even though, the general trend in application areas of copper based organic frameworks has been towards to gas separation and purification processes, the binding ability of functional groups make copper based MOFs convenient to use in sensoring areas. Sahiner et al. (2014) synthesized MOFs based on TMA (TMA: trimesic acid) with Cu(II) from different salts to investigate their conductivity performances.

Table 3.4. Adsorption based gas separation/purification studies on copper based and related metal organic frameworks in literature

Materials	Metal Source	Ligand*	S_{BET} (m^2g^{-1})	V_{pore} (cm^3g^{-1})	Applications	Ref.
MIL-53(Cu)	$Cu(NO_3)_2 \cdot 3H_2O$	BDC	1150	0.65	CH$_4$ storage	Anbia and Sheykhi (2012)
MIL-53(Cu)	$Cu(NO_3)_2 \cdot 3H_2O$	BDC	1283	0.48		Anbia and Sheykhi (2013)
MWCNT@MIL-53-Cu	$Cu(NO_3)_2 \cdot 3H_2O$	BDC	1123	0.39		
MIL-53(Cu)	$Cu(NO_3)_2 \cdot 3H_2O$	BDC	1283	0.48	Natural gas storage	Anbia and Sheykhi (2014)
CuTATB	$Cu(NO_3)_2 \cdot 2.5H_2O$	TATB	3800	-	H$_2$ storage	Sun et al. (2006)
NOTT-112	$Cu(NO_3)_2 \cdot 3H_2O$	H$_6$L	3800	1.62		Yan et al. (2009)
HKUST-1	$Cu(NO_3)_2 \cdot 2.5H_2O$	BTC	1009	0.06		Lin et al. (2012)
UTSA-15	$Cu(OAc)_2 \cdot 3H_2O$	BDC-OH/ 4,4'-bpy	553	-	Purification of acetylene	Chen et al. (2011)
ZJU-26	$Cu(NO_3)_2 \cdot 2.5H_2O$	H$_4$ADDI	989	0.57	Purification of acetylene	Duan et al. (2013)
Cu(hfipbb)	$Cu(NO_3)_2 \cdot 3H_20$	H$_2$hfipbb	105	0.04	CO$_2$ capture	Wu et al. (2014)
HKUST-1	$Cu(NO_3)_2 \cdot 3H_2O$	BTC	1978	0.81		Yang et al. (2015)
HKUST-1	$Cu(NO_3)_2 \cdot 3H_2O$	BTC	452	0.28		Li et al. (2014)
MOF-5	$Zn(NO_3)_2 \cdot 6H_2O$	BDC	621	0.30		
MOF-14	$Cu(NO_3)_2 \cdot 3H_2O$	BTB	1398	0.57		Karra et al. (2013)
Cu(dhbc)$_2$(bpy)	$Cu(NO_3)_2 \cdot 3H_2O$	DHBC/BPY	364	-		Yang et al. (2012)
Cu(BF$_4$)$_2$(bpy)$_2$	$Cu(BF_4)_2 \cdot 6H_2O$	BPY	622	-		
HKUST-1	$Cu(NO_3)_2 \cdot 2.5H_2O$	BTC	1571	0.79		Liang et al. (2009)
Zeolite 13X	-	-	616	0.34		
CuTMA	$CuSO_4 \cdot 5H_2O$	TMA	5.58	0.02	Sensoring	Sahiner et al. (2014)
CuTMA	$Cu(CH_3CO_2)_2 \cdot H_2O$		107	0.23		
CuTMA	$Cu(NO_3)_2 \cdot 3H_2O$		850	0.039		

*BDC, TPA: 1,4-benzenedicarboxylic acid; TATB: 4,4',4''-s-triazine-2,4,6-triyltribenzoate; H$_6$L: 1,3,5 tris(3',5''-dicarboxy[1,1'-biphenyl]-4-yl)benzene; BTC: 1,3,5-benzenetricarboxylic acid; BDC-OH: 2-hydroxyterephthalic acid; 4,4'-bpy: 4,4'-bipyridine; H$_4$ADDI = 5,5'-(anthracene-2,6-diyl) diisophthalic acid; H$_2$hfipbb = 4,4'-(hexafluoro-isopropylidene) bisbenzoic acid; BTB: 4,4',4''-benzene-1,3,5-triyl-tribenzoic acid; DHBC = 2,5-dihydroxybenzoic acid; BPY = 4,4'-bipyridine; TMA: trimesic acid.

Aluminum based organic frameworks (AlMOFs) synthesized by different metal sources and organic linkers were stated in Table 3.5. The most common AlMOF is aluminum terephthalate (MIL-53(Al), AlTPA), commercially named as BASF Basolite A100, synthesized with BDC organic linker and aqueous form of aluminum nitrate. It can be found in different forms; tablet, powder, pellet and utilized for adsorption based CH$_4$

purification and separation of acidic gas mixtures. Tablet form Basolite A100 is known by its water stability and provided moderately high selectivity between CH_4 and CO_2 about 4 and high purity methane at 99% and CO_2 at 95% achieved at 303 K and 4 bar (Ferreira et al. 2015). Although, Basolite A100 pellets showed lower adsorption capacities compared to powder form, pellet form was found better candidate for selective CH_4 separation of CH_4 from acidic gas mixtures of CH_4/CO_2 and CH_4/H_2S (Heymans, Vaesen, and De Weireld 2012).

Also, by using BDC-NH_2 ligand, amino functionalized aluminum terephthalates (amino- MIL-53(Al)) were synthesized and studied for upgrading of biogas and CO_2 capture. In comparison with zeolite 13 X, amino- MIL-53(Al) had lower CO_2 adsorption capacity but it provided 20 time higher selectivity for CO_2 over CH_4 at 1 bar and 303 K (Peter et al. 2013). For CO_2 capture, in order to improve CO_2 uptake and selectivity of aluminum based MOFs, different organic linkers (BDC, BTC and BDC/PVA) in different forms (powders and pellets) were tested. Abid et al. (2016) found that although MIL-96(Al) has lower BET surface area than MIL-53(Al), the CO_2 uptake capacity of MIL-96(Al) was much higher as a result of three bridging hydroxyl group in BTC linker which enables the strong interactions with CO_2. Besides, combining PVA binder to aluminum terephthalate pellets (MIL-53(Al)/PVA) resulted in a great loss in overall CO_2 uptake capacity, but enhanced the CO_2 selectivity over CH_4 up to 7 at 1 bar and 303 K (Finsy et al. 2009) compared to MIL-53(Al) synthesized by Rallapalli et al. (2011) which exhibited selectivity for CO_2 as 3.8 at the same conditions.

For separation of linear n-alkanes and H_2 storage aluminum and chromium based terephthalates that compose of BDC ligand in common were frequently examined. It was reported that depending on the nature of metal (Al, Cr) the adsorption isotherms greatly differs due to energetic considerations related to the interaction that occurs between the n-alkane species and MOFs (Trung et al. 2008). Moreover, the MIL-53(Al) which had comparable surface area to MIL-53(Cr) showed higher H_2 uptake capacity at 77 K and 16 bar (Ferey et al. 2003).

Table 3.5. Adsorption based gas separation/purification studies on aluminum based and related metal organic frameworks in literature

Materials	Metal Source	Ligand*	S_{BET} (m^2g^{-1})	V_{pore} (cm^3g^{-1})	Applications	Ref.
BASF Basolite A100 tablet	$Al(NO_3)_3 \cdot 9H_2O$	BDC	560	-	CH_4 purification	Ferreira et al. (2015)
BASF Basolite A100 powder	$Al(NO_3)_3 \cdot 9H_2O$	BDC	830	0.55	Acidic gas separation	Heymans et al. (2012)
BASF Basolite A100 pellet	$Al(NO_3)_3 \cdot 9H_2O$		601	0.40		
amino- MIL-53(Al)	$Al(NO_3)_3 \cdot 9H_2O$	$BDC-NH_2$	-	-	Upgrading of biogas	Peter et al. (2013)
Zeolite 13X	Si/Al = 1.23	-	-	-		
amino- MIL-53(Al)	$Al(NO_3)_3 \cdot 9H_2O$	$BDC-NH_2$	262	1.31	CO_2 capture	Abid et al. (2016)
MIL-53(Al)	$Al(NO_3)_3 \cdot 9H_2O$	BDC	1519	0.78		
MIL-96(Al)	$Al(NO_3)_3 \cdot 9H_2O$	BTC	687	0.34		
MIL-53(Al)/ PVA pellet	$Al(NO_3)_3 \cdot 9H_2O$	BDC/PVA	-	-		Finsy et al. (2009)
MIL-53(Al)	$Al(NO_3)_3 \cdot 9H_2O$	BDC	1235	-	CO_2 capture	Rallapalli et al. (2011)
MIL-53(Al)	$Al(NO_3)_3 \cdot 9H_2O$	BDC	-	-	Separation of linear n-alkanes	Trung et al. (2008)
MIL-53(Cr)						
MIL-53(Al)	$Al(NO_3)_3 \cdot 9H_2O$	BDC	1020	-	H_2 storage	Férey et al. (2003)
MIL-53(Cr)	$Cr(NO_3)_3 \cdot 9H_2O$		1026	-		

*BDC, TPA: 1,4-benzenedicarboxylic acid; $BDC-NH_2$=2-amino-1,4-benzenedicarboxylic acid; PVA: polyvinyl alcohol; BTC: 1,3,5-benzenetricarboxylic acid.

Titanium based organic frameworks (TiMOFs) are generally synthesized using titanium isopropoxide ($Ti(OiPr)_4$) as metal cluster and various organic ligands (Table 3.6). Titanium terephthalates (MIL-53(Ti), TiTPA) were studied for natural gas, syngas and fuel purification, acidic gas separation and CO_2 capture and they were functionalized with amino (amino-MIL-125(Ti)) and methyl (m-MIL-125(Ti)) groups to enhance their adsorptive performances. Wiersum et al. (2013) examined the adsorbent performance indicator (API) of three porous materials; titanium (MIL-125(Ti)), chromium (MIL-101(Cr)) and copper (HKUST-1) based MOFs and it was stated that these MOFs could be effectively used for the separation of CO_2/CH_4 mixtures with high CO_2 selectivities to CH_4 as 3.8, 23.6 and 7.1 for MIL-125(Ti), MIL-101(Cr) and HKUST-1, respectively. In case of syngas purification, it was seen that CO_2/H_2 separation achieved with 100% hydrogen purity by using amino functionalized titanium terephthalate (amino-MIL-125(Ti)) granules as adsorbent (Regufe et al. 2015).

Furthermore, for the separation of alkane mixtures especially for n-hexane/2-methypentane mixture, MIL-125(Ti) offered 6.8 selectivity towards to n-hexane, while HKUST-1 gave only 0.79. This n-hexane selectivity difference between MIL-125(Ti) and HKUST-1 was clarified by Ramsahye et al. (2014) as the effect of MOF pore shape on adsorption mechanisms. The acid gas stability of MIL-125(Ti) and cerium based framework (CeBTC) was investigated by Mounfield Iii et al. (2016) and provided visual insight into the degradation mechanisms after acid gas (CO_2/SO_2) exposure. After 15 min of CO_2 and SO_2 exposure the stability of MIL-125(Ti) was found better than CeBTC. Titanium terephthalates and their functionalized forms were frequently studied for CO_2 capture and it was shown that addition of amino group increases the surface area as well as the CO_2 and CH_4 uptake capacities in CO_2/CH_4 separation and improve the selectivity towards CO_2 (Rada et al. 2015). On the other hand, Im et al. (2014) illustrated the CO_2 uptake capacities of MIL-125(Ti) and methyl functionalized m-MIL-125(Ti) before and after 2 h of water exposure. Without water exposure the CO_2 uptake capacities of MIL-125(Ti) and m-MIL-125(Ti) were similar, but after 2 h of water exposure MIL-125(Ti) experienced great loss in BET surface area, consequently sharp decrease in CO_2 uptake capacity, whereas the stability of m-MIL-125(Ti) was almost maintained.

Table 3.6. Adsorption based gas separation/purification studies on titanium based and related metal organic frameworks in literature

Materials	Metal Source	Ligand*	S_{BET} (m^2g^{-1})	V_{pore} (cm^3g^{-1})	Applications	Ref.
MIL-125(Ti)	Ti(OiPr)$_4$	BDC	1820	0.67	Natural gas purification	Wiersum et al. (2013)
MIL-101(Cr)	Cr(NO$_2$)$_3$•9H$_2$O		3870	1.57		
HKUST-1	Cu(NO$_3$)$_2$•3H$_2$O	BTC	1850	0.67		
amino-MIL-125(Ti) granules	Ti$_8$O$_8$(OH)$_4$	BDC-NH$_2$	-	-	Syngas purification	Regufe et al. (2015)
MIL-125(Ti)	Ti(OiPr)$_4$	BDC	1550	0.65	Fuel purification	Ramsahye et al. (2014)
HKUST-1	Cu(NO$_3$)$_2$•3H$_2$O	BTC	692	0.33		
MIL-125(Ti)	Ti(OiPr)$_4$	BDC	1392	-	Acidic gas separation	Mounfield III et al. (2016)
CeBTC	Ce(NO$_3$)$_3$•6H$_2$O	BTC	752	-		
MIL-125(Ti)	Ti(OiPr)$_4$	BDC	714	-	CO$_2$ capture	Rada et al. (2015)
amino-MIL-125(Ti)	Ti(OiPr)$_4$	BDC-NH$_2$	1660	-		
MIL-125(Ti)	Ti(OiPr)$_4$	BDC	1550	0.74		Im et al. (2014)
MIL-125(Ti)-2h	Ti(OiPr)$_4$		280	0.37		
m- MIL-125(Ti)	Ti(OiPr)$_4$	BDC-Me$_4$	830	0.40		
m- MIL-125(Ti)-2h	Ti(OiPr)$_4$		550	0.41		

*BDC: 1,4-benzenedicarboxylic acid; BTC: 1,3,5-benzenetricarboxylic acid; BDC-NH$_2$=2-amino-1,4-benzenedicarboxylic acid; BDC-Me$_4$: tetramethyl benzene-1,4-dicarboxylic acid.

Zinc based organic frameworks (ZnMOFs), especially MOF-5 synthesized by zinc nitrate hexahydrate ($Zn(NO_3)_2 \cdot 6H_2O$) and BDC organic linker, have drawn great attention as an adsorbent used in hydrogen storage (Table 3.7). Tetrahedral $[Zn_4O]^{6+}$ units linked via rigid arylcarboxylate ligands were found to adsorb large amount of H_2 at low temperatures (77K) and high pressures. Eddaoudi, Li, and Yaghi (2000) reported the porous and thermally stable MOF-5 framework and its H_2 uptake capacity was 4.5 wt% at 77 K and 0.8 bar and 1 wt% at room temperature and 20 bar. Later, Rowsell and Yaghi (2004) found the maximum H_2 uptake of MOF-5 as 1.32 wt% at 1 bar and 77 K. The effect of air exposure on the structural properties of MOF-5 was studied by Panella and Hirscher (2005) and it was observed that exposing the sample in air for six weeks collapsed the whole structure. Also, 1.6 wt% of H_2 adsorption capacity of MOF-5 at 77 K and 10 bar decreased to less than 0.2 wt % at room temperature and 67 bar, highlighting the critical importance of extremely low temperature as requirement for H_2 storage. Moreover, Panella et al. (2006) showed that the hydrogen physically adsorbed in MOFs and the saturation value of MOF-5 as 5.1 wt% at 77 K over 80 bar. Later on, Lee et al. (2007) studied the mixed ligand ZnMOF (Zn(BDC)(TED)$_{0.5}$, (TED: triethylenediamine) with the highest H_2 sorption capacity (2.1 wt%) at 77 K and 1 bar to date. Moreover, Kaye et al. (2007), Li, Kuppler, and Zhou (2009), Saha, Wei, and Deng (2009) and Segakweng et al. (2016) were synthesized ZnMOFs and conducted H_2 adsorption measurements, however they came up with different H_2 uptake capacities as a result of variations in synthesis procedure, presence of solvent molecules and other impurities in MOF structures.

Moreover, Zn$_2$DHTP (DHTP: 2,5 dihydroxyterephthalic acid) was tested for CH_4 storage, as it offers large densities of open metal sites that make possible to adsorb one CH_4 molecule per open metal, resulted in very large CH_4 storage capacities as 160-174 $cm^3(STP)/cm^3$ at 298 K up to 35 bar (Wu, Zhou, and Yildirim 2009). Ling et al. (2011) examined the selective adsorption of Zn(BDC)(hmtrz)$_2$ (hmtrz: 3,5-dimethyl-1H,1,2,4-triazole) for linear and monobranced hexane isomers over a dibranched one and suggested MOF-5 as a potential adsorbent to separate hexane isomers to boost RON of gasoline. Also, Mishra et al. (2012), Zhang et al. (2010) and Karra and Walton (2010) were investigated CO_2 capture performance of ZnMOFs synthesized from different routes using various organic linkers and results implied that incorporating functional groups into the structure enhance the selectivity towards CO_2.

Table 3.7. Adsorption based gas separation/purification studies on zinc based and related metal organic frameworks in literature

Materials	Metal Source	Ligand*	S_{BET} (m^2g^{-1})	V_{pore} (cm^3g^{-1})	Applications	Ref.
MOF-5	$Zn(NO_3)_2•6H_2O$	BDC	2900	1.04	H$_2$ storage	Eddaoudi et al. (2000)
MOF-5	$Zn(NO_3)_2•6H_2O$	BDC	3362	1.02		Rowsell et al. (2004)
MOF-5	$Zn(NO_3)_2•6H_2O$	BDC	572	-		Panella and Hirscher (2005)
MOF-5	$Zn(NO_3)_2•6H_2O$	BDC	2296	-	H$_2$ storage	Panella et al. (2006)
MOF-5	$Zn(NO_3)_2•6H_2O$	BDC	3100	-		Kaye et al. (2007)
MOF-5	$Zn(NO_3)_2•6H_2O$	BDC	840	0.34		Li et al. (2009)
MOF-5	$Zn(NO_3)_2•6H_2O$	BDC	2449	1.39		Saha et al. (2009)
MOF-5	$Zn(NO_3)_2•6H_2O$	BDC	835	0.38		Segakw. et al. (2016)
Zn(BDC)ted	$Zn(NO_3)_2•6H_2O$	BDC/ted	1794	0.65		Lee et al. (2007)
Zn$_2$DHTP	$Zn(NO_3)_2•6H_2O$	DHTP	885	0.41	CH$_4$ storage	Wu et al. (2009)
Zn(BDC)hmtrz	$Zn(OAc)_2•2H_2O$	BDC/hmtrz	552	-	Separation of RON** alkanes	Ling et al. (2011)
ZnDABCO	$Zn(NO_3)_2•6H_2O$	BDC/dabco	1863	0.67	CO$_2$ capture	Mishra et al. (2012)
Zn$_5$BTAtda	$Zn(NO_3)_2•6H_2O$	BTA/tda	414	0.24		Zhang et al. (2010)
Zn$_2$BDCdabco	$Zn(NO_3)_2•6H_2O$	BDC/dabco	1685	-		Karra and Walton (2010)

*BDC, TPA: 1,4-benzenedicarboxylic acid; TED: triethylenediamine; DHTP: 2,5 dihydroxyterephthalic acid; hmtrz: 3,5-dimethyl-1H, 1, 2, 4-triazole; DABCO: 1,4-diazabicyclo (2, 2,2) octane, BTA:2,3-benzenetriazole; TDA: thiophene-2,5-dicarboxylic acid; BTC: 1,3,5-benzenetricarboxylic acid, **RON: Low research-octane number

CHAPTER 4

EXPERIMENTAL STUDIES

4.1. Materials

All materials used in the synthesis of four different MOFs; copper terephthalate (CuTPA), aluminum terephthalate (AlTPA), titanium terephthalate (TiTPA) and zinc terephthalate (ZnTPA) were listed in Table 4.1. No further purification was applied.

Table 4.1. Materials used in the MOF synthesis and their properties

Material	Chemical Formula	%Purity	Vendor
Copper (II) nitrate trihydrate	$Cu(NO_3)_2 \cdot 3H_2O$	≥ 99.5	Merck
Aluminum nitrate nonahydrate	$Al(NO_3)_3 \cdot 9H_2O$	≥ 99.5	Sigma Aldrich
Titanium (IV) isopropoxide (TTIP)	$Ti[OCH(CH_3)2]_4$	≥ 98	Merck
Zinc acetate dihydrate (ZnAc)	$Zn(CH_3COOH)_2 \cdot 2H_2O$	≥ 99.5	Merck
Benzene-1,4-dicarboxylic acid (Terephthalic acid, TPA or BDC)	C_6H_4-1,4-$(COOH)_2$	≥ 99.6	Petkim
N, N- dimethylformamide (DMF)	$HCON(CH_3)_2$	≥ 99.8	Merck
Methanol	CH_3OH	≥ 99.9	Merck

4.2. Synthesis of Copper, Aluminum, Titanium and Zinc Terephthalates

The solvothermal synthesis route for CuTPA, AlTPA, TiTPA and ZnTPA comprises three main steps which are crystallization, purification and activation, respectively. The synthesis studies of CuTPA and AlTPA were conducted in IYTE, while the syntheses of TiTPA and ZnTPA were carried out in Ege University.

4.2.1. Synthesis of Copper Terephthalate (CuTPA)

The synthesis studies of CuTPA were conducted in IYTE (Çiçek 2014). The CuTPA was synthesized in accordance with a previously published solvothermal procedures by Carson et. al. (2009) and Carson et. al. (2014) with several adjustments.

The synthesis of CuTPA sample which was packed into fixed bed for further adsorption studies started with the dissolution of copper nitrate trihydrate ($Cu(NO_3)_2 \cdot 3H_2O$)) (2.42 g, 10 mmol) and benzene-1,4-dicarboxylic acid (TPA) (1.66 g, 10 mmol) in equimolar quantities (Cu/TPA molar ratio:1.0) in N, N- dimethylformamide (DMF) under stirring at room temperature for 1 hour at 330 rpm. The solution was taken into sealed heat-resistant glass flask (500 ml), placed in oven (Binder ED 53 and Memmert 100-800) at a crystallization temperature of 110 °C for 24 h. Then, solution was cooled down for 3.5 h while small blue particles specific to copper based MOFs became clearly visible inside the flask. The solution was centrifuged (Hettich Rotofix 32) at 3000 rpm for 25 min, the resulted blue precipitate was dried in vacuum oven (P-Selecta Vaciotem-T) overnight. To remove the unreacted terephthalic acid and/or DMF out of the pores, the solvent exchange (purification) step was carried out via soxhlet extraction with methanol (200 ml) for 3 days. Following the purification step, wet CuTPA powder was kept under vacuum overnight prior to activation. The sample was activated at 160 °C with heating ramp of 50 °C for 1 h, 100 °C for 1 h and 160 °C for 24 h (Çiçek 2014).

4.2.2. Synthesis of Aluminum Terephthalate (AlTPA)

The solvothermal synthesis studies of AlTPA were directed in IYTE (Angı 2016). First, with the mixture molar composition of 1 $Al(NO_3)_3$:1.48 TPA:184.5 DMF, aluminum nitrate nonahydrate ($Al(NO_3)_3 \cdot 9H_2O$) (1.85 g) and TPA (1.21 g) were dissolved in DMF (70ml) under stirring at 330 rpm at room temperature for 24 h. In crystallization step, the solution was transferred to a Teflon-lined stainless steel autoclave and heated directly up to 130 °C in oven (Binder ED 53 and Memmert 100-800) for 72 h. After cooling the mixture, centrifugation (Hettich Rotofix 32) at 3000 rpm for 25 min was completed and the resulted solid phase was dried at room temperature overnight in vacuum (-1.0 bar). Purification step was directed via soxhlet extraction with hot (72 °C) methanol (200 ml) for 20 h. After samples were dried overnight, AlTPA was activated under vacuum (-1.0 bar) 130 °C for 72 h.

4.2.3. Synthesis of Titanium Terephthalate (TiTPA)

The synthesis studies of TiTPA were executed in Ege University (Çalışkan 2016) The solvothermal synthesis was began with dissolving TPA (16.61 g) into methanol (50 ml) and DMF (450ml) mixture (1 methanol: 9 DMF by volume). Then, Titanium (IV) isopropoxide (Ti[OCH(CH$_3$)$_2$]$_4$) (14.69 g) as Ti^{4+} source was added to the mixture at a molar ratio of 1 Ti[OCH(CH$_3$)$_2$]$_4$:2 TPA and stirred at room temperature for 30 min. The transparent solution was crystallized in glass-lined stirred reactor at 95 °C for 114 h. Following the cooling the resulted mixture at room temperature, the solid phase was separated by centrifuge (Nüve NF 1200R) at 6000 rpm for 20 min. For purification of TiTPA precipitate, first stirring with hot DMF (60 °C) three times, followed by the centrifugation of TiTPA/DMF mixture, 5 cycles of soxhlet washing with methanol under magnetic stirring (440 rpm) were conducted. After purification step, activation of TiTPA sample was completed in vacuum (-0.5 bar) oven (Nüve EV 018) at 150 °C with a heating ramp of 50 °C for 1 h, 100 °C for 1 h and 150 °C for 28 h.

4.2.4. Synthesis of Zinc Terephthalate (ZnTPA)

The solvothermal synthesis studies of ZnTPA were conducted in Ege University (Çalışkan 2016). The crystallization step was started with dissolving of zinc acetate dihydrate (Zn(CH$_3$COOH)$_2$ $\cdot$ 2H$_2$O) (3.398 g) and TPA (1.013 g) at a molar ratio of 1 Zn^{2+}:1.5 in DMF (80 ml) under stirring at room temperature for 30 min. Crystallization was taken place in glass-lined reactor under stirring at 95 °C for 72 h. After cooling the resulted mixture at room temperature for 24 h, centrifugation (Nüve NF 1200R) at 6000 rpm for 20 min was performed to separate the white solid phase. Purification step was started with washing the precipitate with hot (60 °C) DMF three times on magnetic stirrer at 440 rpm for 24 h. Following DMF washing, precipitate was processed to soxhlet extraction with methanol for 5 cycles. Activation of ZnTPA sample was completed in vacuum oven (Nüve EV 018) up to 150°C with a heating ramp of 50 °C for 1 h, 100 °C for 1 h and 150 °C for 24 h.

4.3. Characterization Methods of MOFs

Investigation of textural properties of the synthesized CuTPA, AlTPA, TiTPA and ZnTPA MOFs were carried out by using volumetric adsorption instrument (Micromeritics ASAP 2010 M). Nitrogen adsorption and desorption isotherms of samples were measured at 77.35 K at low pressure dose 10 cm^3/g STP. Prior to each measurement, adsorbents were degassed considering their thermal stabilities; CuTPA samples were degassed at 160 °C, AlTPA at 130 °C, TiTPA and ZnTPA at 150 °C for 24 h. The surface areas were calculated by Langmuir and Brunauer–Emmett–Teller (BET) method, the micropore volumes and the average pore diameters were calculated using Barrett-Joyner-Halenda (BJH) model and Horvath–Kawazoe method, respectively. The surface morphology and particle size of the crystalline samples were evaluated by scanning electron microscope (SEM, FEI QUANTA 250 FEG) with different magnifications under secondary electron (SE) and back scatter electron (BSE) detectors without any deposition. Thermal stability of MOF samples was determined by Thermogravimetric analysis (TGA, Shimadzu TGA-51) with 10 °C/ min heating rate under air flow at a rate of 40 mL/min. Examination of bounded groups and the interaction between atoms were accomplished by Fourier Transform Infrared spectrophotometer (FTIR, Shimadzu 8201) via preparation the pellets composed of MOF samples (1.5 mg) and KBr (148.5 mg). Crystallographic structure of the MOF powders was demonstrated by X-ray diffraction (XRD, Philips X' Pert Pro Diffractometer) with a scan speed of 2°/min and a step size of 0.002° in 5-85° using CuKα radiation (λ = 1.5418 Å).

4.4. Packed Bed Adsorption Studies

Adsorption and desorption studies on synthesized MOFs were carried out in a home-made system (Figure 4.1). The system includes gas (hydrogen, helium, carbon dioxide, methane, carbon monoxide) preparation part, three way valves (VTP1, VTP2 and VTP3), mass flow controllers (MFC1 and MFC2), manifold (M1), fixed bed adsorption column associated with heater and back pressure regulator (BPR), and gas chromatograph (GC-Agilent 7890A).
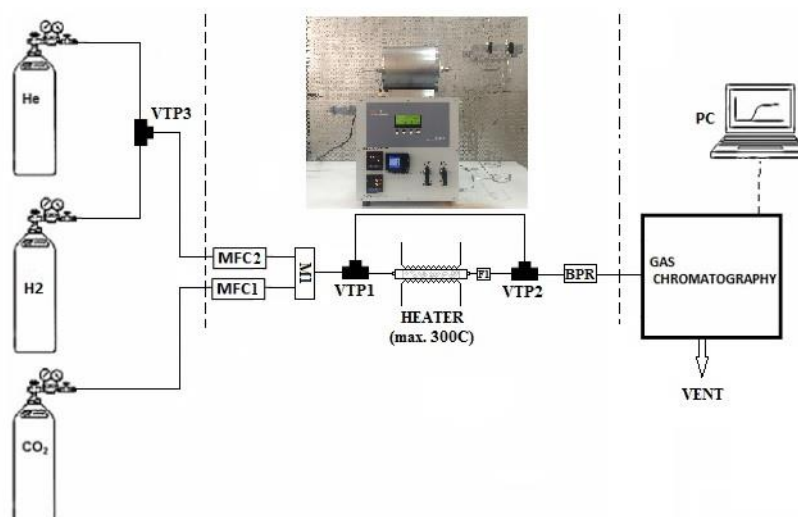
Figure 4.1. Gas adsorption desorption system; three way valves: VTP1, VTP2, and VTP3, mass flow controllers: MFC1 and MFC2, manifold: M1, back pressure regulator: BPR

In pure gas adsorption studies, high-purity CO_2, CH_4 and CO were used combined with hydrogen carrier flow (equimolar combination: 50% adsorptive gas-50% carrier gas) at three different feed flows; 10, 20 and 30 mL/min total and at three bed operating pressures; 1, 5 and 10 bar. First, the gases were sent to MFCs to measure and set the specified flow rates. After mixing of gases in manifold, gases were directed through VTP1 depending on the selection of gas direction (bypass or fixed bed column). Bypass line was used to check the stability of gases at a desired flow rate and mixing ratio (i.e., equimolar). Adsorption was started once the stability of gases on bypass line was ensured, then the way of gas flow was directed from bypass to packed bed column. The operating pressure of the bed was maintained by back pressure regulator (BPR, Bronkhorst) and operating temperature was set and read on digital temperature controller on the bed. The time dependent concentration change of the gases was analyzed by chromatographic method (GC). Gas chromatograph placed at the outlet of the column comprises two thermal conductivity detectors (TCDs): front and back with two carrier gases (helium front: 40 mL/min, nitrogen-back: 40 mL/min). Thee quartz wool was used at the both end of the packed bed to prevent sweeping of the MOF particles. Prior to each adsorption experiment, desorption was carried out by sending helium purge flow throughout the bed at a flow rate and at bed pressure same as the corresponding adsorption operating conditions. Prior to each experiment, in other words after completing the adsorption and

desorption cycle, overnight regeneration of adsorbent packed bed was conducted at atmospheric pressure under 20 mL/min helium flow and at temperatures specific to each MOF. The regeneration temperatures were determined based on the thermal characteristic of the adsorbents and higher temperature than adsorbent activation temperature was avoided. For example, the CuTPA packed bed was regenerated at 160 °C, AlTPA at 130 °C, TiTPA and ZnTPA at 150 °C.

In binary gas adsorption experiments, same procedure with the pure gas adsorption studies was followed using equimolar gas mixtures of CO_2/CH_4 at three different total flow rates (i.e., 10, 20 and 30 mL/min) and bed pressures (i.e., 1, 5 and 10 bar). The bed characteristics packed with CuTPA, AlTPA, TiTPA and ZnTPA adsorbents and the properties of these adsorbents were summarized in Table 4.2.

Table 4.2. Adsorbent packed bed characteristics and adsorbent properties

	CuTPA (powder)	AlTPA (powder)	TiTPA (powder)	ZnTPA (powder)
Column length (cm)	24.8	24.5	17.7	24
Column diameter (cm)	0.67	0.60	0.80	0.65
Adsorbent layer length (cm)	10.8	15.5	13.0	14.6
Bed volume (cm³)	3.81	4.4	6.5	4.8
Void volume (V_{bed}-V_{solid}, (cm³))	2.78	4.46	4.61	3.91
Mass of adsorbent (g)	4	2.5	3	3
[a]Micropore volume (cm³/g)	0.26	0.68	0.53	0.31
[b]Average pore diameter (Å)	6.0	9.9	6.2	8.5
Surface area (S_{Lang}, (m²/g))	776	1330	1835	1023
Surface area (S_{BET}, (m²/g))	530	1270	1237	778

[a]BJH method was used for calculation
[b]Horvath-Kawazoe method was used for calculation.

The differential material balance around the adsorbent packed bed,

$$\frac{dn_a}{dt} = F_{a0} - F_a \tag{4.1}$$

where n_a was the amount adsorbed in mmol,

$$dn_a = F_{a0} \int_0^t (1 - \frac{F_a}{F_{a0}}) dt \qquad (4.2)$$

Defining X_a as the mole fraction of component a in the gas phase, $X_a = F_a/F_{a0}$ or $X_a = C/C_0$ and regarding experimental breakthrough curves, integration of Equation 4.2 from t=0 to time when equilibrium reached gave the mean residence time, τ_a (min), for pure component gas systems (CO_2/H_2, CH_4/H_2 and CO/H_2 or CO_2/He, CH_4/He and CO/He) in Equation 4.3.

$$\tau_a = \int_0^t (1 - \frac{C}{C_0}) dt \qquad (4.3)$$

Due to the roll-up area of CH_4 in binary gas mixture of CO_2/CH_4 the breakthrough curves were obtained as in Figure 4.2.
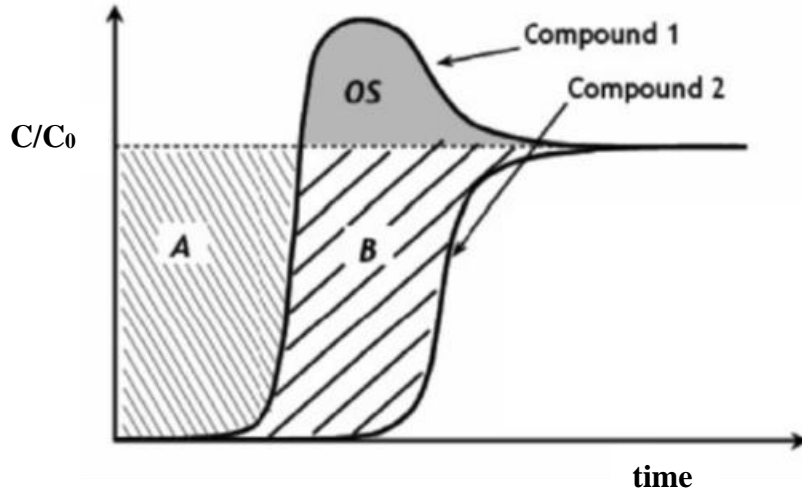
Figure 4.2. Typical adsorption breakthrough curves of binary mixture of CO_2/CH_4
(Source: adapted from Silva et al. (2014))

where compound 1 and 2 were CH_4 and CO_2, respectively. The τ_{CH4} for binary gas mixture were found by Equation 4.4 (Silva et al. 2014),

$$\tau_{CH4} = Area(A) - Area(OS) \qquad (4.4)$$

Then, the amount adsorbed of component a by per gram of specific adsorbent, q_a in mmol/g was calculated by Equation 4.5.

$$q_a = \frac{\left(F_{a0} \cdot \tau_a - \frac{(V_b - V_s) P_b X_a}{R T_b} \right)}{m_{ads}} \qquad (4.5)$$

where, V_b: bed volume (mL); V_s: solid volume (mL); C: concentration of CO_2 at time t, C_0: CO_2 concentration at bed inlet; P_b: bed operating pressure (bar); F_a: CO_2 flow rate at time t (mmol CO_2/min); F_{a0}: the CO_2 flow rate in feed (mmol CO_2/min); T_b: bed temperature (K); R: ideal gas constant (0.0831 mLbar/mmol.K) and m_{ads}: mass of the adsorbent (g). Consequently, experimental adsorption isotherms were obtained by the calculation of adsorbed gas amounts at each defined pressure and feed flow rate over MOFs.

For pure component adsorption studies, two adsorption isotherm models; Langmuir (Equation 3.13) and virial (Equation 3.18) models in non-linear form were fitted to the experimental adsorption isotherms. The purpose was to minimize the error between experimentally measured adsorbed amounts and theoretical data calculated by the models and model parameters were assessed by using solver add-in with Microsoft Excel. In addition to minimum error, the highest correlation coefficient (R^2) was also intended. The minimization procedure considered the minimum value of the objective function which was sum of squares of the errors (SSE or ERRSQ) (Allen et al. 2003, Boulinguiez, Le Cloirec, and Wolbert 2008, McKay et al. 2014, Subramanyam and Das 2014, Tari et al. 2016a) defined in Equation 4.6.

$$ERRSQ = \sum_{i=1}^{n} \left(q_{experimental} - q_{model} \right)_i^2 \qquad (4.6)$$

A confidence interval is an indicator of the measurement's precision. Besides, it shows how close the measurement will be to the original estimate in case of repeated trials. The most commonly preferred confidence level is 95 percent was used and the procedure below was followed in the calculations (Smithson 2003).

The sample mean, $\bar{x}$,

$$\bar{x} = \frac{\sum x}{N} \qquad (4.7)$$

The number of repeated measurements was N and the standard deviation σ calculated as,

$$\sigma = \sqrt{\frac{\sum (x-\bar{x})^2}{N}} \qquad (4.8)$$

The margin of error for small set of data (N<30) was calculated as;

$$\text{Margin of error} = t_{.95} \frac{\sigma}{\sqrt{N}} \tag{4.9}$$

Finally, the confidence interval was represented as,

$$\text{Confidence interval} = \bar{x} \pm t_{.95} \frac{\sigma}{\sqrt{N}} \tag{4.10}$$

CHAPTER 5

RESULTS AND DISCUSSION

5.1. Characterization of MOFs

Within the scope of the TUBITAK (112M294) project successfully concluded in IYTE and EGE University, numbers of CuTPA, AlTPA, TiTPA and ZnTPA samples were synthesized at different conditions and several parameters (i.e., crystallization time and temperature, purification method, activation time and temperature) that directly influence the MOF characteristics were investigated in detail (Çiçek 2014, Angı 2016, Çalışkan 2016). In this section, the characterization results were demonstrated only in the interest of the synthesized MOFs with the highest surface areas (i.e., CuTPA (S_{Lang}: 776 m^2/g); AlTPA (S_{Lang}: 1330 m^2/g); TiTPA (S_{Lang}: 1834 m^2/g) and ZnTPA (S_{Lang}: 1023 m^2/g)) that packed into the fixed bed for further adsorption studies.

5.1.1. Thermogravimetric Behavior of MOFs

The thermogravimetric profiles of CuTPA, AlTPA, TiTPA and ZnTPA were demonstrated in Appendix, Figure A.1. The CuTPA showed one step weight loss without significant weight difference up to 336 °C. After that, a sharp increase indicated that CuTPA structure was collapsed due to the removal of structural terephthalic acid linkers from the framework. The two steps weight loss of AlTPA corresponded to the release of the guest molecules (100 °C for water and around 200 °C for DMF) and followed by transformation into amorphous Al_2O_3 around 550 °C (Loiseau et al. 2004, Chen et al. 2012). Similarly, TiTPA and ZnTPA displayed two steps weight loss regions due to evacuation of guest molecules, then degradation of frameworks and production of TiO_2 (Moreira et al. 2012, McNamara et al. 2013) and ZnO (Segakweng et al. 2016), respectively. The thermal stability order was found to be AlTPA>ZnTPA>TiTPA>CuTPA. However, the effectiveness of the purification step to remove guest molecules was highest for CuTPA indicated by the lowest weight loss in a single step as a result of longer soxhlet extraction time.

5.1.2. X-ray Powder Diffraction Pattern of MOFs

The XRD patterns of the CuTPA, AlTPA, TiTPA and ZnTPA were shown in Appendix, Figure A.2. The CuTPA demonstrated the intense characteristic peaks at 8.3, 8.6, 12 and, 16° (2θ) which were closely compatible with literature (Carson et al. 2009). Characteristic signals of AlTPA were found particularly around 10–20° and the main peak towards 8.67°, indicating slightly different XRD pattern reported in literature due to the to the presence of DMF molecules inside the pores (Loiseau et al. 2004, Rallapalli et al. 2011). The XRD analysis of TiTPA illustrated the characteristic peaks of TiTPA MOF at 6.7, 9.8 and 12° (2θ) (McNamara et al. 2013), proving the well-formed TiTPA crystal structure. The main peaks of ZnTPA at 7.1, 9.7, 13.9° (2θ) that were well-matched to literature with some shifting in peak locations probably due to alterations of atomic orientation in crystal planes by solvent molecules that fill the micropores of ZnTPA (Saha, Wei, and Deng 2009).

5.1.3. Fourier Transform Infrared Spectroscopy Analysis of MOFs

The FTIR analysis of CuTPA and AlTPA were given in Appendix, Figure A.3 and that of TiTPA and ZnTPA were in Figure A.4. For CuTPA, the absorption band in the region between 1280 and 1650 cm^{-1}, characteristic carboxylate and phenyl vibrational bands were observed. The absence of DMF peaks at 675 cm^{-1} (OCN bending) and 1663 cm^{-1} (CO stretching) confirmed the effective removal of solvent from MOF structure. The strong bands at around 1280 cm^{-1}, 1390 cm^{-1}, and 1570 cm^{-1} attributed to symmetric and asymmetric stretching of carboxylate groups coordinated to Cu^{II} center, thereby approving the CuTPA product of the synthesis (Carson et al. 2009). The AlTPA exhibited absorption bands at 1414 and 1435 cm^{-1} and bands at 1503 and 1604 cm^{-1} for symmetric and asymmetric $-CO_2$ stretchings, respectively. These values were consistent with the presence of COO^- groups that were coordinated to Al^{3+} center (Loiseau et al. 2004). For TiTPA the band at 1673 cm^{-1} was attributed to carboxyl group from free aromatic carboxylic acid as the sign of unreacted TPA. The out-of plane vibrations in the region of 1300-700 cm^{-1} confirmed the formation of TiTPA MOF structure (Rada et al. 2015). ZnTPA exhibited the peaks occurring around 400–530 cm^{-1} characteristic of ZnO molecules (Arjmandi and Pakizeh 2014). Absorption bands located at around 1507 cm^{-1}

were assigned to the v_{as}(COO) asymmetric stretching. These values were consistent with the presence of COO$^-$ groups that are coordinated to zinc (Hermes et al. 2006).

5.1.4. Scanning Electron Micrograph of MOFs

The SEM images of CuTPA, AlTPA, TiTPA and ZnTPA were illustrated in Appendix, Figure A.4. The external morphology of the CuTPA reflected a cubic layered sheet-like particle with some degree of agglomeration as a result of impurities such as DMF and unreacted TPA linkers in crystalline structure, the micrographs were comparable to literature (Phan et al. 2013, Tari et al. 2015). The AlTPA demonstrated irregular shaped crystals in dispersed phases similar to results obtained by Chen et al. (2012), Chen et al. (2013), and Abedini, Omidkhah, and Dorosti (2014). TiTPA showed round plate and cubic shaped TiTPA crystals, while ZnTPA presented the regular cubic shaped crystals consistent with the literature (Rada et al. 2015, Saha, Wei, and Deng 2009).

5.1.5. Textural Analysis of MOFs

The textural characteristics of MOF adsorbents used in the calculations were stated in Table 4.2.

5.2. Packed Bed Adsorption Studies on MOFs

After the synthesis and characterization of the CuTPA, AlTPA, TiTPA and ZnTPA MOFs having the highest surface areas were packed into bed for detailed adsorption studies. For each MOF the adsorption studies were categorized into two parts. In the first part of the study, the experimental breakthrough curves of stream methane reformer (SMR) components on aforementioned MOFs were obtained under different flow rates and bed pressures, hence the dynamic behavior of the adsorption bed was investigated in detail. The second part included the determination of the adsorption capacities of each MOF for SMR components in cases for pure and binary gas systems followed by fitting the Langmuir and virial adsorption isotherm models to pure experimental data and investigation selective separation of SMR components on MOFs.

5.2.1. Adsorption Studies on CuTPA

The change in molar percentages for equimolar (50/50%) CO_2 and H_2 system at a total flow rate of 30 mL/min and at 1 bed pressure and 303 K was stated in Figure 5.1. Only CO_2 was adsorbed by CuTPA for 2 min and the mole percent of CO_2 was read as 0, while the mole percent of H_2 was 100%. The time (2 min) when the breakthrough curve of CO_2 rose up from 0 is called as the breakthrough time or breakpoint of CO_2. Between 2 and 6 min, the effluent CO_2 percentage increased while the H_2 decreased. After 6 min the equilibrium reached and the CuTPA became saturated, the mole percentages of CO_2 and H_2 were read constant at a value which was the same as the initial (feed) concentration as 50 and 50%.

The breakthrough behaviors of CO_2 and H_2 in case of higher pressures (5 bar and 10 bar) were shown in Figure 5.2. The increase in bed operating pressure resulted in the longer breakthrough times; at 5 bar the breakpoint of CO_2 was found as 5 min while at 10 bar it extended to 9 min. Up to these points the percent CO_2 mole was noticed as 0 and H_2 was 100%, indicating that CuTPA does only adsorb CO_2, not H_2. Even though, considering H_2 storage applications, hydrogen adsorption studies on copper based MOFs are present in literature (Sun et al. 2006, Yan et al. 2009, Lin et al. 2012), but here it was not the case. Because, literature review revealed that copper based MOFs could adsorb H_2 only at very low temperatures (77 K), not at room temperature (303 K). Besides, comparison between Figure 5.1 and Figure 5.2 showed that the time when the mole percentage of CO_2 and H_2 effluent read same as the initial feed concentration (50/50%) extended with increasing bed pressure; from 6 min at 1 bar to 11 min at 5 bar and to 33 min at 10 bar.
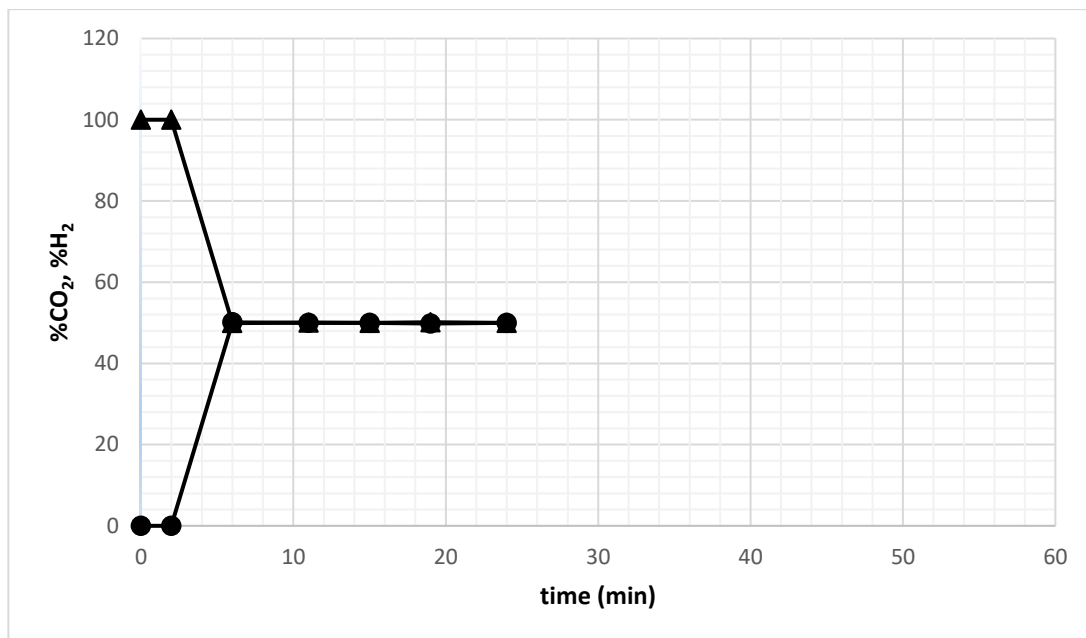
Figure 5.1. Molar percentages of CO_2 and H_2 effluent over CuTPA at 303 K (Total CO_2/H_2 flow rate: 30 mL/min; CO_2: ● and H_2: ▲; Bed pressure: 1 bar)
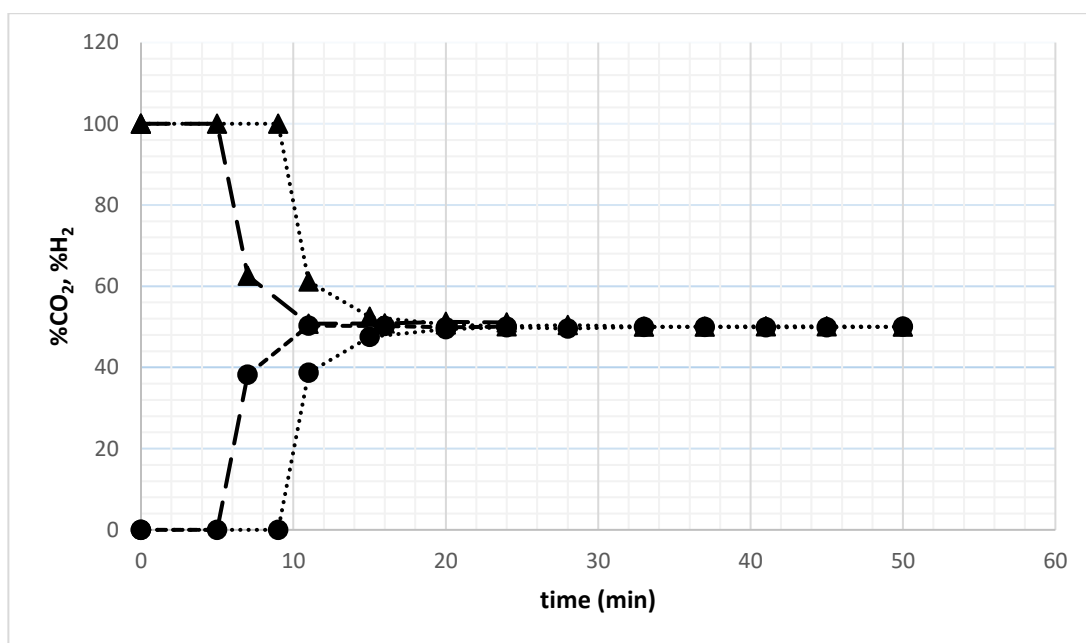
Figure 5.2. Molar percentages of CO_2 and H_2 effluent over CuTPA at 303 K (Total CO_2/H_2 flow rate: 30 mL/min; CO_2: ● and H_2: ▲; Bed pressures: 5bar (‑‑‑‑‑) and 10 bar (·········))

The effect of pressure on the CuTPA packed bed dynamics at three different total CO_2/H_2 feed flow was represented in Appendix, Figure A.6 (F_{total}: 30 mL/min), Figure A.7 (F_{total}: 20 mL/min) and Figure A.8 (F_{total}: 10 mL/min). As only CO_2 component was

adsorbed by CuTPA in CO_2/H_2 system, the breakthrough curves of CO_2 were investigated instead of H_2. At a constant feed flow rate, the increase in bed pressure extended the breakthrough point of CO_2 (t_{break}), consequently the time required for the saturation of adsorbent (t_{sat}) prolonged. For example, feeding the bed at a rate of 10 mL/min (Figure A.8), at 1 bar CO_2 left the column immediately, so the breakthrough point of CO_2 observed at time zero, while the breakpoint was reached in 10 min at 5 bar, and in 25 min at 10 bar. Also, at constant pressure the decrease in feed flow from 30 mL/min (Figure A.6) to 10 mL/min (Figure A.8) the breakpoint shifted from 5 min to 10 min at 5 bar and from 9 min to 25 min at 10 bar. It was seen that the breakthrough lines at each specified pressure diverged with decreasing the flow rate as the external mass transfer resistance was experienced at the 10 mL/min of feed rate.

The effect of feed flow rate on the bed dynamics were examined at three different bed pressure in Appendix, Figure A.9, A.10 and A.11. At atmospheric pressure (Figure A.9) CO_2 exits the bed instantly and the breakpoint of CO_2 originated from zero for all feed flow rates, but the time required for saturation of CuTPA (when C_{out}/C_{in}: 1.0) extended with the decrees in feed flow. At 1 bar, the equilibrium (t_{sat}) reached in 6 min for 30 mL/min, in 11 for 20 mL/min and in 19 min for 10 mL/min of flow rate. With the increase in bed pressure to 5 bar (Figure A.10) the breakpoint of CO_2 shifted to 5 min for 30 mL/min, to 7 min for 20 mL/min and to 10 min for 10 mL/min feed rate, while the saturation time of CuTPA extended to 11 min (30 mL/min), to 17 min (20mL/min) and 38 min (10 mL/min). At 10 bar (Figure A.11) the breakthrough lines at each feed flow became much more distant to each other, indicating that the breakpoint and saturation time prolonged and the effect of external mass transfer especially at low flow rates (10 mL/min) strongly experienced. The desorption curves of CO_2 under different helium flow rates and bed pressures were given in Appendix, Figure A.12.

The dynamic parameters of CuTPA packed bed and the experimental adsorbed amount of CO_2 calculated from the breakthrough curves were given in Table 5.1. The time allotted for the pressurization of the bed (t_{pres}) decreased with the increase in feed flow rate. At a flow rate of 10 mL/min the time required to pressurize bed to 10 bar was 25 min while at 30 mL/min it was reduced to 9 min. Also, at constant flow rate of helium purge gas the time for complete CO_2 removal (desorption time, t_{des}) rises with increasing pressure, while at constant bed pressure t_{des} reduced with the increase in helium flow accompanied with the decrease in cycle time. At 10 bar, in case of 10 mL/min of helium

flow the complete removal of CO_2 was achieved in 56 min and it reduced to 21 min with increasing the helium flow up to 30 mL/min. Moreover, at constant CO_2/H_2 feed flow (10 mL/min), the unused bed length (H_{UNB}) was found about six times lower at 10 bar compared to 1 bar as a direct relationship between the time CO_2 spent in the bed (the mean residence time of CO_2, τ_{CO2}) that was increased from 4 min (1 bar) to 28 min (10 bar). The increase in mean residence time of CO_2 in the CuTPA bed directly resulted in the increase in adsorbed CO_2 amount (q_{CO2}). Eventually, the highest adsorbed amount of CO_2 was calculated at highest operating feed flow and bed pressure (30 mL/min and 10 bar) as 1.61 mmolCO_2/gCuTPA at 303 K, while the CO_2 adsorption capacity of CuTPA synthesized by Anbia et al. (2014) was only 0.7 mmolCO_2/gCuTPA at 30 bar and 298 K.

To determine the confidence interval of the calculated adsorbed gas amount, at constant total feed flow of 30 mL/min, at each bed pressure six trials were carried out and small margin of errors were found. However, the higher pressures the higher margin of errors were calculated (Table 5.1) as a result of increasing the data points of experimental breakthrough curves accompanied by longer saturation time.

Table 5.1.   The dynamic parameters of CuTPA packed bed and calculated adsorbed amount of CO_2 from experimental breakthrough curves at different bed operating conditions

Total flow rate (mL/min)	Pressure (bar)	t_{pres} (min)	t_{break} (min)	t_{sat} (min)	t_{des} (min)	t_{cycle} (min)	H_{UNB} (cm)	τ_{CO2} (min)	q_{CO2} (mmolCO_2/gCuTPA)
10	**1**	0	0	19	8	27	10.2	4	0.17
	5	10	10	38	34	82	3.1	14	0.55
	10	25	25	57	56	138	1.6	28	1.12
20	**1**	0	0	11	5	16	9.9	3	0.25
	5	7	7	17	17	41	2.7	9	0.85
	10	14	14	37	30	81	1.7	16	1.49
30	**1**	0	0	6	8	14	9.9	2	0.37 ± 0.009
	5	5	5	11	9	25	3.0	7	1.01 ± 0.012
	10	9	9	33	21	63	2.2	20	1.61 ± 0.018

The Langmuir and virial adsorption models fitted to experimental isotherm data of CO_2 on CuTPA was represented in Figure 5.3. With the increase in CO_2/H_2 feed flow and bed pressure, the adsorbed amount of CO_2 was sharply increased, even at the highest bed operating pressure (10 bar) and highest feed rate (30 mL/min) the adsorbed amount of CO_2 was not reached at a constant value, implying that the CuTPA adsorbent was not saturated yet and the CO_2 adsorption capacity of CuTPA could be much higher than 1.61 $mmolCO_2$/CuTPA at higher pressures and feed flows. Besides, it was shown that both models fitted well with the experimental data and the corresponding model parameters were given Table 5.6.
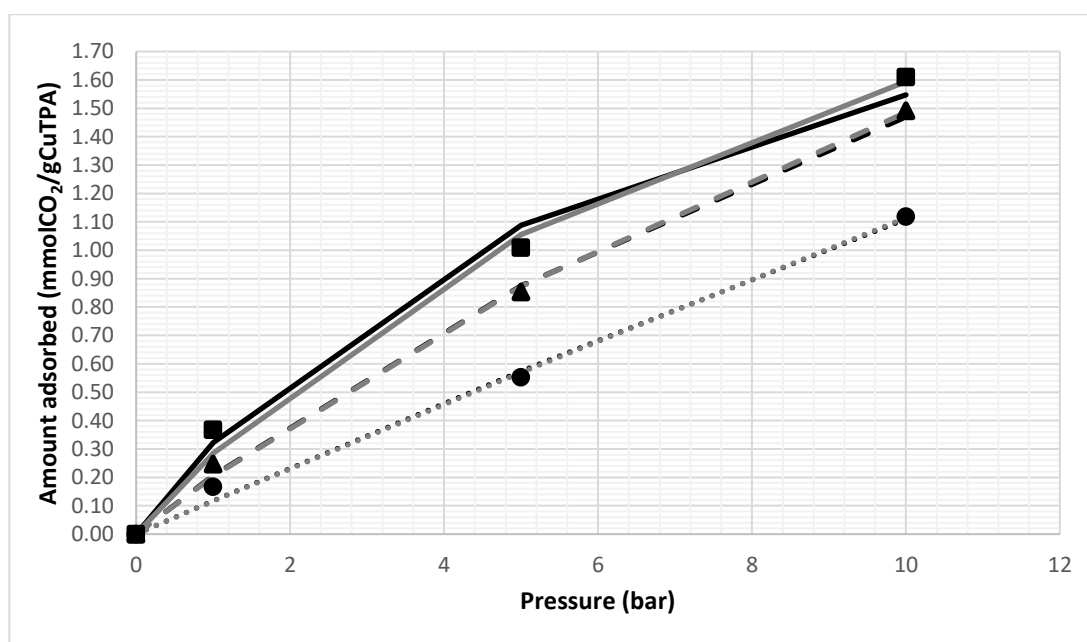
Figure 5.3. Adsorption isotherms of CO_2 on CuTPA at 303 K (Symbols: experimental data at CO_2/H_2 total flow rate of 10 mL/min (●), 20 mL/min (▲) and 30 mL/min (■); black lines: Langmuir model, grey lines: virial model applied for total feed flow rates of 10 mL/min: (·········), 20 mL/min: (----) and 30 mL/min: (——))

The molar percentages for equimolar (50/50%) CH_4 and H_2 system at a total flow rate of 30 mL/min and three different bed pressures was stated in Figure 5.4. With the increase in bed pressure the first time that CH_4 leaves the bed and the time that molar percent of CH_4 at the exit of the bed reaches the inlet value (50%) were extended. Besides, it was observed that similar to CO_2/H_2 system adsorption studies (Figure 5.1 and Figure 5.2), for CH_4/H_2 system CuTPA only adsorbed CH_4 component, not H_2 at 303 K.

Figure 5.4. Molar percentages of CH_4 and H_2 effluent over CuTPA at 303 K (Total CH_4/H_2 flow rate: 30 mL/min; CH_4: ● and H_2: ▲ ; Bed pressures: 1bar (——), 5bar (– – – –), 10 bar (·········))

The effect of pressure and CH_4/H_2 feed flow on CH_4 breakthrough curves was established in Figure 5.5. In case of high feed flow (30 mL/min) the curves were strictly parallel to each other at each bed pressure, indicating that at high flow rates the CH_4 adsorption mechanism and dynamics was independent of pressure and external mass transfer resistance was eliminated. At 20 mL/min feed rate the parallel tendency of breakthrough curves almost maintained, but decreasing the rate down to 10 mL/min the curves became distant especially for curve of 10 bar at which external mass transfer resistance was experienced. At low pressure (1bar) curves belongs to 30 and 20 mL/min feed rate overlapped, suggesting that similar CH_4 adsorption mechanism takes place at these conditions. However, at high pressures decrease in feed rate directly affected the bed dynamics and the curve of 10 mL/min separated as a result of external mass transfer resistance. With the increase in bed pressure the distance between the CH_4 breakthrough curves became more apparent even for high feed flow case with negligible external mass transfer resistance, therefore the adsorption mechanism was possibly under the control of the internal mass transfer at high pressures.

Figure 5.5. CH$_4$ adsorption breakthrough curves over CuTPA (Total CH$_4$/H$_2$ feed flow rate: 30 mL/min (———), 20 mL/min (-----) and 10 mL/min (··········); Bed pressures: 1bar (●), 5bar (■) and 10 bar (▲))

The time based dynamic parameters of CuTPA bed and the calculated adsorbed amount of CH$_4$ calculated were given in Table 5.2. As corroborated by CH$_4$ breakthrough curves obtained at different bed operating conditions, at CH$_4$/H$_2$ feed flow, the increase in pressure extended time for bed pressurization, time for breakpoint and mean residence time of CH$_4$ inside the bed, consequently rise in the adsorbed CH$_4$ amount. The highest amount of CH$_4$ adsorbed by CuTPA was calculated as 1.50 mmolCH$_4$/gCuTPA at 10 bar and 30 mL/min feed flow, whereas the CH$_4$ adsorption capacity of CuTPA synthesized by Anbia et al. (2014) was 6.5 mmolCH$_4$/gCuTPA at 10 bar and 8.0 mmolCH$_4$/gCuTPA at 30 bar and 298 K. The Langmuir and virial model parameters calculated for CH$_4$ were given in Table 5.6. The experimental CH$_4$ adsorption isotherms and the fitted models were perfectly overlapped as shown in Figure 5.6. The increase in pressure and feed flow caused a steep increase in adsorbed CH$_4$ amount. Even at the highest pressure and feed rate operated in the study, the adsorbed amount of CH$_4$ was not reach a constant value, implying that the CuTPA was not saturated for CH$_4$, yet.

Table 5.2. The dynamic parameters of CuTPA packed bed and calculated adsorbed amount of CH$_4$ from experimental breakthrough curves at different bed operating conditions

| Total flow rate (mL/min)	Pressure (bar)	t_{pres} (min)	t_{break} (min)	t_{sat} (min)	H_{UNB} (cm)	τ_{CH4} (min)	q_{CH4} (mmolCH$_4$/gCuTPA)
10	1	0	0	10	5.4	4	0.16
	5	9	9	20	2.6	12	0.44
	10	22	22	32	1.3	24	0.93
20	1	0	0	9	9.8	2	0.18
	5	6	6	16	2.3	7	0.68
	10	13	13	23	1.4	14	1.33
30	1	0	0	6	9.8	1	0.16 ± 0.005
	5	4	4	19	3.1	5	0.80 ± 0.007
	10	9	9	15	1.7	10	1.50 ± 0.011

Figure 5.6. Adsorption isotherms of CH$_4$ on CuTPA at 303 K (Symbols: experimental data at CH$_4$/H$_2$ total flow rate of 10 mL/min (●), 20 mL/min (▲) and 30 mL/min (■); black lines: Langmuir model, grey lines: virial model applied for total feed flow rates of 10 mL/min: (·········), 20 mL/min: (-----) and 30 mL/min: (———))

The change in molar percent for equimolar (50/50%) CO/H$_2$ system at a total flow rate of 30 mL/min at different bed pressures was stated in Figure 5.7. As previously investigated for CO$_2$/H$_2$ and CH$_4$/H$_2$ systems in detail, it was ensured that the CuTPA adsorbed only CO component in CO/H$_2$ system at 303 K.
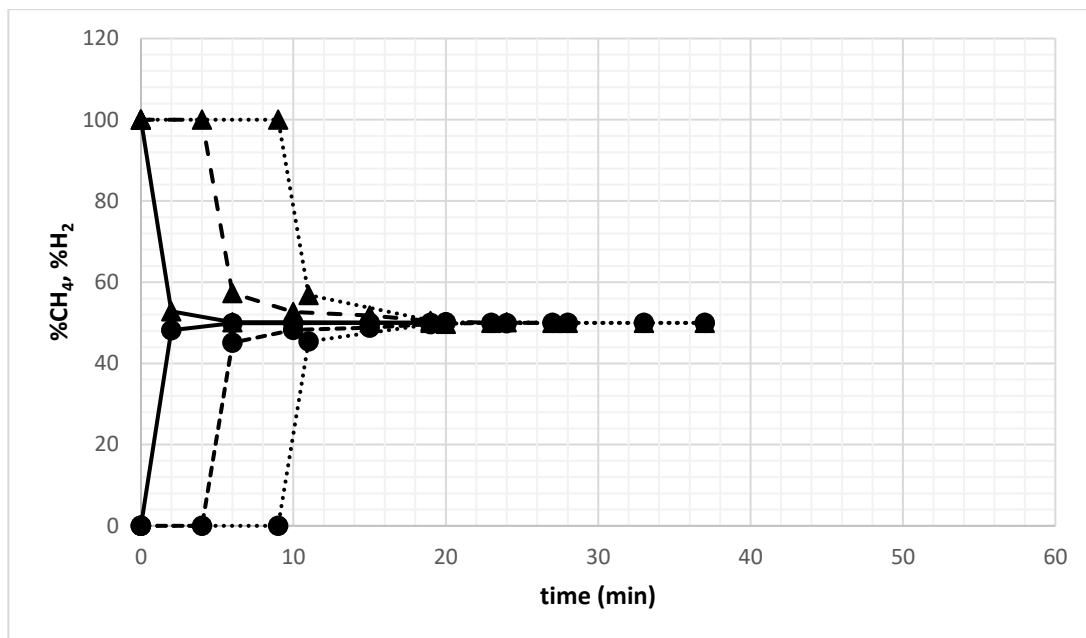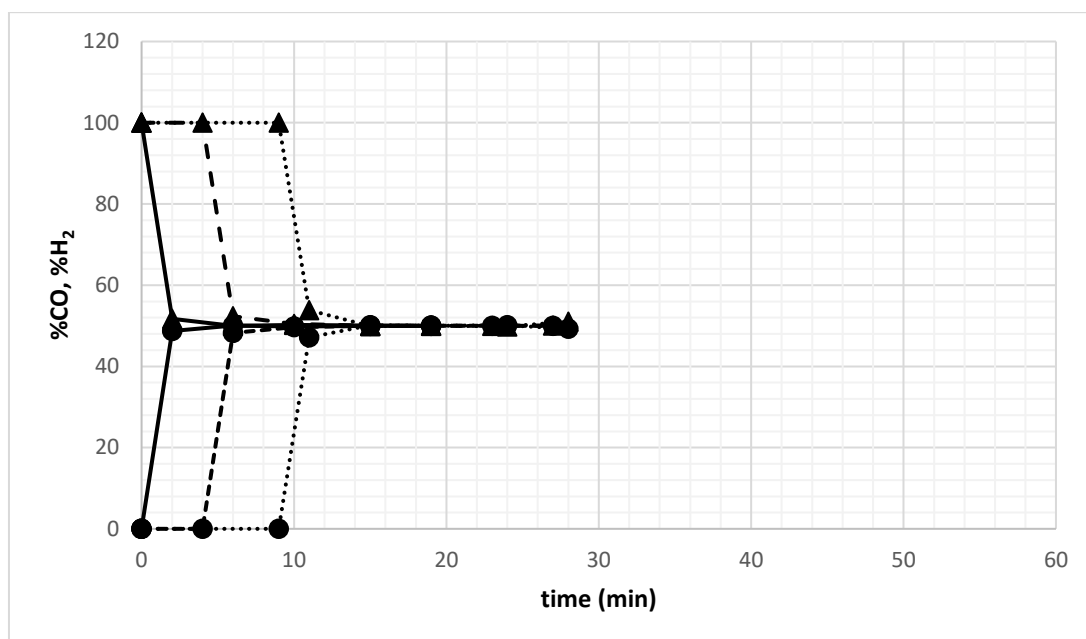
Figure 5.7. Molar percentages of CO and H$_2$ effluent over CuTPA at 303 K (Total CO/H$_2$ flow rate: 30 mL/min; CO: ● and H$_2$:▲; Bed pressures: 1bar (———), 5bar (-----) 10 bar (·········))

The change in CuTPA packed bed dynamics with total feed flow rate of CO/H$_2$ system and bed pressure given in Figure 5.8. At low bed pressure (1 bar), the change in feed flow did not affect the bed dynamics, the breakpoint of CO originates from time zero and the breakthrough lines overleaped for all three feed flows, hence the impact of mass transfer resistance was eliminated at low pressure regardless of the feed rate. With the increase in bed pressure the distance CO breakthrough lines specific to each feed flow became more apparent, at highest bed pressure (10bar) and lowest feed rate (10 mL/min) the bed dynamics changed noticeably, the breakpoint of CO and the saturation time of the adsorbent extended greatly. The desorption curves of CO was in Appendix, Figure A.13. The dynamic factors evaluated from CO breakthrough curves were exhibited in Table 5.3. The highest adsorbed CO amount was calculated as 1.47 mmolCO/gCuTPA at 10 bar and 303 K under 30 mL/min CO/H$_2$ feed flow, whereas the CO adsorption capacity of CuTPA synthesized by Anbia et al. (2014) was only 0.5 mmolCO/gCuTPA at 30 bar and 298 K. The experimental CH$_4$ adsorption isotherms with fitted Langmuir and virial models were demonstrated in Figure 5.9 and the model parameters were given in Table 5.6.
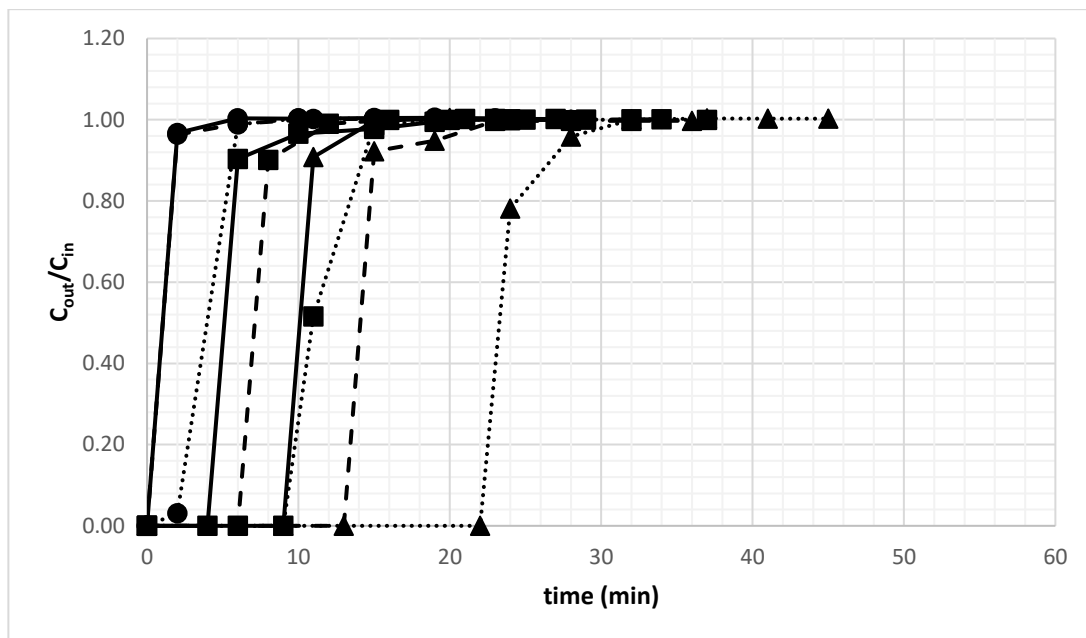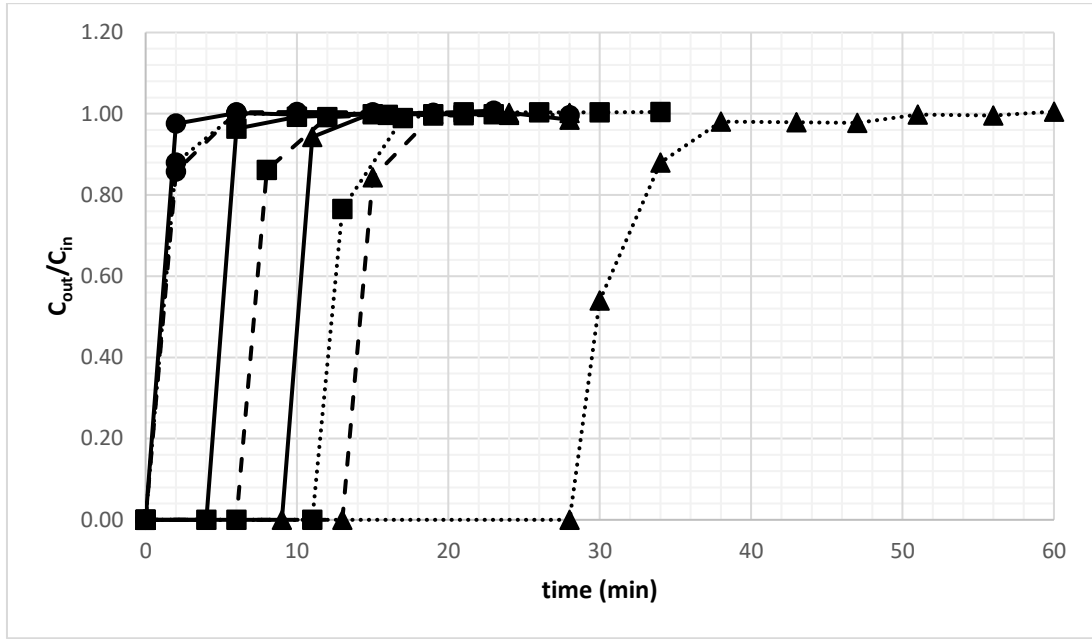
Figure 5.8. CO adsorption breakthrough curves over CuTPA (Total CO/H$_2$ feed flow rate: 30 mL/min (———), 20 mL/min (- - - -) and 10 mL/min (·········); Bed pressures: 1bar (●), 5bar (■) and 10 bar (▲))

Table 5.3. The dynamic parameters of CuTPA packed bed and calculated adsorbed amount of CO from experimental breakthrough curves at different bed operating conditions

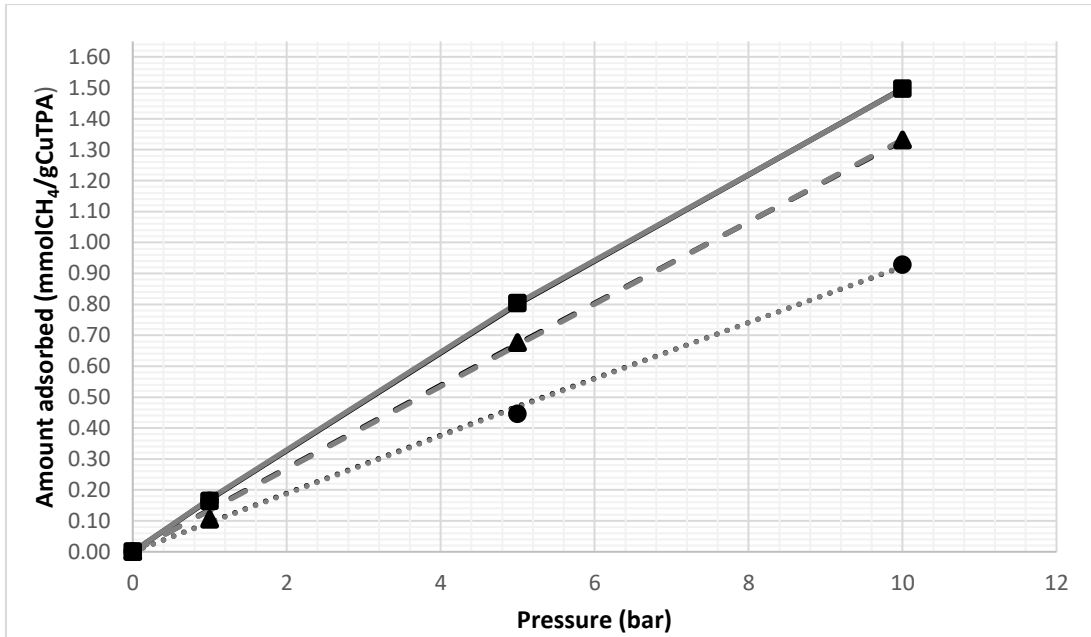| Total flow rate (mL/min)	Pressure (bar)	t_{pres} (min)	t_{break} (min)	t_{sat} (min)	t_{des} (min)	t_{cycle} (min)	H_{UNB} (cm)	τ_{CO} (min)	q_{CO} (mmolCO/gCuTPA)
	1	0	0	6	47	53	9.9	3	0.10
10	5	11	11	21	65	97	1.9	13	0.47
	10	28	28	51	64	143	0.9	29	1.09
	1	0	0	6	26	32	9.9	2	0.13
20	5	6	6	12	34	52	2.3	7	0.67
	10	13	13	19	40	72	1.5	14	1.30
	1	0	0	6	21	27	9.8	1	0.16 ± 0.021
30	5	4	4	10	21	35	2.6	5	0.74 ± 0.028
	10	9	9	15	26	50	1.6	10	1.47 ± 0.033
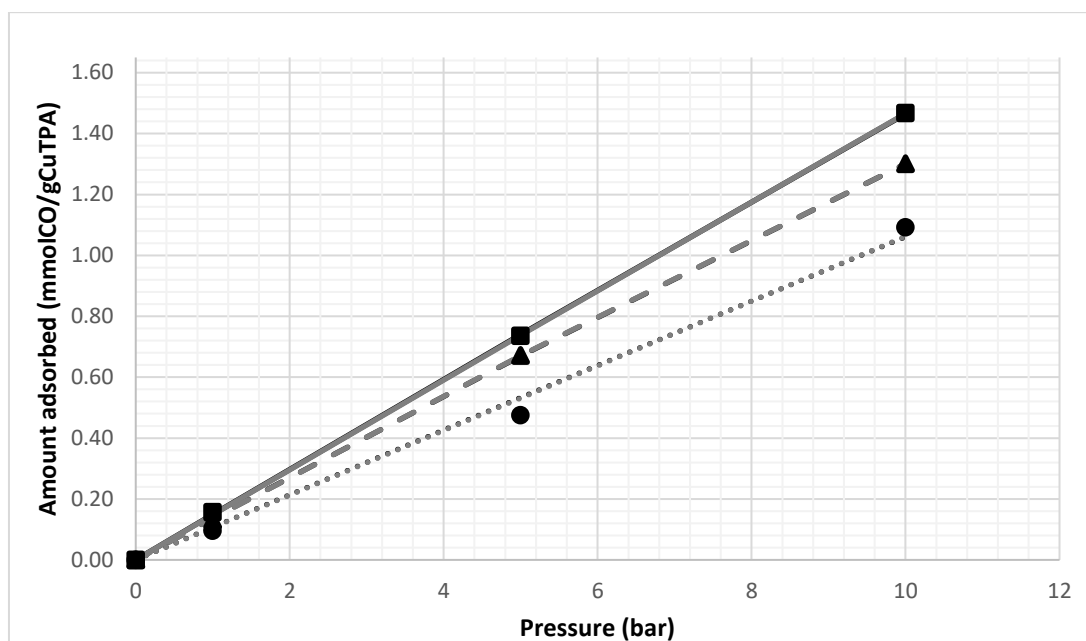
Figure 5.9. Adsorption isotherms of CO on CuTPA at 303 K (Symbols: experimental data at CO/H$_2$ total flow rate of 10 mL/min (●), 20 mL/min (▲) and 30 mL/min (■); black lines: Langmuir model, grey lines: virial model applied for total feed flow rates of 10 mL/min: (··········), 20 mL/min: (-----) and 30 mL/min: (——))

The comparison of adsorption capacity of CuTPA adsorbent for steam methane reformer off-gas components was given in Table 5.4. Under covered operating conditions, at constant flow rate the adsorbed CO$_2$, CH$_4$ and CO amounts was increased with rise in pressure; at constant pressure the rise in feed flow increases the adsorbed amounts, thus the highest CO$_2$, CH$_4$ and CO adsorption capacities of CuTPA was reached at 30 mL/min feed flow at 10 bar.

At each pressure and feed flow, the order of adsorbed gas amounts (from more adsorbed compound to the less) over CuTPA was found as CO$_2$>CH$_4$>CO. The order of adsorbed gas amounts was compatible with literature (Yang et al. 2012, Karra et al. 2013, Silva et al. 2013, Wu et al. 2014, Yang, Sitprasert, et al. 2015, Tari et al. 2016a, b) on copper based MOFs synthesized from different organic ligands and different synthesis routes. The reason of more favorable adsorption of CO$_2$ among CH$_4$ and CO relies on the molecular properties of the gases (Table 5.5). The kinetic diameter of CO$_2$ is the smallest which enables faster and easier penetration of CO$_2$ molecules inside the micropores of CuTPA. Besides, high quadrupole property of CO$_2$ leads to respectively stronger interaction between CO$_2$ molecule and the CuTPA surface that comprise of positive and negative charges of Cu^{2+} and COO$^-$. Although, CH$_4$ larger kinematic diameter than CO,

due to higher polarizability of CH_4 the interactions between CH_4 molecule and CuTPA surface are enhanced resulted in more favorable adsorption of CH_4 than CO molecule.

Table 5.4. Adsorbed amounts of CO_2, CH_4 and CO obtained from pure component breakthrough curves on CuTPA at 303 K

Total flow rate (mL/min)	Pressure (bar)	q_{CO2} (mmolCO₂/gCuTPA)	q_{CH4} (mmolCH₄/gCuTPA)	q_{CO} (mmolCO/gCuTPA)
	1	0.17	0.16	0.10
10	5	0.55	0.44	0.47
	10	1.12	0.93	1.09
	1	0.25	0.18	0.13
20	5	0.85	0.68	0.67
	10	1.49	1.33	1.30
	1	0.37	0.16	0.16
30	5	1.01	0.80	0.74
	10	1.61	1.50	1.47

Table 5.5. Molecular properties of studied gases
(Source: adapted from (Agueda et al. 2015))

Gas	Polarizability (Å³)	Dipole moment (Debye)	Quadrupole moment (Debye·Å)	Kinetic diameter (Å)
CO_2	2.51	0	4.28	3.3
CH_4	2.45	0	0	3.8
CO	1.95	0.11	2.84	3.6

The Langmuir and virial model parameters fitted to experimentally obtained CO_2, CH_4 and CO adsorption isotherms were obtained at a total feed flow of 30 mL/min, at 10 bar and stated in Table 5.6. As seen from the adsorption isotherms (Figure 5.3, Figure 5.6 and Figure 5.9) amount adsorbed did not reach a constant value and the saturation of CuTPA was not achieved, that is why formation monolayer coverage could not be ensured on CuTPA adsorbent.

The Langmuir constant, $\propto$ is directly related to binding energy or affinity of the adsorption system, while the Henry's constant calculated by virial model dictates the average interaction energy of single gas molecule with the adsorbent surface. As examined readily in detail, CO_2 was adsorbed more favorably by CuTPA due to its molecular properties (Table 5.5), therefore the highest affinity constant and Henry's constant was calculated for CO_2, followed by CH_4 and CO which in the same order of

adsorption capacity of CuTPA for these molecules. The higher correlation coefficients (R^2) and lower sum of squares of the errors (ERRSQ) with narrower margin of errors was found for virial isotherm model (Table 5.6).

Table 5.6. Langmuir and virial model parameters of pure CO_2, CH_4 and CO components on CuTPA at 303 K (Total feed flow: 30mL/min, bed pressure: 10 bar)

	Langmuir Model Parameters		
	CO_2	CH_4	CO
q_m (mmolg^{-1})	2.677 ± 0.041	11.48 ± 0.022	67.97 ± 0.082
∝ (bar^{-1})	0.137± 0.001	0.015 ± 0.001	0.002 ± 0.008
R^2	0.9996	0.9998	0.9998
ERRSQ	0.0122	0.0001	0.0012
	Virial Model Parameters		
	CO_2	CH_4	CO
H (mmolg^{-1}bar^{-1})	0.338 ± 0.013	0.175 ± 0.011	0.148 ± 0.013
b	0.467 ± 0.007	0.102 ± 0.004	0.002 ± 0.009
c	0	0	0.0035
R^2	0.9997	0.9999	0.9999
ERRSQ	0.0093	0.00007	0.0001

The CO_2/CH_4 binary adsorption studies was carried out three different total feed flows (10, 20 and 30 mL/min) and three different bed pressures (1, 5 and 10 bar) and the breakthrough curves for equimolar CO_2/CH_4 system on CuTPA at 303 K were given in Figure 5.10, 5.11 and 5.12. For CO_2/CH_4 binary system, CH_4 was the lighter component having relatively weak molecular interaction with the adsorbent while it was displaced by preferentially adsorbed component or namely, heavy component CO_2. Therefore, CH_4 breakthrough curve exhibited roll-up area, where the flow rate at the column exit exceeded the feed flow rate for some period of time. This phenomenon could be explained by the partial desorption of CH_4 due to the adsorption of CO_2, which causes CH_4 flow rate to rise above the feed flow rate. At constant CO_2/CH_4 feed flow the increase in bed pressure increases the roll-up of CH_4, also at constant bed pressure the rise in feed flow decreases the roll-up of CH_4.
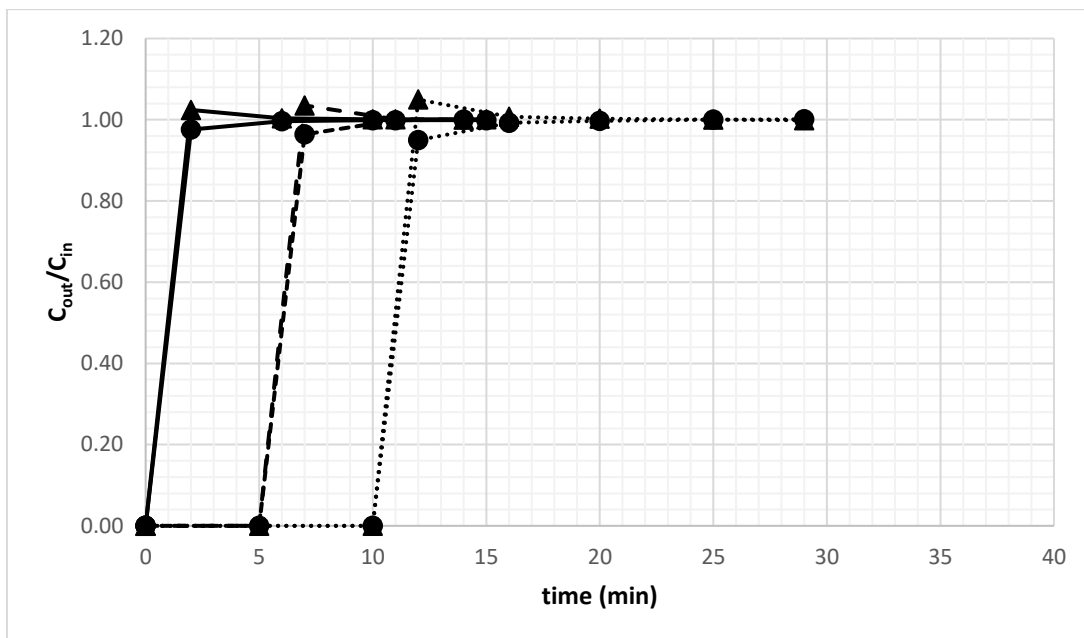
Figure 5.10. Effect of pressure on CO_2 and CH_4 adsorption breakthrough curves over CuTPA (Total CO_2/CH_4 flow rate: 30 mL/min; CO_2: ● and CH_4: ▲, Bed pressures: 1bar (———), 5bar (-----) and 10bar (···········))
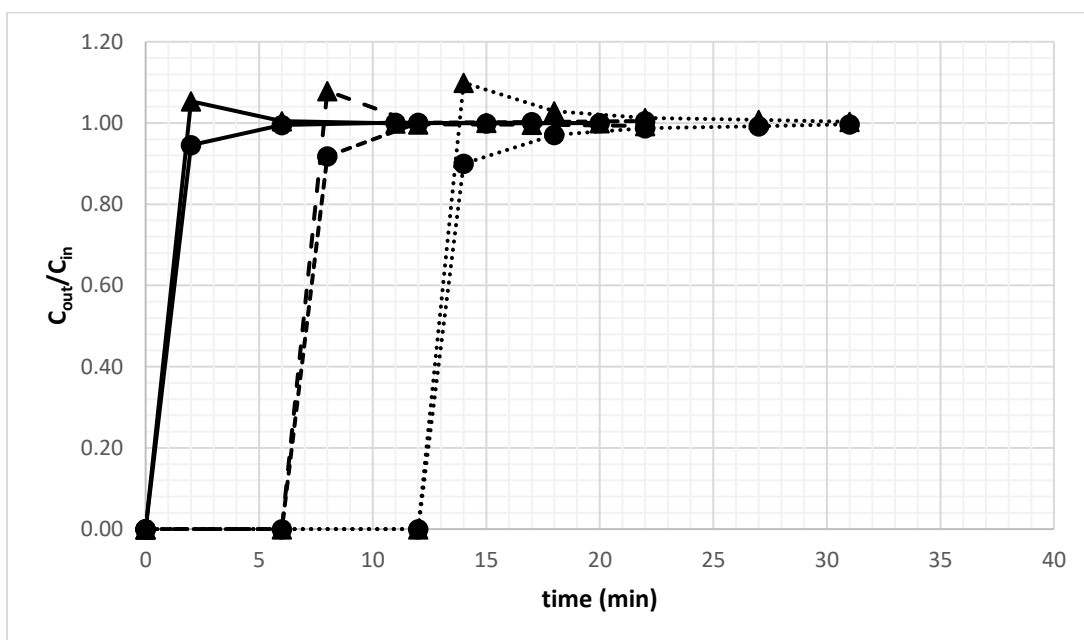
Figure 5.11. Effect of pressure on CO_2 and CH_4 adsorption breakthrough curves over CuTPA (Total CO_2/CH_4 flow rate: 20 mL/min; CO_2: ● and CH_4: ▲, Bed pressures: 1bar (———), 5bar (-----) and 10bar (···········))
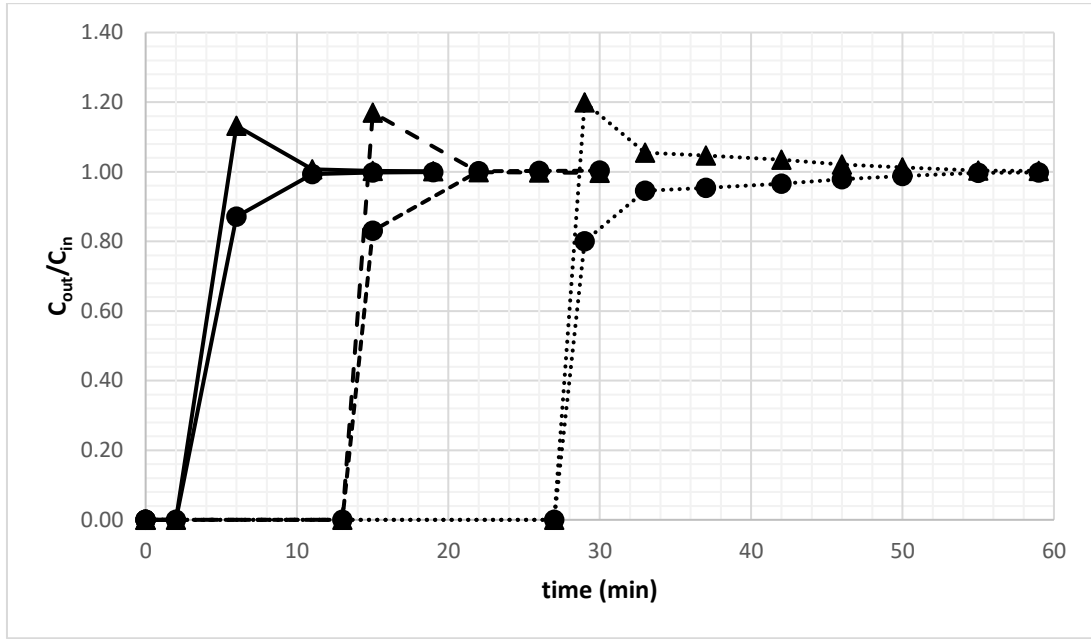
Figure 5.12. Effect of pressure on CO_2 and CH_4 adsorption breakthrough curves over CuTPA (Total CO_2/CH_4 flow rate: 10 mL/min; CO_2: ● and CH_4: ▲, Bed pressures: 1bar (———), 5bar (-----) and 10bar (·········))

The comparison of adsorbed CO_2 and CH_4 amounts between pure component systems (CO_2/H_2 and CH_4/H_2) and binary system (CO_2/CH_4) was given in Table 5.7. In CO_2/CH_4 binary system competitive adsorption was observed and both CO_2 and CH_4 components were adsorbed by CuTPA, while in pure systems carrier gas H_2 did not adsorbed by CuTPA as an indication of noncompetitive adsorption. The ideal and real selectivities of CuTPA for CO_2 over CH_4 was given in Appendix, Table A.1. In the pressure and feed rate range covered in the study, it was seen that the selectivity of CuTPA was around 1 implying that CuTPA was not a suitable adsorbent to separate equimolar CO_2/CH_4 binary mixture, but the highest selectivity of binary system was reached as 3.11 at 10 mL/min and 1 bar at 303 K.

Table 5.7. Adsorbed amounts of CO_2 and CH_4 in pure (CO_2/H_2 and CH_4/H_2) and binary (CO_2/CH_4) systems on CuTPA at 303 K

Total flow rate (mL/min)	Pressure (bar)	Adsorbed Amount in Pure System		Adsorbed Amount in Binary System	
		q_{CO_2} (mmolCO_2/g)	q_{CH_4} (mmolCH_4/g)	q_{CO_2} (mmolCO_2/g)	q_{CH_4} (mmolCH_4/g)
10	1	0.17	0.16	0.15	0.05
	5	0.55	0.44	0.52	0.23
	10	1.12	0.93	1.10	0.65
20	1	0.25	0.18	0.22	0.13
	5	0.85	0.68	0.68	0.62
	10	1.49	1.33	1.26	1.15
30	1	0.37	0.16	0.16	0.13
	5	1.01	0.80	0.87	0.77
	10	1.61	1.50	1.52	1.48

The influence of type of carrier gas used in the pure component adsorption studies was also examined on CuTPA. Despite the fact that the non-adsorptive behavior of H_2 carrier gas was previously asserted by the breakthrough curves of CO_2/H_2, CH_4/H_2 and CO/H_2 systems on CuTPA, gas systems that carried by inert helium flow were also checked. The breakthrough curves of equimolar CO_2/He, CH_4/He and CO/He systems were obtained at a constant total feed flow of 20 mL/min at bed pressures of 1, 3, 5, 8 and 10 bar. The mole percent of CO_2/He effluent over CuTPA were demonstrated in Figure 5.13 and those for CH_4/He and CO/He were given in Appendix, Figure A.14 and A.15, respectively. The mole percent graphs indicated the non-adsorptive behavior of He was ensured as for H_2.
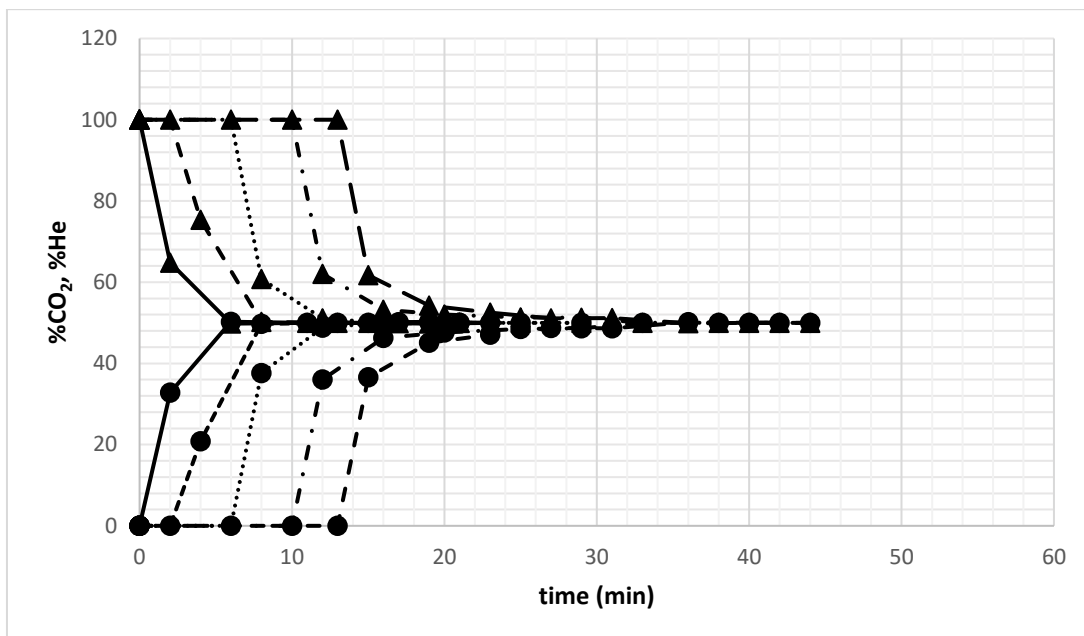
Figure 5.13. Molar percentages of CO_2 and He effluent over CuTPA at 303 K (Total CO_2/He flow rate: 20 mL/min; CO_2: ● and H_2:▲; Bed pressures: 1bar (——), 3bar (-----), 5bar (········), 8bar (— · —) and 10bar (— —))

The breakthrough curves obtained in case of He and H_2 carrier gases were given in Figure 5.14 for CO_2, in Figure 5.15 for CH_4 and in Figure 5.16 for CO gas systems. It was observed that the type of carrier gas slightly influenced the bed dynamics; the breakpoint of CO_2, CH_4 and CO and the time required to reach equilibrium were not changed, but the mean residence time of gases inside the bed (area above the curve until C_{out}/C_{in}: 1.0) was marginally changed with the type of carrier gas. Regardless of the type of carrier gas, the parameter that strongly influenced the breakthrough characteristics was the bed operating pressure.
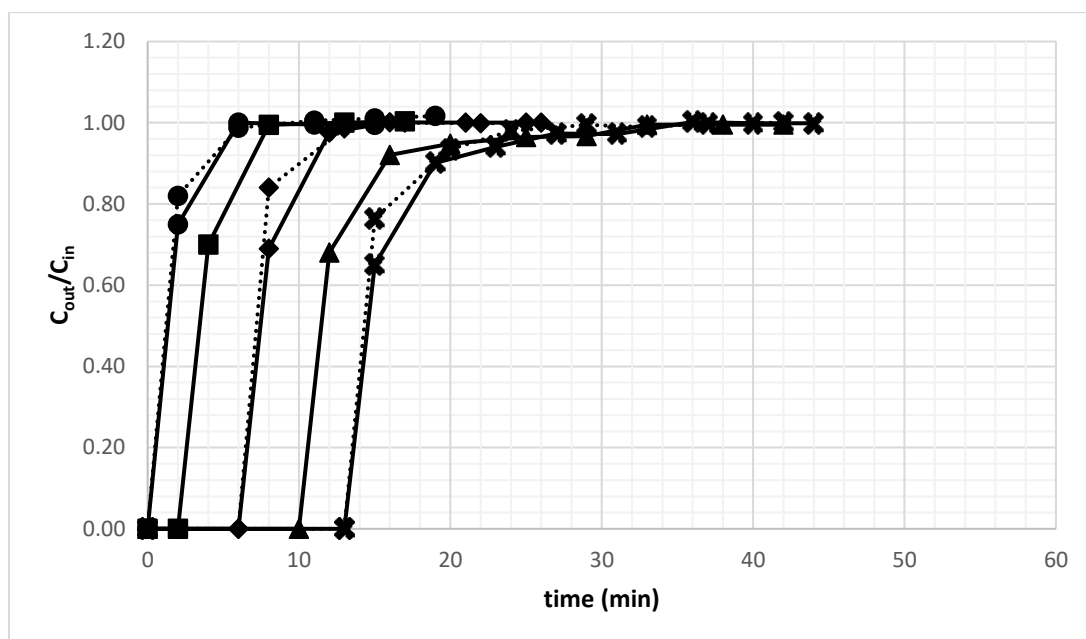
Figure 5.14. Effect of pressure on CO_2 adsorption breakthrough curves obtained for CO_2/He and CO_2/H_2 gas systems over CuTPA (Total feed flow rate: 20 mL/min; Bed pressures: 1bar (●), 3bar (■), 5bar (♦), 8bar (▲) and 10 bar (✖); CO_2/He system (———) and CO_2/H_2 system (·········))
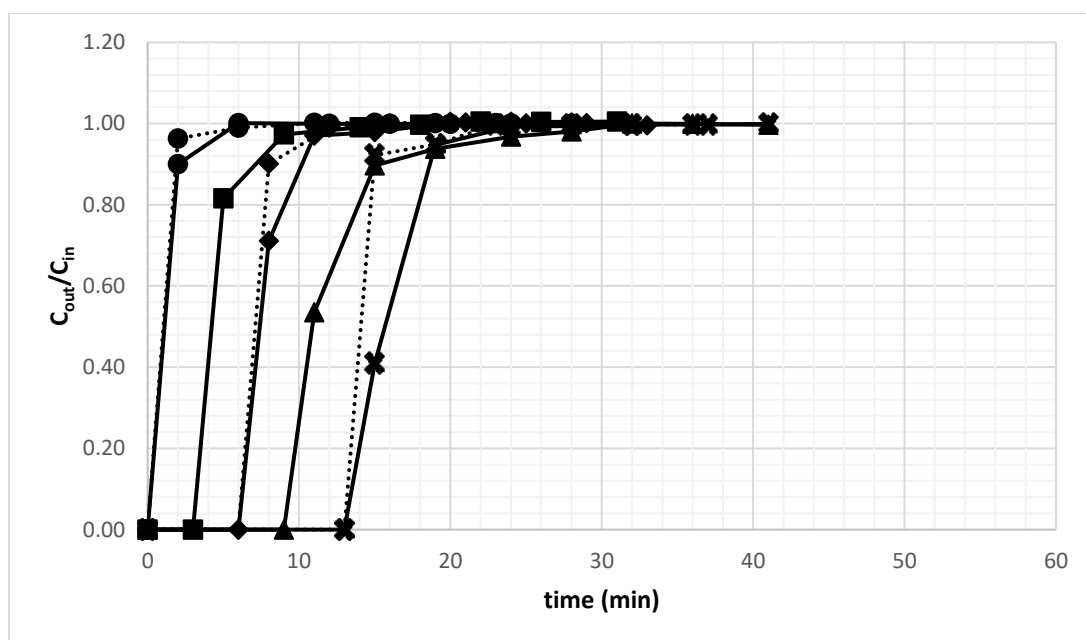
Figure 5.15. Effect of pressure on CH_4 adsorption breakthrough curves obtained for CH_4/He and CH_4/H_2 gas systems over CuTPA (Total feed flow rate: 20 mL/min; Bed pressures: 1bar (●), 3bar (■), 5bar (♦), 8bar (▲) and 10 bar (✖); CH_4/He system (———) and CH_4/H_2 system (·········))
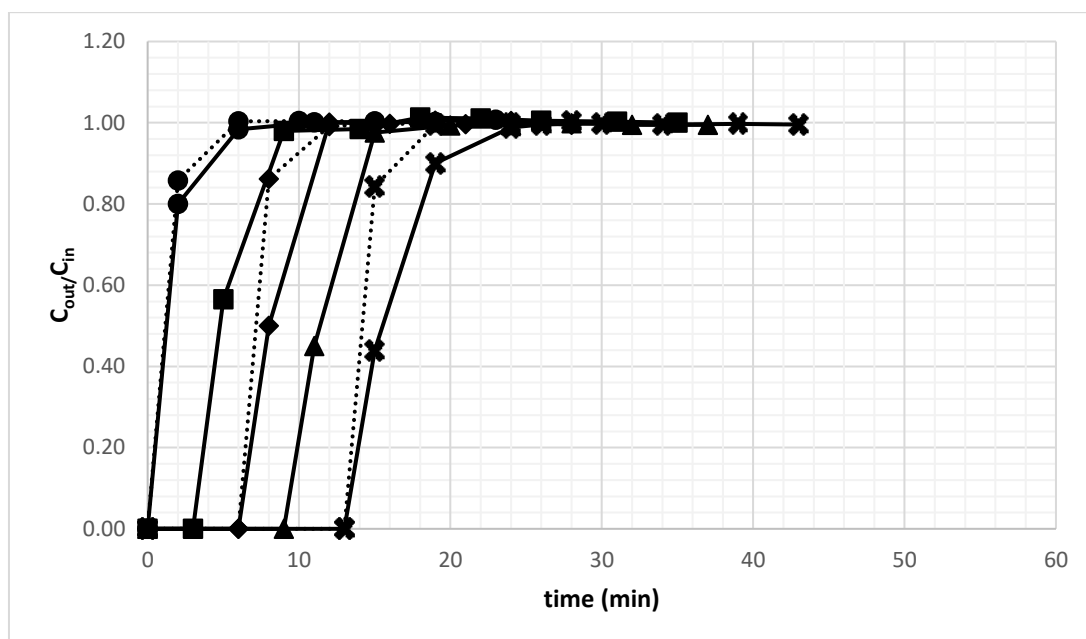
Figure 5.16. Effect of pressure on CO adsorption breakthrough curves obtained for CO/He and CO/H$_2$ gas systems over CuTPA (Total feed flow rate: 20 mL/min; Bed pressures: 1bar (●), 3bar (■), 5bar (♦), 8bar (▲) and 10 bar (✖); CO/He system (———) and CO/H$_2$ system (··········))

The influence of type of the carrier gas on the adsorbed gas amounts was given in Table 5.8. At each bed, operating pressure the adsorbed amount of CO$_2$, CH$_4$ and CO amounts were slightly higher when helium carrier was used. In contrast to inert gas He, hydrogen has molecular polarizability and quadrupole moment which could be involved molecular interaction between adsorbent surface resulted in reduction of adsorption capacity of CuTPA for CO$_2$, CH$_4$ and CO components.

Table 5.8. Comparison of adsorbed gas amounts in case of different type of carrier gas over CuTPA (Total feed flow: 20 mL/min)

Pressure (bar)	q$_{CO2}$ (mmol/CO$_2$/gCuPTA)		q$_{CH4}$ (mmol/CH$_4$/gCuPTA)		q$_{CO}$ (mmol/CO/gCuPTA)	
	CO$_2$/He	CO$_2$/H$_2$	CH$_4$/He	CH$_4$/H$_2$	CO/He	CO/H$_2$
1	0.20	0.25	0.15	0.18	0.14	0.13
3	0.50	-	0.45	-	0.40	-
5	0.80	0.85	0.71	0.68	0.70	0.67
8	1.20	-	1.12	-	1.10	-
10	1.44	1.49	1.34	1.33	1.34	1.30

5.2.2. Adsorption Studies on AlTPA

The change in molar percentage of CO_2, CH_4 and CO effluents with bed pressure at a constant feed flow of 30 mL/min of CO_2/H_2, CH_4/H_2 and CO/H_2 systems at 303 K were given in Figure 5.17, 5.18 and 5.19, respectively. Up to breakpoint of CO_2, CH_4 and CO, the molar percentages of compounds were read as zero, while H_2 was 100% indicating that H_2 was not adsorbed by AlTPA similar to the case for CuTPA.
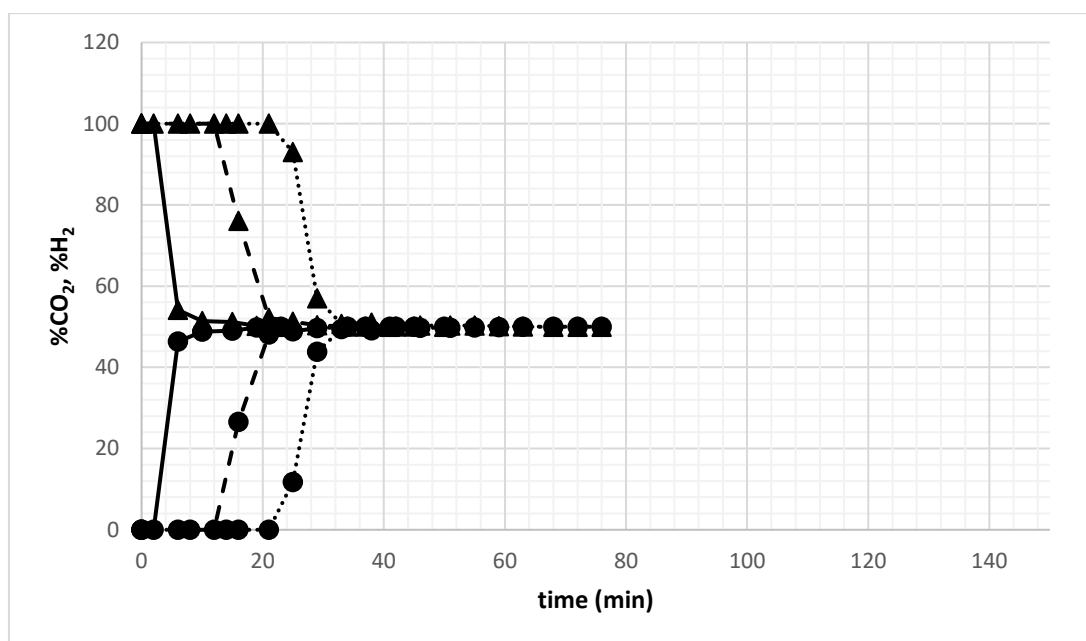
Figure 5.17. Molar percentages of CO_2 and H_2 effluent over AlTPA at 303 K (Total CO_2/H_2 flow rate: 30 mL/min; CO_2: ● and H_2:▲; Bed pressures: 1bar (———), 5bar (- - - - -), 10 bar (·········))
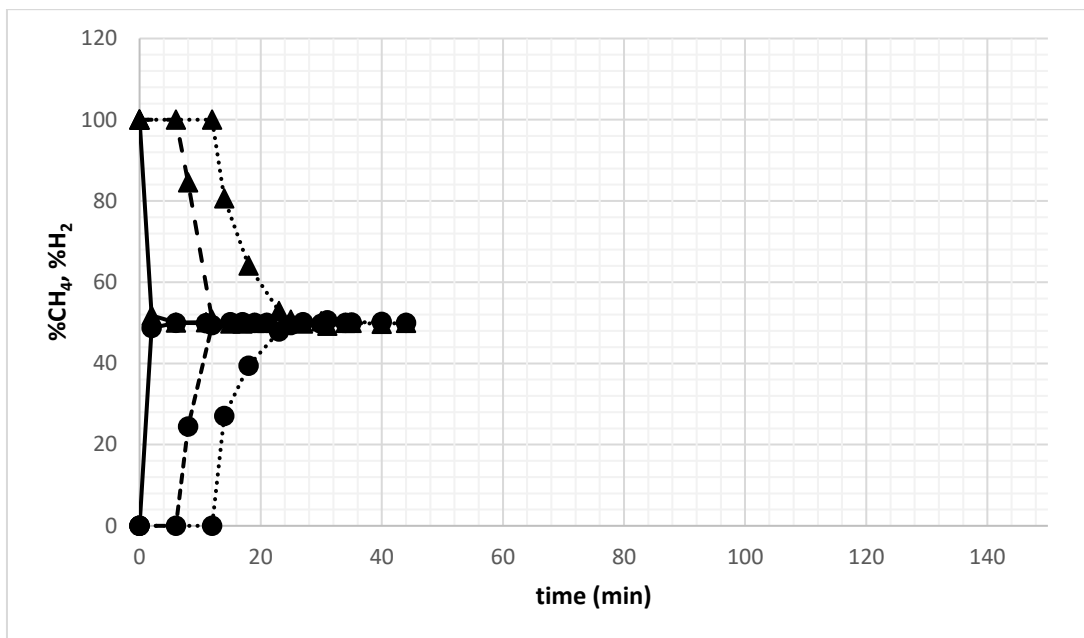
Figure 5.18. Molar percentages of CH$_4$ and H$_2$ effluent over AlTPA at 303 K (Total CH$_4$/H$_2$ flow rate: 30 mL/min; CH$_4$: ● and H$_2$:▲; Bed pressures: 1bar (———), 5bar (- - - -), 10 bar (··········))
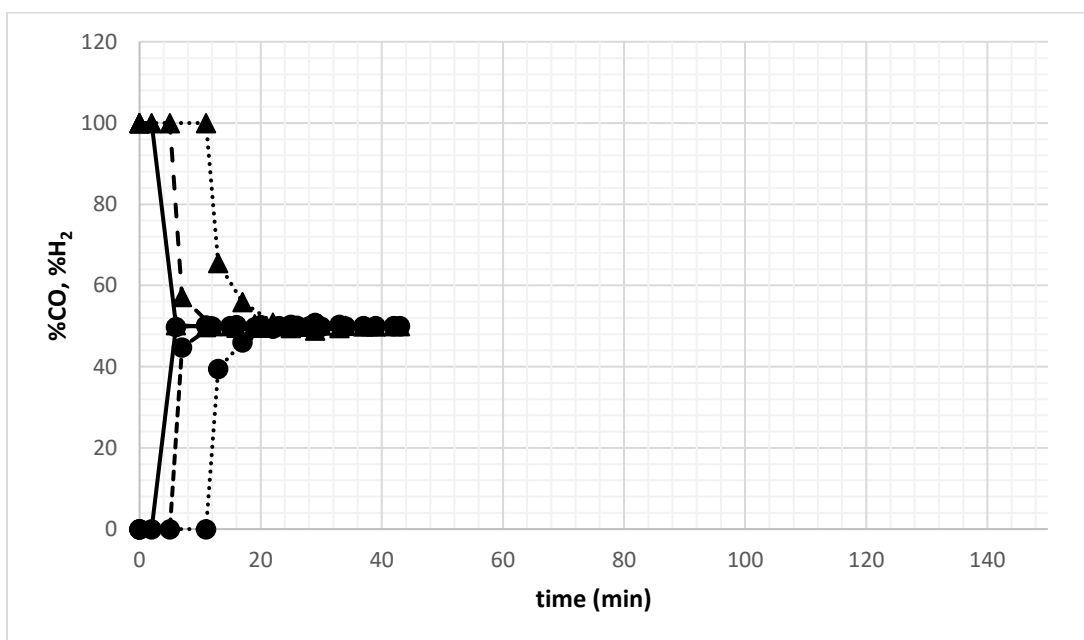
Figure 5.19. Molar percentages of CO and H$_2$ effluent over AlTPA at 303 K (Total CO/H$_2$ flow rate: 30 mL/min; CO: ● and H$_2$:▲; Bed pressures: 1bar (———), 5bar (- - - -), 10 bar (··········))

The dynamic behavior of AlTPA packed bed under CO_2/H_2, CH_4/H_2 and CO/H_2 flows was demonstrated in Figure 5.20, 5.21 and 5.22 respectively. At constant pressure, decrease in the feed flow elongates the breakpoint of adsorptive components as well as the saturation time of the AlTPA. The effect of pressure on the bed dynamics became dominant especially for low feed rates; the rise in pressure at a feed rate of 10 mL/min extremely prolonged the residence time of CO_2, CH_4 and CO inside the bed. The desorption curves of CO_2 (Figure 5.23) was obtained by feeding helium purge gas. At constant He flow, the time required for complete removal of CO_2 from AlTPA sharply rises with rise in bed pressure, especially at low He flow (10 mL/min). The same tendency in desorption curves was observed for CH_4 and CO components (Appendix, Figure A.16 and Figure A.17).
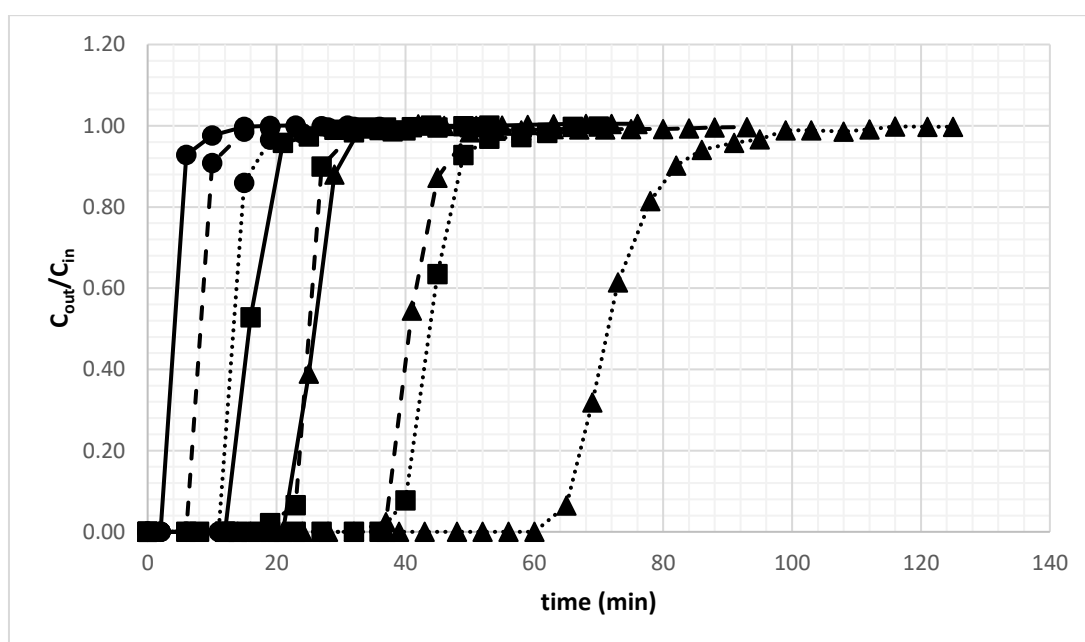
Figure 5.20. CO_2 adsorption breakthrough curves over AlTPA (Total CO_2/H_2 feed flow rate: 30 mL/min (——), 20 mL/min (– – – –) and 10 mL/min (⋯⋯); Bed pressures: 1bar (●), 5bar (■) and 10 bar (▲))
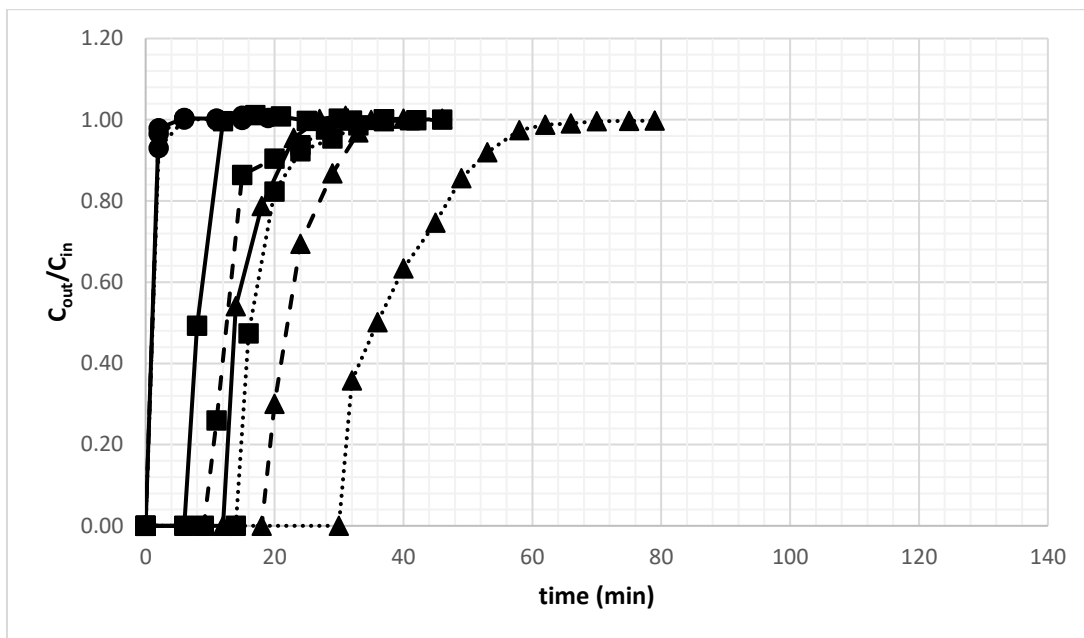
Figure 5.21. CH$_4$ adsorption breakthrough curves over AlTPA (Total CH$_4$/H$_2$ feed flow rate: 30 mL/min (———), 20 mL/min (- - - -) and 10 mL/min (·······); Bed pressures: 1bar (●), 5bar (■) and 10 bar (▲))
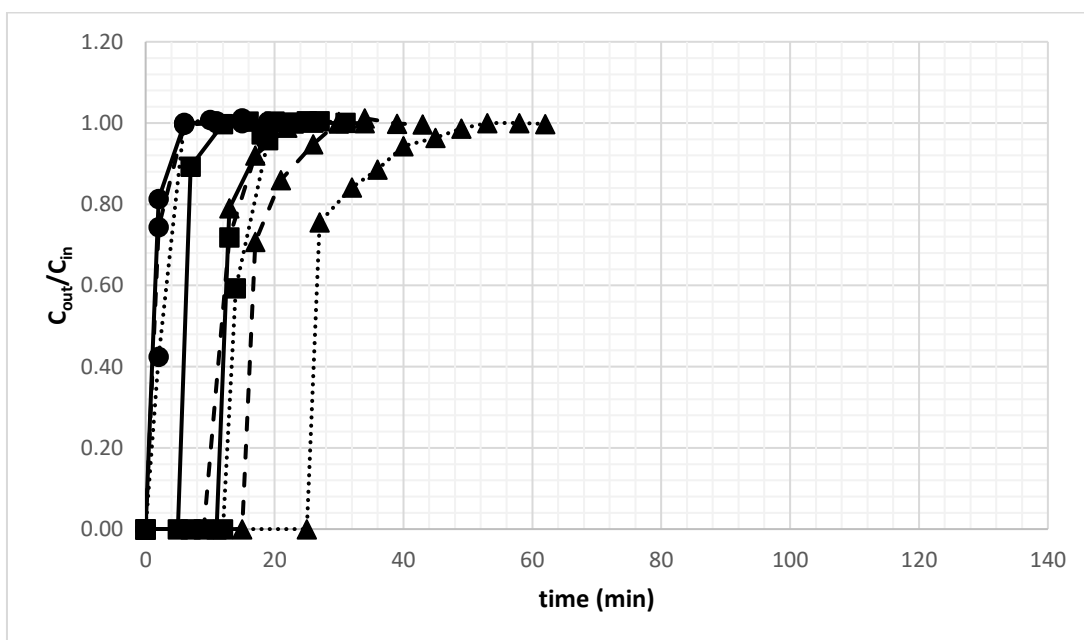
Figure 5.22. CO adsorption breakthrough curves over AlTPA (Total CO/H$_2$ feed flow rate: 30 mL/min (———), 20 mL/min (- - - -) and 10 mL/min (·······); Bed pressures: 1bar (●), 5bar (■) and 10 bar (▲))
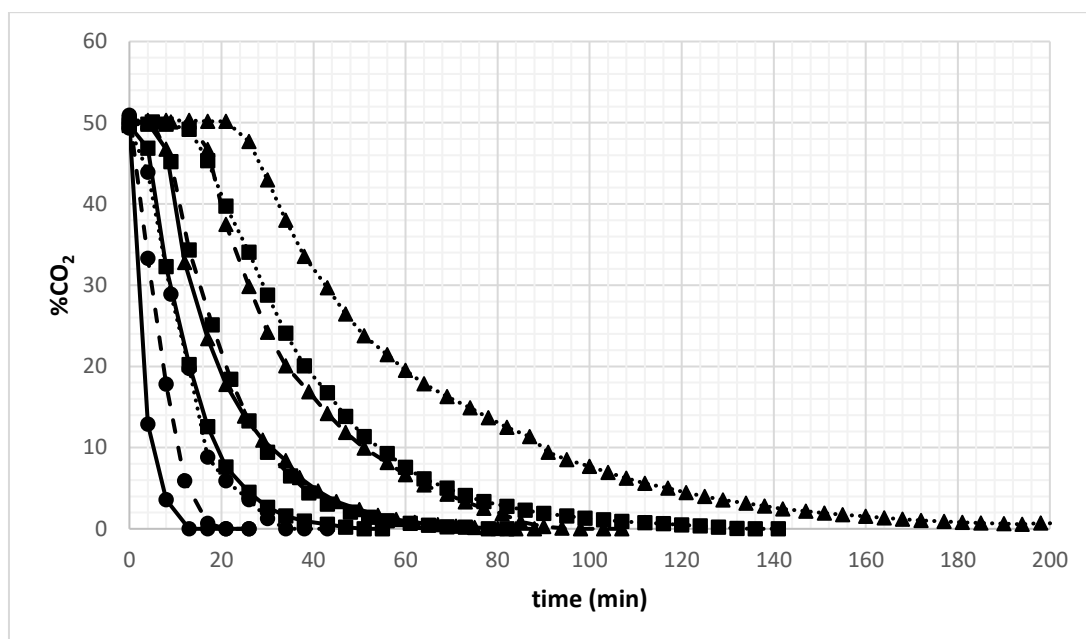
Figure 5.23. CO_2 desorption curves over AlTPA (He purge flow rate: 30 mL/min (——),
20 mL/min (–––––·) and 10 mL/min (··········); Bed pressures: 1bar (●), 5bar
(■) and 10 bar (▲))

The dynamic parameters for AlTPA packed bed were given in Appendix, in Table A.2 for CO_2/H_2, in Table A.3 for CH_4/H_2 and in Table A.4 for CO/H_2 system. The Langmuir and virial model parameters of pure CO_2, CH_4 and CO components on AlTPA were given in Table A.5. The graphs of fitted adsorption isotherm models to experimental CO_2, CH_4 and CO isotherms were illustrated in Appendix, Figure A.18, A.19 and A.20, respectively.

The adsorbed amount of SMR components on AlTPA was compared in Table 5.9. The same order of adsorption capacity determined for CuTPA was maintained for AlTPA; the highest adsorption capacity of AlTPA was for CO_2, followed by CH_4 and then CO. Therefore, as evaluated in detail for CuTPA, the adsorption mechanisms of CO_2, CH_4 and CO were greatly dictated by the molecular properties of adsorptive gases (Table 5.5) that enable the interaction between adsorptive and adsorbent surface. Moreover, the adsorbed gas amounts were increased with pressure and flow rate, and the highest adsorption capacity of AlTPA for CO_2 (5.54 mmolCO_2/gAlTPA), CH_4 (3.16 mmolCH_4/gAlTPA) and CO (2.59 mmolCO/gAlTPA) was reached at 30 mL/min and 10 bar. The Basolite A100 powder used by Heymans, Vaesen, and De Wiereld (2012) for acidic gas separation adsorbed 4.9 mmolCO_2/gAlTPA of CO_2 and 3.8 mmolCH_4/gAlTPA of CH_4 at 10 bar and 303 K. The adsorption capacity of commercial AlTPA (Basolite A100) pellets used by

Ferreira et al. (2015) for biogas upgrading was 2.3 mmolCO$_2$/gAlTPA for CO$_2$ and 0.5 mmol/gCH$_4$ for CH$_4$ at 1 bar and 303 K.

Table 5.9. Adsorbed amounts of CO$_2$, CH$_4$ and CO obtained from pure component breakthrough curves on AlTPA at 303 K

Total flow rate (mL/min)	Pressure (bar)	q$_{CO2}$ (mmolCO$_2$/gAlTPA)	q$_{CH4}$ (mmolCH$_4$/gAlTPA)	q$_{CO}$ (mmolCO/gAlTPA)
	1	0.80	0.22	0.14
10	5	2.56	1.15	0.75
	10	4.19	2.14	1.46
	1	1.14	0.41	0.22
20	5	3.36	1.62	1.13
	10	5.47	2.99	2.21
	1	1.19	0.45	0.31
30	5	3.41	1.73	1.26
	10	5.54	3.16	2.59

The CO$_2$/CH$_4$ binary breakthrough curves at different bed operating conditions on AlTPA were established in Appendix, Figure A.21, A.22 and A.23. Based on the calculated amount CO$_2$ and CH$_4$ adsorbed in pure and binary systems (Table 5.10), the selectivity of CO$_2$ over CH$_4$ was determined at each operating conditions and calculated selectivities were given in Appendix, Table A.6. The ideal selectivity was determined for noncompetitive adsorption for pure systems that carried by hydrogen (CO$_2$/H$_2$ and CH$_4$/H$_2$), while the real selectivity was calculated in case of competitive binary system (CO$_2$/CH$_4$). At constant feed rate, the rise in bed pressure decreased both ideal and real selectivity, while at constant bed pressure increase in feed rate resulted in rise of the selectivities (Figure 5.24). Moreover, the real selectivity was higher than ideal selectivity for all pressures and feed rates as a result of the competitive adsorption in CO$_2$/CH$_4$ system that reduces the amount of CH$_4$ more than CO$_2$ adsorbed. The highest ideal (3.6) and real (7.5) selectivities of AlTPA for CO$_2$ over CH$_4$ were found at a feed rate of 10 mL/min and 10 bar at 303 K. The noticeably high selectivities of AlTPA achieved in this study showed that AlTPA was a potential candidate for the selective separation of SMR components. The binary equimolar CO$_2$/CH$_4$ adsorption experiments conducted by Finsy et al. (2009) resulted in selectivity of 7.9 at 2.2 bar and 4.0 at 8 bar, while examined by Ferreira et al. (2015) gave real selectivity of 4 at 4 bar at 303 K.

Table 5.10. Adsorbed amounts of CO_2 and CH_4 in pure (CO_2/H_2 and CH_4/H_2) and binary (CO_2/CH_4) systems on AlTPA at 303 K

Total flow rate (mL/min)	Pressure (bar)	Adsorbed Amount in Pure System		Adsorbed Amount in Binary System	
		q_{CO2} (mmolCO$_2$/g)	q_{CH4} (mmolCH$_4$/g)	q_{CO2} (mmolCO$_2$/g)	q_{CH4} (mmolCH$_4$/g)
10	1	0.80	0.22	0.78	0.10
	5	2.56	1.15	2.53	0.49
	10	4.19	2.14	4.08	1.25
20	1	1.14	0.41	0.73	0.12
	5	3.36	1.62	3.27	0.92
	10	5.47	2.99	5.05	2.02
30	1	1.19	0.45	0.36	0.09
	5	3.41	1.73	3.13	1.17
	10	5.54	3.16	4.36	2.22
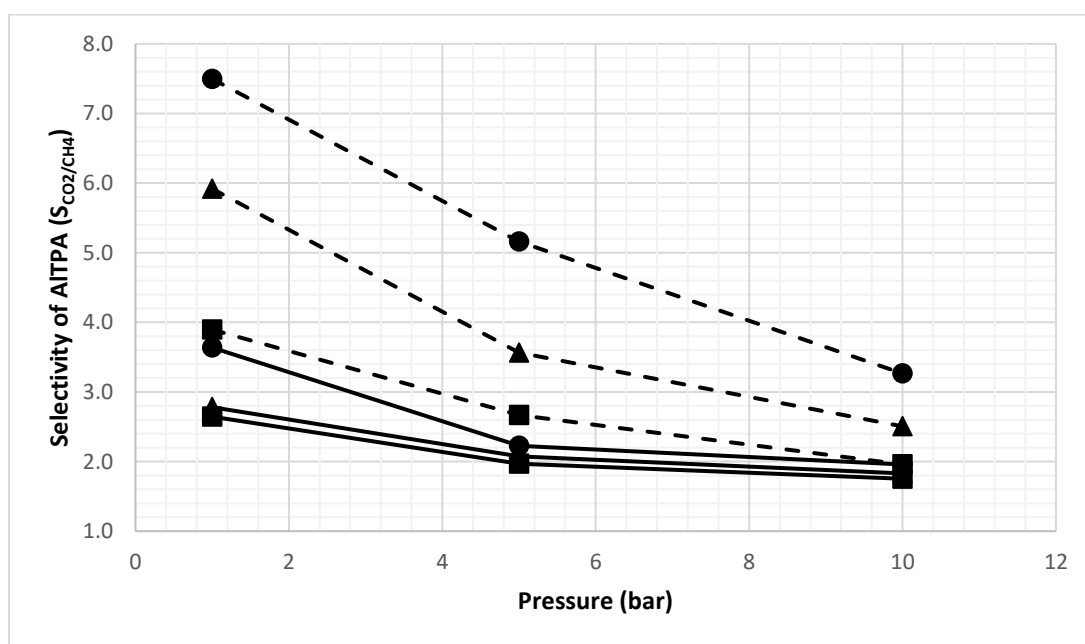
Figure 5.24. Effect of bed pressure and feed flow rate on ideal and real selectivities of AlTPA for CO_2 over CH_4 at 303 K (Ideal selectivity (———), Real selectivity (------); Total feed flow rate: 10 mL/min (●), 20 mL/min (▲) and 30 mL/min (■))

5.2.3. Adsorption Studies on TiTPA

The molar percentages of CO_2/H_2, CH_4/H_2 and CO/H_2 systems over ZnTPA were demonstrated in Appendix, Figure A.24, A.25 and A.26, respectively. It was confirmed that TiTPA adsorbed only SMR components, not H_2 at 303 K, hence the noncompetitive pure component adsorption on TiTPA was subjected, as in CuTPA and AlTPA. The

experimental breakthrough curves of CO_2, CH_4 and CO obtained from TiTPA packed bed were established in Figure 5.25, 5.26 and 5.27, respectively. The breakthrough curves of CO_2 were widespread and the dynamic parameters of breakpoint time, saturation time, consequently the mean residence time were longer than curves for CH_4 and CO as an indication of preferable adsorption of CO_2. Breakthrough profiles for CH_4 and CO at each flow rate were orderly parallel to each other suggesting that similar adsorption dynamics were followed and the effect of feed rate on the adsorption mechanism could be neglected and except for the low feed rate (10 mL/min) where the external mass transfer resistance was intensely experienced. The desorption curves were given in Appendix, Figure A.27, A.28 and A.29 for CO_2, CH_4 and CO, respectively. The time based dynamic parameters of TiTPA packed bed obtained by experimental breakthrough curves of CO_2/H_2, CH_4/H_2 and CO/H_2 systems were in Appendix, Table A.7, A.8 and A.9, respectively.
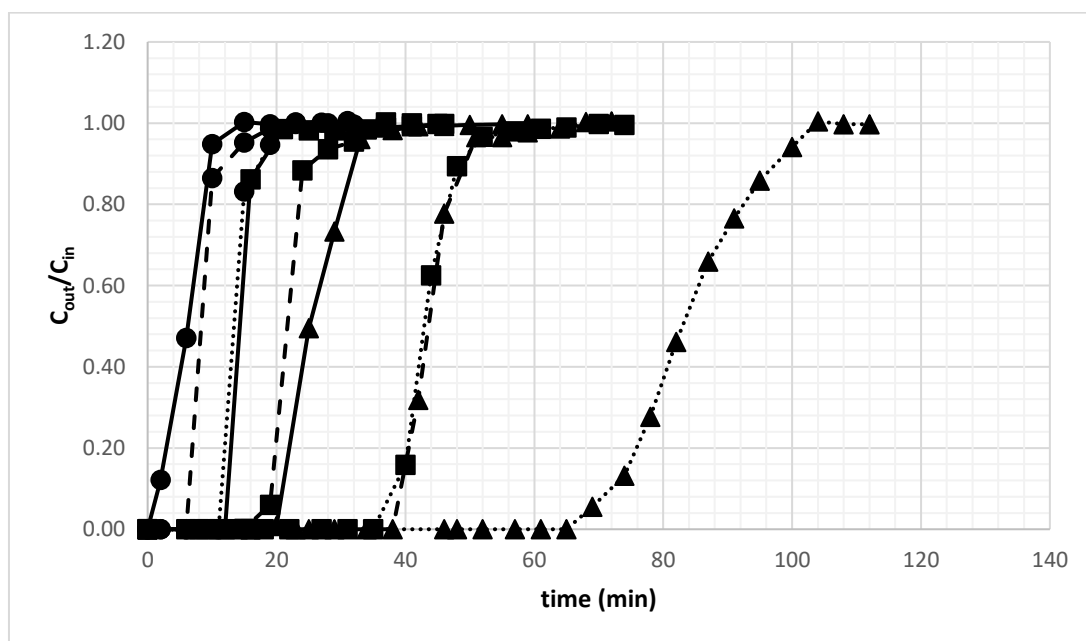
Figure 5.25. CO_2 adsorption breakthrough curves over TiTPA (Total CO_2/H_2 feed flow rate: 30 mL/min (———), 20 mL/min (‐ ‐ ‐ ‐) and 10 mL/min (⋯⋯⋯); Bed pressures: 1bar (●), 5bar (■) and 10 bar (▲))
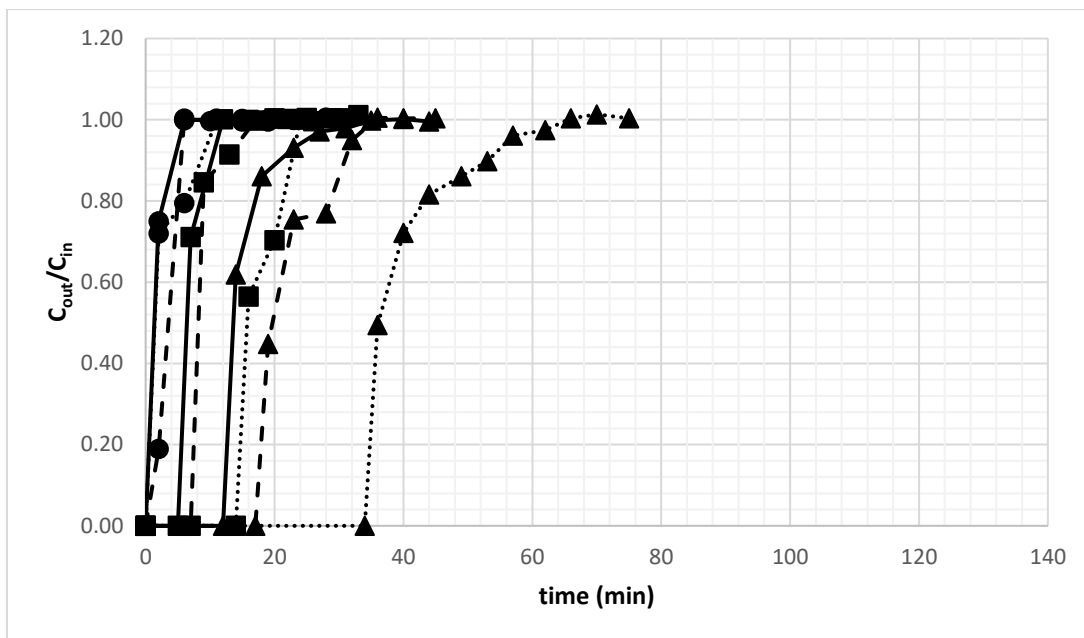
Figure 5.26. CH₄ adsorption breakthrough curves over TiTPA (Total CH4/H2 feed flow rate: 30 mL/min (——), 20 mL/min (-----) and 10 mL/min (·········); Bed pressures: 1bar (●), 5bar (■) and 10 bar (▲))
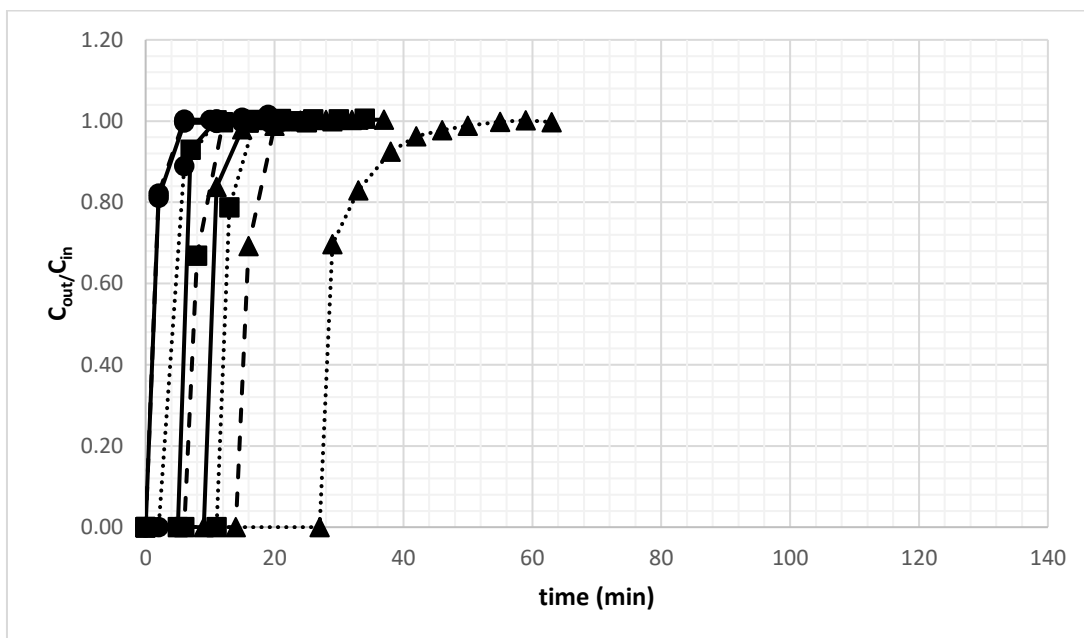
Figure 5.27. CO adsorption breakthrough curves over TiTPA (Total CO/H2 feed flow rate: 30 mL/min (——), 20 mL/min (-----) and 10 mL/min (·········); Bed pressures: 1bar (●), 5bar (■) and 10 bar (▲))

The adsorbed amount of SMR components on TiTPA was stated in Table 5.11. As breakthrough curves revealed that, CO_2 was most favorably adsorbed, followed by CH_4 and CO as a result of molecular properties of components as examined previously

(Table 5.5). The highest adsorption capacities of TiTPA were 5.20 mmolCO_2/gTiTPA for CO_2, 3.25 mmolCH_4/gTiTPA for CH_4 and 1.91 mmolCO/gTiTPA for CO at 30 mL/min, 10 bar at 303 K. For comparison, the TiTPA synthesized by Rada et al. (2015) adsorbed 2.1 mmolCO_2/gTiTPA of CO_2 at 5 bar and 2.9 mmolCO_2/gTiTPA at 10 bar, and the adsorbed CH_4 amounts were 0.5 mmolCH_4/gTiTPA at 5 bar and 1.3 mmolCH_4/gTiTPA at 10 bar 298 K. TiTPA studied by Wiersum et al. (2013) adsorbed 9 mmolCO_2/gTiTPA of CO_2 at 10 bar and 10.1 mmolCO_2/gTiTPA at 50 bar and 4.2 mmolCH_4/TiTPA of CH_4 at 10 bar and 7.1 mmolCH_4/gTiTPA at 50 bar 303 K. The Langmuir and virial model parameters of SMR components over TiTPA were given in Appendix, Table A.10 and the model isotherms fitted to experimental data (Appendix, Figure A.30, A.31 and A.32) revealed that TiTPA was not saturated yet by SMR components in the pressure and flow rate range operated in this study.

Table 5.11. Adsorbed amounts of CO_2, CH_4 and CO obtained from pure component breakthrough curves on TiTPA at 303 K

Total flow rate (mL/min)	Pressure (bar)	q_{CO2} (mmolCO_2/gTiTPA)	q_{CH4} (mmolCH_4/gTiTPA)	q_{CO} (mmolCO/gTiTPA)
	1	0.80	0.26	0.17
10	5	2.47	0.89	0.56
	10	4.71	2.08	1.40
	1	1.18	0.51	0.49
20	5	2.88	1.04	0.90
	10	5.17	2.7	1.80
	1	1.25	0.82	0.80
30	5	3.01	1.34	1.15
	10	5.20	3.25	1.91

The effect of bed pressure (Figure A.33, A.34 and A.35) and the feed rate (Figure A.36, A.37 and A.38) on CO_2/CH_4 binary breakthrough curves on TiTPA at 303 K were given in Appendix. According to CO_2 and CH_4 adsorbed amounts (Table 5.12), the ideal and real selectivities (Appendix, Table A.11) were calculated for pure and binary systems, respectively. In this study, the highest ideal selectivity for CO_2 over CH_4 (3.1) and the real selectivity (8.0) was achieved at 10 mL/min of feed rate and 10 bar at 303 K. The ideal selectivities reached by Abid et al. (2016) was 6.0 at 1 bar and 4.2 at 5 bar at 298 K, while the ideal selectivity found by Wiersum et al. (2013) was 2.1 at 10 bar and 1.42 at

50 bar and the highest real selectivity was 4.3 at 4 bar at 303 K. The ideal selectivity of TiTPA was slightly changed with pressure, whereas the real selectivity was greatly influenced with the rise in bed pressure and feed rate (Figure 5.28).

Table 5.12. Adsorbed amounts of CO_2 and CH_4 in pure (CO_2/H_2 and CH_4/H_2) and binary (CO_2/CH_4) systems on TiTPA at 303 K.

Total flow rate (mL/min)	Pressure (bar)	Adsorbed Amount in Pure System		Adsorbed Amount in Binary System	
		q_{CO2} (mmolCO_2)	q_{CH4} (mmolCH_4/g)	q_{CO2} (mmolCO_2/g)	q_{CH4} (mmolCH_4/g)
10	1	0.80	0.26	0.73	0.09
	5	2.47	0.89	2.42	0.44
	10	4.71	2.08	4.67	1.25
20	1	1.18	0.51	1.03	0.15
	5	2.88	1.51	2.83	0.73
	10	5.17	2.9	4.90	1.90
30	1	1.25	0.62	1.06	0.20
	5	3.01	1.78	2.94	1.05
	10	5.20	3.25	4.36	2.12
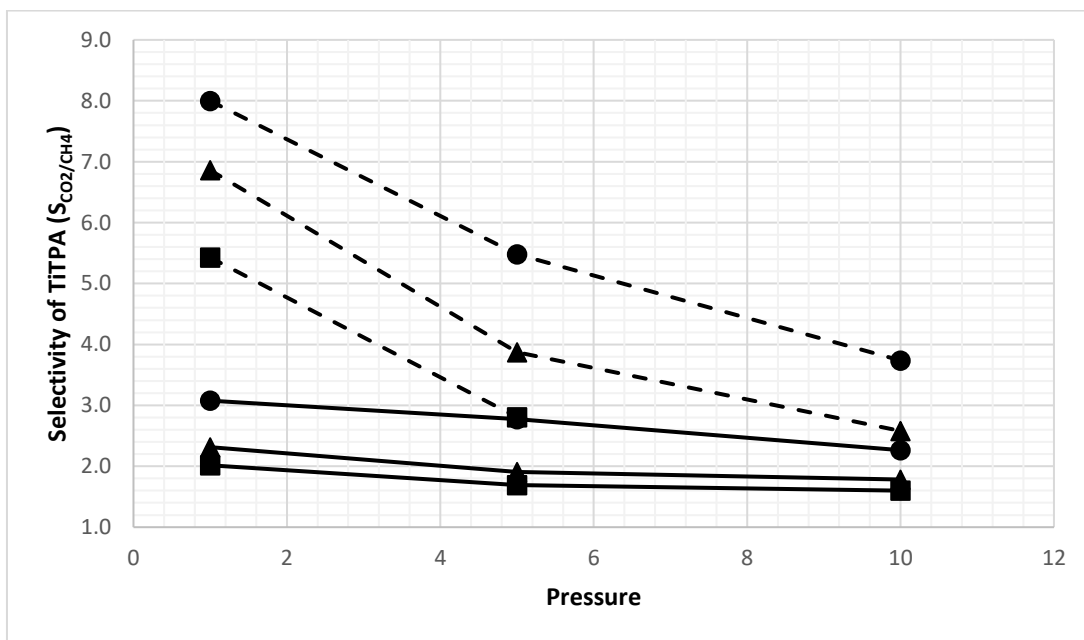
Figure 5.28. Effect of bed pressure and feed flow rate on ideal and real selectivities of TiTPA for CO_2 over CH_4 at 303 K (Ideal selectivity (———), Real selectivity (-----); Total feed flow rate: 10 mL/min (●), 20 mL/min (▲) and 30 mL/min (■))

5.2.4. Adsorption Studies on ZnTPA

The non-adsorbed behavior of carrier gas H_2 in CO_2/H_2, CH_4/H_2 and CO/H_2 systems on ZnTPA were checked by the effluent molar percentages of CO_2, CH_4 and CO in presented at Appendix, Figure A.39, A.40 and A.41. The experimental breakthrough curves of SMR components over ZnTPA at different bed operating conditions were stated in Figure 5.29, 5.30 and 5.31 for CO_2, CH_4 and CO, respectively. At atmospheric pressure the SMR components left the bed immediately and the curves belongs to high flow rates (30 mL/min and 20 mL/min) were overlapped. The impact of external mass transfer resistance were negligible at higher flow rates (30 mL/min) as the curves were strictly parallel to each other at each bed pressure. The distance between breakthrough curves extended at lower flow rates, especially at 10 mL/min feed rate and 10 bar, the effect of external mass transfer intensively experienced. The desorption curves of SMR components were given in Appendix, Figure A.42 and A.43. The dynamic parameters evaluated over ZnTPA bed were demonstrated in Table A.12, A.13 and A.14 for CO_2, CH_4 and CO, respectively. Since the increase in bed pressure at constant feed rate, prolonged the time spent (τ) of SMR components inside the bed and the bed was used more efficiently, so the H_{UNB} decreased. On the other hand, at constant bed pressure, rise in feed rate caused to decrease in τ, consequently increase in H_{UNB}.
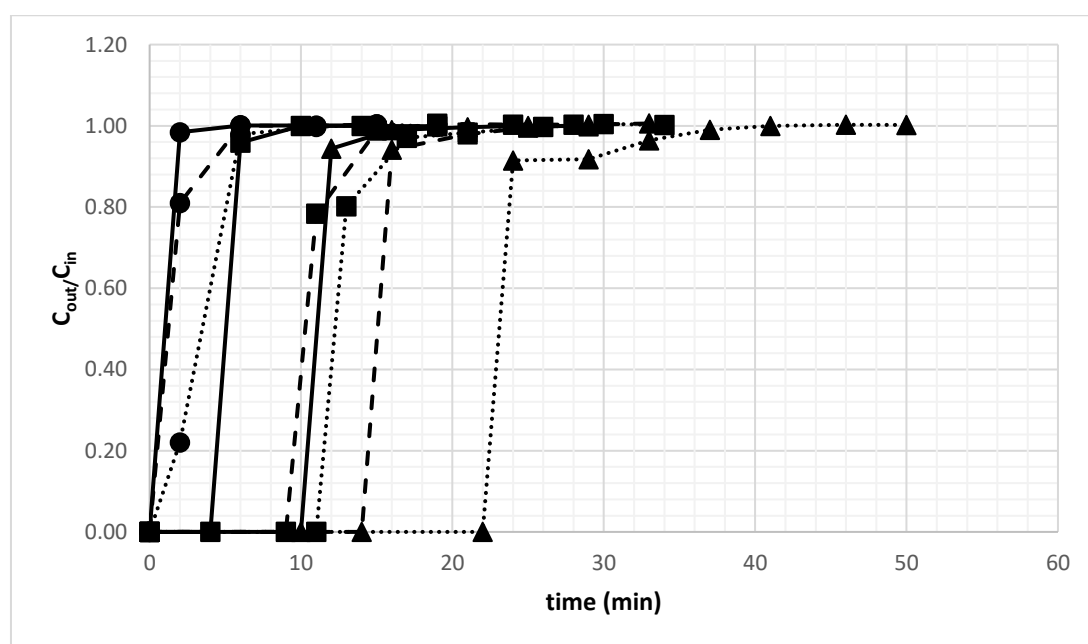
Figure 5.29. CO_2 adsorption breakthrough curves over ZnTPA (Total CO_2/H_2 feed flow rate: 30 mL/min (——), 20 mL/min (- - - -) and 10 mL/min (·········); Bed pressures: 1bar (●), 5bar (■) and 10 bar (▲))
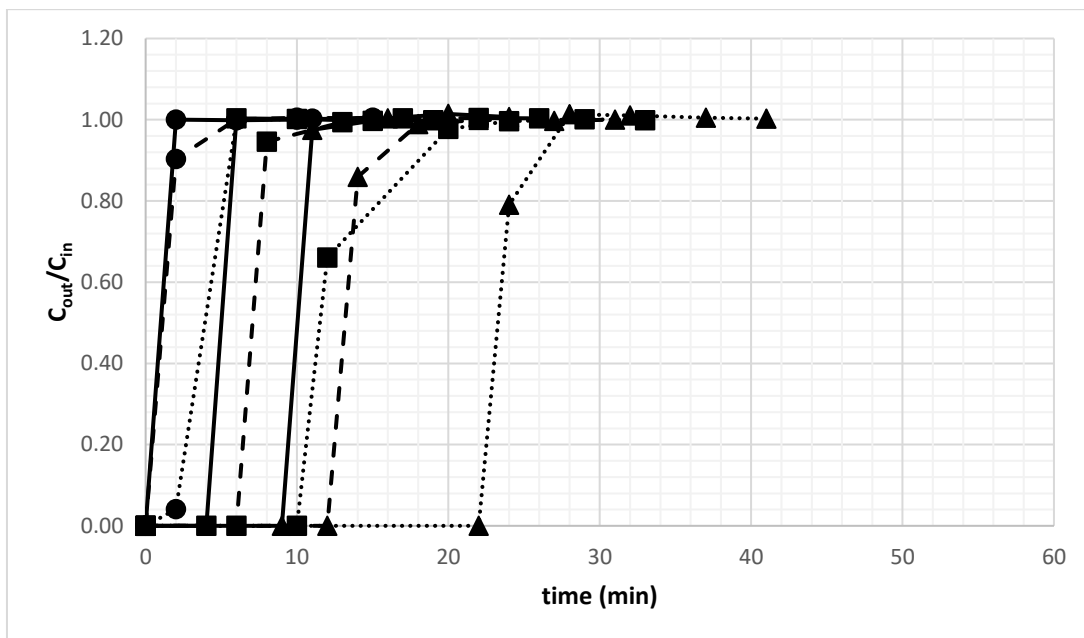
Figure 5.30. CH₄ adsorption breakthrough curves over ZnTPA (Total CH_4/H_2 feed flow rate: 30 mL/min (⎯⎯), 20 mL/min (-----) and 10 mL/min (·········); Bed pressures: 1bar (●), 5bar (■) and 10 bar (▲))
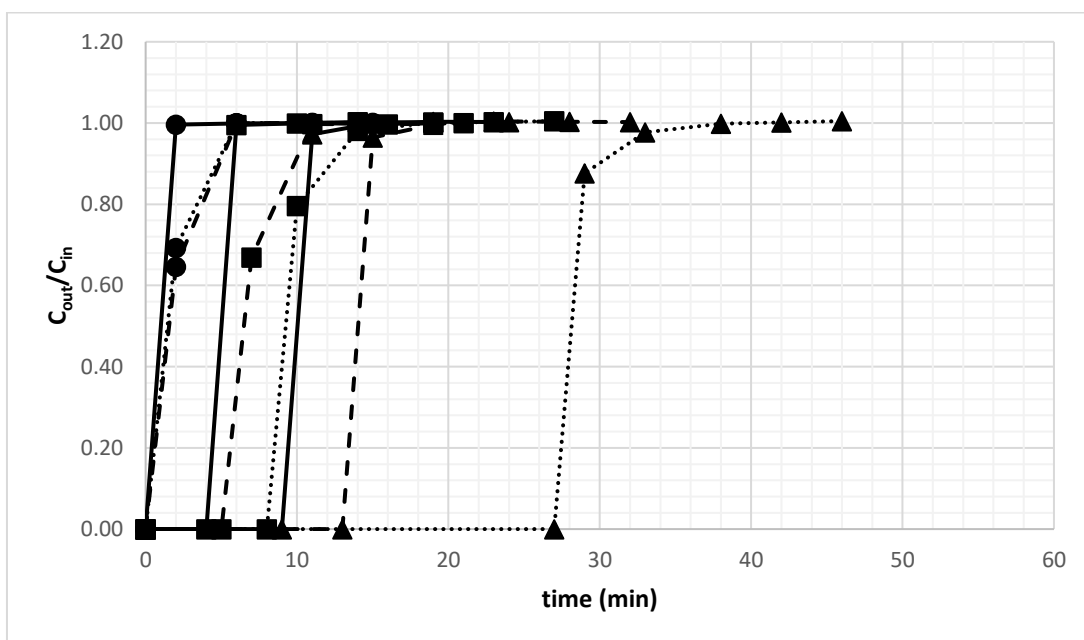
Figure 5.31. CO adsorption breakthrough curves over ZnTPA (Total CO/H_2 feed flow rate: 30 mL/min (⎯⎯), 20 mL/min (-----) and 10 mL/min (·········); Bed pressures: 1bar (●), 5bar (■) and 10 bar (▲))

The adsorbed amounts of SMR components on ZnTPA at 303 K were listed in Table 5.13. The adsorption capacity of ZnTPA was higher for CO_2 among SMR components due to higher polarizability and quadrupole moment of CO_2 that enables the stronger interaction with ZnTPA surface. The highest adsorbed amounts over ZnTPA

76

were calculated as 2.11 mmolCO$_2$/gZnTPA for CO$_2$, 1.90 mmolCH$_4$/gZnTPA for CH$_4$ and 1.83 mmolCO/gZnTPA for CO at 30 mL/min and 10 bar. The commercial ZnTPA investigated by Karra and Walton (2010) adsorbed 3.8 mmolCO$_2$/gZnTPA of CO$_2$ and 2.1 mmolCO/gZnTPA of CO at 1 bar 298 K, while the ZnTPA synthesized by Mishra et al. (2012) adsorbed 1.1 mmolCO$_2$/gZnTPA of CO$_2$ at 10 bar and 2.6 mmolCO$_2$/gZnTPA at 50 bar and the adsorbed CH$_4$ amount was 0.24 mmolCH$_4$/gZnTPA at 10 bar and 0.7 mmolCH$_4$/gZnTPA at 50 bar 303 K.

The calculated ideal selectivities of ZnTPA for CO$_2$ over CH$_4$ (Appendix, Table A.15) at different bed pressures and feed rates were close to 1 presenting that the ZnTPA was not effective for selective separation of CO$_2$/CH$_4$ mixture. Therefore, the binary adsorption studies were not conducted on ZnTPA adsorbent.

Table 5.13. Adsorbed amounts of CO$_2$, CH$_4$ and CO obtained from pure component breakthrough curves on ZnTPA at 303 K

Total flow rate (mL/min)	Pressure (bar)	q$_{CO2}$ (mmolCO$_2$/gZnTPA)	q$_{CH4}$ (mmolCH$_4$/gZnTPA)	q$_{CO}$ (mmolCO/gZnTPA)
	1	0.18	0.16	0.08
10	5	0.64	0.59	0.42
	10	0.90	0.88	0.73
	1	0.19	0.17	0.13
20	5	1.34	0.85	0.79
	10	1.81	1.56	1.46
	1	0.20	0.19	0.18
30	5	1.84	1.82	1.77
	10	2.11	1.90	1.83

The calculated Langmuir and virial model parameters of SMR components on ZnTPA was stated in Appendix, Table A.16. The fitted model isotherms to experimental isotherm data (Appendix, Figure A.44, A.45 and A.46) revealed that with the rise in bed pressure the adsorbed CO$_2$, CH$_4$ and CO amount sharply increased for total feed rates of 10 and 20 mL/min. However, with the increase in feed rate to 30 mL/min a plateau was formed in adsorbed amounts at high pressures, as an indication of saturation of ZnTPA with SMR components at high feed rates and bed pressures.

Among the four MOFs packed in the adsorption bed, TiTPA has the highest surface area, whereas AlTPA has the highest micropore volume and average pore

diameter (Table 4.2). The higher surface area and micropore volume of adsorbent the higher adsorbed amount and the higher average pore diameter easier penetration of gas molecules into the micropores were expected. Considering the Table 5.4, Table 5.9, Table 5.11 and table 5.13 in the covered feed rate and bed pressure range especially at 30 mL/min and 10 bar where the highest amount of adsorbed values achieved on all four MOFs were compared. Even though TiTPA with the highest surface area was expected to be adsorbed more amount of SMR components, but AlTPA adsorbed higher amount of CO_2 and CO components than TiTPA. Also, CH_4 with the highest kinematic diameter was expected to penetrate more easily to AlTPA having highest average pore diameter, but CH_4 was adsorbed more by TiTPA. The higher adsorption affinity, consequently the higher adsorbed amounts on AlTPA towards the adsorbates having quadrupole moment (CO_2 and CO) and could be caused by the strong interactions between these molecules and hydroxyl groups of AlTPA. On the other hand, ZnTPA and CuTPA have relatively comparable surface areas but lower than both TiTPA and AlTPA resulted in lower adsorption capacities of SMR components than both TiTPA and AlTPA. But the higher surface area, micropore volume and average pore diameter of ZnTPA than CuTPA provided relatively higher adsorption capacities for SMR components.

Considering Table A.1, Table A.6, Table A.11 and Table A.15, at 10 mL/min feed rate and 1 bar, the highest ideal and real selectivities for CO_2 over CH_4 were attained and over AlTPA (3.6, 7.5) and TiTPA (3.1, 8.0). In addition, it was noteworthy that the selectivity values for AlTPA and TiTPA were superior to those values of many reported MOFs under the same conditions. Therefore, the results demonstrated that AlTPA and TiTPA can be served as an excellent candidate for the selective sorption of CO_2 from SMR off-gas streams. However, at 10 mL/min and 1 bar the amount adsorbed of SMR components was very low on MOFs, thereby the compromise between adsorption capacity and selectivity should be made based on the purpose of the process (e.g., gas storage or selective gas separation). The selectivity of CuTPA and ZnTPA for CO_2 over CH_4 were found close to 1 at each feed rate and bed pressure, but the adsorption capacities for SMR components was higher than many stated MOFs in literature, thereby application of CuTPA and ZnTPA could be more suitable in gas storage rather than selective gas separation.

CHAPTER 6

CONCLUSION

Within the scope of the TUBITAK (112M294) project successfully concluded in IYTE and EGE University, CuTPA (S_{Lang}: 776 $m^2 g^{-1}$), AlTPA (S_{Lang}: 1330 $m^2 g^{-1}$), TiTPA (S_{Lang}: 1834 $m^2 g^{-1}$) and ZnTPA (S_{Lang}: 1023 $m^2 g^{-1}$) MOFs were synthesized and packed into the fixed bed for further adsorption studies on SMR components. The conducted adsorption studies were involved the investigation of dynamic behavior of CuTPA, AlTPA, TiTPA and ZnTPA packed beds via experimental breakthrough curves of CO_2, CH_4 and CO, followed by the calculation of the adsorbed SMR component amounts and determination of selectivity of CO_2 over CH_4 over each aforementioned MOF.

The pure component (noncompetitive) adsorption studies of CO_2/H_2, CH_4/H_2 and CO/H_2 gas systems and binary (competitive) adsorption studies on CO_2/ CH_4 system were carried out at 10mL/min, 20 mL/min and 30 mL/min total feed flow at 1, 5 and 10 bar bed pressures at 303 K. The dynamic behavior analysis showed the bed operating pressure drastically effected the breakthrough curves of SMR components, at constant feed flow increase in pressure directly prolonged the t_{break}, t_{sat}, t_{des} and τ_{CO2}, resulted in much longer cycle times. At high feed flow rates, even though the external mass transfer resistance was overcome at atmospheric pressure, but rising the bed pressure up to 10 bar the breakthrough characteristics greatly experienced the mass transfer resistance.

The great potential of CuTPA, AlTPA, TiTPA and ZnTPA for hydrogen purification from SMR off-gas streams was confirmed by the experimental breakthrough analysis showing that hydrogen was not adsorbed on these aforementioned adsorbents under covered operating conditions in this study. The highest adsorbed CO_2, CH_4 and CO amounts were attained at 30mL/min of feed rate and 10 bar on each MOF. All MOFs adsorbed CO_2 in higher amounts than CH_4 and CO due to higher quadrupole moment and polarizability of CO_2 that enable the stronger interactions between CO_2 molecule and the adsorbent surface and the smaller kinetic diameter leading the faster and easier penetration of CO_2 molecules inside the micropores. From the pure component adsorption data, the highest adsorbed CO_2, CH_4 and CO amounts were calculated as 1.61 mmolCO$_2$/g, 1.50 mmolCH$_4$/g and 1.47 mmolCO/g on CuTPA, respectively and 2.11 mmolCO$_2$/g, 1.90 mmolCH$_4$/g and 1.83 mmolCO/g on ZnTPA, and 5.20 mmolCO$_2$/g,

3.25 mmolCH$_4$/g and 1.91 mmolCO/g on TiTPA, and 5.54 mmolCO$_2$/g, 3.16 mmolCH$_4$/g and 2.59 mmolCO/g on AlTPA. The difference between adsorption capacities of MOFs caused by their textural properties; specific surface area, micropore volume and the average pore diameter. The highest ideal and real selectivities for CO$_2$ over CH$_4$ was attained over AlTPA (3.6, 7.5) and TiTPA (3.1, 8.0) at 10 mL/min of feed rate at 10 bar and due to their high selectivities AlTPA and TiTPA can be served as an excellent candidate for the selective sorption of CO$_2$ from SMR off-gas streams. However, at 10 mL/min and 1 bar the amount adsorbed of SMR components was very low on MOFs, indicating the compromise between adsorption capacity and selectivity should be made based on the purpose of the process (e.g., gas storage or selective gas separation). The selectivity of CuTPA and ZnTPA for CO$_2$ over CH$_4$ were found close to 1, thereby application of CuTPA and ZnTPA could be more suitable in gas storage rather than selective gas separation. The experimental adsorption isotherms of SMR compounds were fitted to Langmuir and virial models. Best fitted model was determined as virial model with lower ERRSQ, higher R^2 and narrower margin of error.

REFERENCES

Aaron, Adedibu C. Tella and Isaac Y. 2012. "Syntheses and Applications of Metal-Organic Frameworks Materials : A Review." *Acta Chimica & Pharmaceutica Indica* 2 (2).

Abedini, Reza, Mohammadreza Omidkhah, and Fatereh Dorosti. 2014. "Hydrogen separation and purification with poly (4-methyl-1-pentyne)/MIL 53 mixed matrix membrane based on reverse selectivity." *International Journal of Hydrogen Energy* 39 (15):7897-7909. doi: http://dx.doi.org/10.1016/j.ijhydene.2014.03.027.

Abid, Hussein Rasool, Zana Hassan Rada, Jin Shang, and Shaobin Wang. 2016. "Synthesis, characterization, and CO2 adsorption of three metal-organic frameworks (MOFs): MIL-53, MIL-96, and amino-MIL-53." *Polyhedron*. doi: http://dx.doi.org/10.1016/j.poly.2016.06.034.

Agarwal, Anshul, Lorenz T. Biegler, and Stephen E. Zitney. 2010. "Superstructure-Based Optimal Synthesis of Pressure Swing Adsorption Cycles for Precombustion CO2 Capture." *Industrial & Engineering Chemistry Research* 49 (11):5066-5079. doi: 10.1021/ie900873j.

Agueda, Vicente I., José A. Delgado, María A. Uguina, Pablo Brea, Aud I. Spjelkavik, Richard Blom, and Carlos Grande. 2015. "Adsorption and diffusion of H2, N2, CO, CH4 and CO2 in UTSA-16 metal-organic framework extrudates." *Chemical Engineering Science* 124:159-169. doi: http://dx.doi.org/10.1016/j.ces.2014.08.039.

Ahmad, Nazir, Hussein A. Younus, Adeel H. Chughtai, and Francis Verpoort. 2015. "Metal-organic molecular cages: applications of biochemical implications." *Chemical Society Reviews* 44 (1):9-25. doi: 10.1039/C4CS00222A.

Ahmed, Imteaz, and Sung Hwa Jhung. 2014. "Composites of metal–organic frameworks: Preparation and application in adsorption." *Materials Today* 17 (3):136-146. doi: http://dx.doi.org/10.1016/j.mattod.2014.03.002.

Ahn, Sol, Young-Woo You, Dong-Geun Lee, Ki-Hyun Kim, Min Oh, and Chang-Ha Lee. 2012. "Layered two- and four-bed PSA processes for H2 recovery from coal gas." *Chemical Engineering Science* 68 (1):413-423. doi: http://dx.doi.org/10.1016/j.ces.2011.09.053.

Al-Kutubi, Hanan, Jorge Gascon, Ernst J. R. Sudhölter, and Liza Rassaei. 2015. "Electrosynthesis of Metal–Organic Frameworks: Challenges and Opportunities." *ChemElectroChem* 2 (4):462-474. doi: 10.1002/celc.201402429.

Allen, Stephen J., Quan Gan, Ronan Matthews, and Pauline A. Johnson. 2003. "Comparison of optimised isotherm models for basic dye adsorption by kudzu." *Bioresource Technology* 88 (2):143-152. doi: http://dx.doi.org/10.1016/S0960-8524(02)00281-X.

Álvarez-Gutiérrez, N., M. V. Gil, F. Rubiera, and C. Pevida. 2016. "Adsorption performance indicators for the CO2/CH4 separation: Application to biomass-based activated carbons." *Fuel Processing Technology* 142:361-369. doi: http://dx.doi.org/10.1016/j.fuproc.2015.10.038.

Anbia, Mansoor, Vahid Hoseini, Sakineh Mandegarzad, Elahe Motaee, and Sara Sheykhi. 2014. "Synthesis of Nanoporous Metal Organic Framework MIL-53-Cu and Its Application for Gas Separation." *Iranian Journal of Chemistry and Chemical Engineering* 33 (4).

Anbia, Mansoor, and Sara Sheykhi. 2012. "Synthesis of nanoporous copper terephthalate [MIL-53(Cu)] as a novel methane-storage adsorbent." *Journal of Natural Gas Chemistry* 21 (6):680-684. doi: http://dx.doi.org/10.1016/S1003-9953(11)60419-2.

Anbia, Mansoor, and Sara Sheykhi. 2013. "Preparation of multi-walled carbon nanotube incorporated MIL-53-Cu composite metal–organic framework with enhanced methane sorption." *Journal of Industrial and Engineering Chemistry* 19 (5):1583-1586. doi: http://dx.doi.org/10.1016/j.jiec.2013.01.026.

Andirova, Dinara, Christopher F. Cogswell, Yu Lei, and Sunho Choi. 2016. "Effect of the structural constituents of metal organic frameworks on carbon dioxide capture." *Microporous and Mesoporous Materials* 219:276-305. doi: http://dx.doi.org/10.1016/j.micromeso.2015.07.029.

Angı, Deniz. 2016. "Synthesis of Aluminum Based Metal Organic Frameworks (Al-MOFs)."Master's Thesis, Materials Science and Engineering, Izmir Institute of Technology.

Arjmandi, Mehrzad, and Majid Pakizeh. 2014. "Mixed matrix membranes incorporated with cubic-MOF-5 for improved polyetherimide gas separation membranes: Theory and experiment." *Journal of Industrial and Engineering Chemistry* 20 (5):3857-3868. doi: http://dx.doi.org/10.1016/j.jiec.2013.12.091.

Armor, John N. 1999. "The multiple roles for catalysis in the production of H2." *Applied Catalysis A: General* 176 (2):159-176. doi: http://dx.doi.org/10.1016/S0926-860X(98)00244-0.

Armstrong, Mitchell R., Sethuraman Senthilnathan, Christopher J. Balzer, Bohan Shan, Liang Chen, and Bin Mu. 2017. "Particle size studies to reveal crystallization mechanisms of the metal organic framework HKUST-1 during sonochemical synthesis." *Ultrasonics Sonochemistry* 34:365-370. doi: http://dx.doi.org/10.1016/j.ultsonch.2016.06.011.

Arvind, R., S. Farooq, and D. M. Ruthven. 2002. "Analysis of a piston PSA process for air separation." *Chemical Engineering Science* 57 (3):419-433. doi: http://dx.doi.org/10.1016/S0009-2509(01)00374-8.

Bacsik, Zoltán, Ocean Cheung, Petr Vasiliev, and Niklas Hedin. 2016. "Selective separation of CO2 and CH4 for biogas upgrading on zeolite NaKA and SAPO-56." *Applied Energy* 162:613-621. doi: http://dx.doi.org/10.1016/j.apenergy.2015.10.109.

Barrer, R. M., and L. V. C. Rees. 1961. "Henry's law adsorption constants." *Transactions of the Faraday Society* 57 (0):999-1007. doi: 10.1039/TF9615700999.

Basu, Subhankar, Angels Cano-Odena, and Ivo F. J. Vankelecom. 2011. "MOF-containing mixed-matrix membranes for CO2/CH4 and CO2/N2 binary gas mixture separations." *Separation and Purification Technology* 81 (1):31-40. doi: http://dx.doi.org/10.1016/j.seppur.2011.06.037.

Batten, S. R. and Robson, R. 1998. "Interpenetrating Nets: Ordered, Periodic Entanglement." *Angewandte Chemie International Edition* 37 (11). doi: 10.1002/(SICI)1521-3773(19980619)37:11<1460::AID-ANIE1460>3.0.CO;2-Z.

Belhachemi, Meriem, and Fatima Addoun. 2011. "Comparative adsorption isotherms and modeling of methylene blue onto activated carbons." *Applied Water Science* 1 (3):111-117. doi: 10.1007/s13201-011-0014-1.

Benes, Jaromir, Marcelle Chauvet, Ondra Kamenik, Michael Kumhof, Douglas Laxton, Susanna Mursula, and Jack Selody. 2015. "The future of oil: Geology versus technology." *International Journal of Forecasting* 31 (1):207-221. doi: http://dx.doi.org/10.1016/j.ijforecast.2014.03.012.

Bhadra, Biswa Nath, Kyung Ho Cho, Nazmul Abedin Khan, Do-Young Hong, and Sung Hwa Jhung. 2015. "Liquid-Phase Adsorption of Aromatics over a Metal–Organic Framework and Activated Carbon: Effects of Hydrophobicity/Hydrophilicity of Adsorbents and Solvent Polarity." *The Journal of Physical Chemistry C* 119 (47):26620-26627. doi: 10.1021/acs.jpcc.5b09298.

Bolis, Vera. 2013. "Fundamentals in Adsorption at the Solid-Gas Interface. Concepts and Thermodynamics." In *Calorimetry and Thermal Methods in Catalysis*, edited by Aline Auroux, 3-50. Berlin, Heidelberg: Springer Berlin Heidelberg.

Bottani, E. J., Ismail M. K. Ismail, M. J. Bojan, and W. A. Steele. 1994. "Henry's Law Constants and Gas-Solid Potential for CO2 on Graphitized Carbon Blacks." *Langmuir* 10 (10):3805-3808. doi: 10.1021/la00022a067.

Boulinguiez, Benoit, Pierre Le Cloirec, and Dominique Wolbert. 2008. "Revisiting the Determination of Langmuir Parameters—Application to Tetrahydrothiophene Adsorption onto Activated Carbon." *Langmuir* 24 (13):6420-6424. doi: 10.1021/la800725s.

Brunauer, Stephen, Lola S. Deming, W. Edwards Deming, and Edward Teller. 1940. "On a Theory of the van der Waals Adsorption of Gases." *Journal of the American Chemical Society* 62 (7):1723-1732. doi: 10.1021/ja01864a025.

Çalışkan, Gonca. 2016. "Synthesis of Ti Based Metal Organic Frameworks (Ti-MOFs)."Master's Thesis, Chemical Engineering, Ege University.

Carson, Cantwell G., Kenneth Hardcastle, Justin Schwartz, Xiaotao Liu, Christina Hoffmann, Rosario A. Gerhardt, and Rina Tannenbaum. 2009. "Synthesis and Structure Characterization of Copper Terephthalate Metal–Organic Frameworks." *European Journal of Inorganic Chemistry* 2009 (16):2338-2343. doi: 10.1002/ejic.200801224.

Cavenati, Simone, Carlos A. Grande, and Alírio E. Rodrigues. 2006. "Removal of Carbon Dioxide from Natural Gas by Vacuum Pressure Swing Adsorption." *Energy & Fuels* 20 (6):2648-2659. doi: 10.1021/ef060119e.

CCP. 2008. "CO2 Capture Project: Three basic methods to separate gases."

Cen, Peiling, and Ralph T. Yang. 1986. "Bulk gas separation by pressure swing adsorption." *Industrial & Engineering Chemistry Fundamentals* 25 (4):758-767. doi: 10.1021/i100024a047.

Chai, Siew Wah, Mayuresh V. Kothare, and Shivaji Sircar. 2011. "Rapid Pressure Swing Adsorption for Reduction of Bed Size Factor of a Medical Oxygen Concentrator." *Industrial & Engineering Chemistry Research* 50 (14):8703-8710. doi: 10.1021/ie2005093.

Cheetham, Anthony K., C. N. R. Rao, and Russell K. Feller. 2006. "Structural diversity and chemical trends in hybrid inorganic-organic framework materials." *Chemical Communications* (46):4780-4795. doi: 10.1039/B610264F.

Chen, Chiachung. 2013. "Evaluation of Equilibrium Sorption Isotherm Equations." *The Open Chemical Engineering Journal* 7. doi: 10.2174/1874123101307010024.

Chen, Xiao Yuan, Vinh-Thang Hoang, Denis Rodrigue, and Serge Kaliaguine. 2013. "Optimization of continuous phase in amino-functionalized metal-organic framework (MIL-53) based co-polyimide mixed matrix membranes for CO2/CH4 separation." *RSC Advances* 3 (46):24266-24279. doi: 10.1039/C3RA43486A.

Chen, Xiao Yuan, Hoang Vinh-Thang, Denis Rodrigue, and Serge Kaliaguine. 2012. "Amine-Functionalized MIL-53 Metal–Organic Framework in Polyimide Mixed Matrix Membranes for CO2/CH4 Separation." *Industrial & Engineering Chemistry Research* 51 (19):6895-6906. doi: 10.1021/ie3004336.

Chen, Xunjun. 2015. "Modeling of Experimental Adsorption Isotherm Data." *Information* 6 (1). doi: 10.3390/info6010014.

Chen, Zhenxia, Shengchang Xiang, Hadi D. Arman, Jalal U. Mondal, Peng Li, Dongyuan Zhao, and Banglin Chen. 2011. "Three-Dimensional Pillar-Layered Copper(II) Metal−Organic Framework with Immobilized Functional OH Groups on Pore Surfaces for Highly Selective CO2/CH4 and C2H2/CH4 Gas Sorption at Room Temperature." *Inorganic Chemistry* 50 (8):3442-3446. doi: 10.1021/ic102347b.

Choi, Sunho, Jeffrey H Drese, and Christopher W Jones. 2009. "Adsorbent Materials for Carbon Dioxide Capture from Large Anthropogenic Point Sources." *ChemSusChem* 2 (9):796-854. doi: 10.1002/cssc.200900036.

Chowdhury, Pradip, Samuel Mekala, Frieder Dreisbach, and Sasidhar Gumma. 2012. "Adsorption of CO, CO2 and CH4 on Cu-BTC and MIL-101 metal organic frameworks: Effect of open metal sites and adsorbate polarity." *Microporous and Mesoporous Materials* 152:246-252. doi: http://dx.doi.org/10.1016/j.micromeso.2011.11.022.

Chughtai, Adeel H., Nazir Ahmad, Hussein A. Younus, A. Laypkov, and Francis Verpoort. 2015. "Metal-organic frameworks: versatile heterogeneous catalysts for efficient catalytic organic transformations." *Chemical Society Reviews* 44 (19):6804-6849. doi: 10.1039/C4CS00395K.

Çiçek, Ahmet Uğur. 2014. "Synthesis of copper based metal organic framework for separation of CO2/H2 at high pressure."Master's Thesis, Chemical Engineering, İzmir Institute of Technology.

Crane, Johanna L., Kelly E. Anderson, and Samantha G. Conway. 2015. "Hydrothermal Synthesis and Characterization of a Metal–Organic Framework by Thermogravimetric Analysis, Powder X-ray Diffraction, and Infrared Spectroscopy: An Integrative Inorganic Chemistry Experiment." *Journal of Chemical Education* 92 (2):373-377. doi: 10.1021/ed5000839.

Cui, Pei-Pei, Xiu-Du Zhang, Yue Zhao, Kai Chen, Peng Wang, and Wei-Yin Sun. 2015. "Structure, topology and property of metal-organic frameworks with pyridine-3,5-bis(phenyl-4-carboxylate) and varied metal centers." *Microporous and Mesoporous Materials* 208:188-195. doi: http://dx.doi.org/10.1016/j.micromeso.2015.02.005.

Cychosz, Katie A., and Adam J. Matzger. 2010. "Water Stability of Microporous Coordination Polymers and the Adsorption of Pharmaceuticals from Water." *Langmuir* 26 (22):17198-17202. doi: 10.1021/la103234u.

Czaja, Alexander U., Natalia Trukhan, and Ulrich Muller. 2009. "Industrial applications of metal-organic frameworks." *Chemical Society Reviews* 38 (5):1284-1293. doi: 10.1039/B804680H.

da Silva, Gilvaldo G., Cecília S. Silva, Rogério T. Ribeiro, Célia M. Ronconi, Bráulio S. Barros, Jorge L. Neves, and Severino Alves Júnior. 2016. "Sonoelectrochemical synthesis of metal-organic frameworks." *Synthetic Metals* 220:369-373. doi: http://dx.doi.org/10.1016/j.synthmet.2016.07.003.

Dantas, Tirzhá L. P., Francisco Murilo T. Luna, Ivanildo J. Silva Jr, Antonio Eurico B. Torres, Diana C. S. de Azevedo, Alírio E. Rodrigues, and Regina F. P. M. Moreira. 2011. "Carbon dioxide–nitrogen separation through pressure swing adsorption." *Chemical Engineering Journal* 172 (2–3):698-704. doi: http://dx.doi.org/10.1016/j.cej.2011.06.037.

Davini, Paolo. 2002. "Flue gas treatment by activated carbon obtained from oil-fired fly ash." *Carbon* 40 (11):1973-1979. doi: http://dx.doi.org/10.1016/S0008-6223(02)00049-0.

Davison, John. 2007. "Performance and costs of power plants with capture and storage of CO2." *Energy* 32 (7):1163-1176. doi: http://dx.doi.org/10.1016/j.energy.2006.07.039.

Dechamps, P., and P. Pilavachi, A. 2004. "Actions de recherche et développement visant à réduire les émissions de CO2 dans l'Union européenne." *Oil & Gas Science and Technology - Rev. IFP* 59 (3):323-330.

Dhakshinamoorthy, Amarajothi, and Hermenegildo Garcia. 2014. "Metal-organic frameworks as solid catalysts for the synthesis of nitrogen-containing heterocycles." *Chemical Society Reviews* 43 (16):5750-5765. doi: 10.1039/C3CS60442J.

Dias, Elton M., and Camille Petit. 2015. "Towards the use of metal-organic frameworks for water reuse: a review of the recent advances in the field of organic pollutants removal and degradation and the next steps in the field." *Journal of Materials Chemistry A* 3 (45):22484-22506. doi: 10.1039/C5TA05440K.

Do, D.D. 1998. *Adsorption Analysis: Equilibria and Kinetics: (With CD Containing Computer Matlab Programs)*.

Duan, Xing, Jianfeng Cai, Jiancan Yu, Chuande Wu, Yuanjing Cui, Yu Yang, and Guodong Qian. 2013. "Three-dimensional copper (II) metal–organic framework with open metal sites and anthracene nucleus for highly selective C2H2/CH4 and C2H2/CO2 gas separation at room temperature." *Microporous and Mesoporous Materials* 181:99-104. doi: http://dx.doi.org/10.1016/j.micromeso.2013.07.019.

Eddaoudi, Mohamed, Hailian Li, and O. M. Yaghi. 2000. "Highly Porous and Stable Metal−Organic Frameworks: Structure Design and Sorption Properties." *Journal of the American Chemical Society* 122 (7):1391-1397. doi: 10.1021/ja9933386.

Edwards, P. P., V. L. Kuznetsov, W. I. F. David, and N. P. Brandon. 2008. "Hydrogen and fuel cells: Towards a sustainable energy future." *Energy Policy* 36 (12):4356-4362. doi: http://dx.doi.org/10.1016/j.enpol.2008.09.036.

Esteves, Isabel A. A. C., Marta S. S. Lopes, Pedro M. C. Nunes, and José P. B. Mota. 2008. "Adsorption of natural gas and biogas components on activated carbon." *Separation and Purification Technology* 62 (2):281-296. doi: http://dx.doi.org/10.1016/j.seppur.2008.01.027.

Ferey, Gerard. 2008. "Hybrid porous solids: past, present, future." *Chemical Society Reviews* 37 (1):191-214. doi: 10.1039/B618320B.

Ferey, Gerard, Michel Latroche, Christian Serre, Franck Millange, Thierry Loiseau, and Annick Percheron-Guegan. 2003. "Hydrogen adsorption in the nanoporous metal-benzenedicarboxylate M(OH)(O2C-C6H4-CO2) (M = Al3+, Cr3+), MIL-53." *Chemical Communications* (24):2976-2977. doi: 10.1039/B308903G.

Ferreira, Alexandre F. P., Ana Mafalda Ribeiro, Seda Kulaç, and Alírio E. Rodrigues. 2015. "Methane purification by adsorptive processes on MIL-53(Al)." *Chemical Engineering Science* 124:79-95. doi: http://dx.doi.org/10.1016/j.ces.2014.06.014.

Finsy, V., L. Ma, L. Alaerts, D. E. De Vos, G. V. Baron, and J. F. M. Denayer. 2009. "Separation of CO2/CH4 mixtures with the MIL-53(Al) metal–organic framework." *Microporous and Mesoporous Materials* 120 (3):221-227. doi: http://dx.doi.org/10.1016/j.micromeso.2008.11.007.

Frankel, Jeffrey A. 2013. *National security warrants slowing domestic oil depletion, not accelerating it*: Cambridge, Mass. : Harvard Univ., John F. Kennedy School of Government. Arbeitspapier, Working Paper, Graue Literatur, Non-commercial literature.

Furukawa, Hiroyasu, Kyle E. Cordova, Michael O'Keeffe, and Omar M. Yaghi. 2013. "The Chemistry and Applications of Metal-Organic Frameworks." *Science* 341 (6149). doi: 10.1126/science.1230444.

Geankoplis, C.J. 1993. *Transport Processes and Unit Operations*: PTR Prentice Hall.

Grande, Carlos A., Richard Blom, Andreas Möller, and Jens Möllmer. 2013. "High-pressure separation of CH4/CO2 using activated carbon." *Chemical Engineering Science* 89:10-20. doi: http://dx.doi.org/10.1016/j.ces.2012.11.024.

Grande, Carlos A., and Alírio E. Rodrigues. 2005. "Propane/Propylene Separation by Pressure Swing Adsorption Using Zeolite 4A." *Industrial & Engineering Chemistry Research* 44 (23):8815-8829. doi: 10.1021/ie050671b.

Haydel, J. J., and Riki Kobayashi. 1967. "Adsorption Equilibria in Methane-Propane-Silica Gel System at High Pressures." *Industrial & Engineering Chemistry Fundamentals* 6 (4):546-554. doi: 10.1021/i160024a010.

Hendon, Christopher H., Davide Tiana, Marc Fontecave, Clément Sanchez, Loïc D'arras, Capucine Sassoye, Laurence Rozes, Caroline Mellot-Draznieks, and Aron Walsh. 2013. "Engineering the Optical Response of the Titanium-MIL-125 Metal–Organic Framework through Ligand Functionalization." *Journal of the American Chemical Society* 135 (30):10942-10945. doi: 10.1021/ja405350u.

Hermes, Stephan, Felicitas Schroder, Saeed Amirjalayer, Rochus Schmid, and Roland A. Fischer. 2006. "Loading of porous metal-organic open frameworks with organometallic CVD precursors: inclusion compounds of the type [LnM]a@MOF-5." *Journal of Materials Chemistry* 16 (25):2464-2472. doi: 10.1039/B603664C.

Heymans, N., S. Vaesen, and G. De Weireld. 2012. "A complete procedure for acidic gas separation by adsorption on MIL-53 (Al)." *Microporous and Mesoporous Materials* 154:93-99. doi: http://dx.doi.org/10.1016/j.micromeso.2011.10.020.

Hill, Robert J., De-Liang Long, Neil R. Champness, Peter Hubberstey, and Martin Schröder. 2005. "New Approaches to the Analysis of High Connectivity Materials: Design Frameworks Based upon 44- and 63-Subnet Tectons." *Accounts of Chemical Research* 38 (4):335-348. doi: 10.1021/ar040174b.

Huang, Limin, Huanting Wang, Jinxi Chen, Zhengbao Wang, Jinyu Sun, Dongyuan Zhao, and Yushan Yan. 2003. "Synthesis, morphology control, and properties of porous metal–organic coordination polymers." *Microporous and Mesoporous Materials* 58 (2):105-114. doi: http://dx.doi.org/10.1016/S1387-1811(02)00609-1.

Huxford, Rachel C., Joseph Della Rocca, and Wenbin Lin. 2010. "Metal-Organic Frameworks as Potential Drug Carriers." *Current opinion in chemical biology* 14 (2):262-268. doi: 10.1016/j.cbpa.2009.12.012.

IEA. 2010. *Energy Technology Perspectives 2010*: OECD Publishing.

Im, Ji Hyuk, Nakeun Ko, Seung Jae Yang, Hye Jeong Park, Jaheon Kim, and Chong Rae Park. 2014. "Enhanced water stability and CO2 gas sorption properties of a methyl functionalized titanium metal-organic framework." *New Journal of Chemistry* 38 (7):2752-2755. doi: 10.1039/C4NJ00138A.

Ipcc. 2014. *Climate Change 2014: Impacts, Adaptation, and Vulnerability. Part B: Regional Aspects. Contribution of Working Group II to the Fifth Assessment Report of the Intergovernmental Panel on Climate Change [Barros, V.R., C.B. Field, D.J. Dokken, M.D. Mastrandrea, K.J. Mach, T.E. Bilir, M. Chatterjee, K.L. Ebi, Y.O. Estrada, R.C. Genova, B. Girma, E.S. Kissel, A.N. Levy, S. MacCracken, P.R. Mastrandrea, and L.L. White (eds.)]*. Cambridge, United Kingdom and New York, NY, USA: Cambridge University Press.

Jain, I. P. 2009. "Hydrogen the fuel for 21st century." *International Journal of Hydrogen Energy* 34 (17):7368-7378. doi: http://dx.doi.org/10.1016/j.ijhydene.2009.05.093.

Kacem, Mariem, Mario Pellerano, and Arnaud Delebarre. 2015. "Pressure swing adsorption for CO2/N2 and CO2/CH4 separation: Comparison between activated carbons and zeolites performances." *Fuel Processing Technology* 138:271-283. doi: http://dx.doi.org/10.1016/j.fuproc.2015.04.032.

Karra, Jagadeswara R., Bogna E. Grabicka, You-Gui Huang, and Krista S. Walton. 2013. "Adsorption study of CO2, CH4, N2, and H2O on an interwoven copper carboxylate metal–organic framework (MOF-14)." *Journal of Colloid and Interface Science* 392:331-336. doi: http://dx.doi.org/10.1016/j.jcis.2012.10.018.

Karra, Jagadeswara R., and Krista S. Walton. 2010. "Molecular Simulations and Experimental Studies of CO2, CO, and N2 Adsorption in Metal−Organic Frameworks." *The Journal of Physical Chemistry C* 114 (37):15735-15740. doi: 10.1021/jp105519h.

Kaye, Steven S., Anne Dailly, Omar M. Yaghi, and Jeffrey R. Long. 2007. "Impact of Preparation and Handling on the Hydrogen Storage Properties of Zn4O(1,4-benzenedicarboxylate)3 (MOF-5)." *Journal of the American Chemical Society* 129 (46):14176-14177. doi: 10.1021/ja076877g.

Ke, Fu-Sheng, Yu-Shan Wu, and Hexiang Deng. 2015. "Metal-organic frameworks for lithium ion batteries and supercapacitors." *Journal of Solid State Chemistry* 223:109-121. doi: http://dx.doi.org/10.1016/j.jssc.2014.07.008.

Keskin, Seda, and Seda Kızılel. 2011. "Biomedical Applications of Metal Organic Frameworks." *Industrial & Engineering Chemistry Research* 50 (4):1799-1812. doi: 10.1021/ie101312k.

Khajuria, Harish, and Efstratios N. Pistikopoulos. 2013. "Optimization and Control of Pressure Swing Adsorption Processes Under Uncertainty." *AIChE Journal* 59 (1):120-131. doi: 10.1002/aic.13783.

Khan, Nazmul Abedin, and Sung Hwa Jhung. 2015. "Synthesis of metal-organic frameworks (MOFs) with microwave or ultrasound: Rapid reaction, phase-selectivity, and size reduction." *Coordination Chemistry Reviews* 285:11-23. doi: http://dx.doi.org/10.1016/j.ccr.2014.10.008.

Khunpolgrang, Jatupol, Songwut Yosantea, Aroon Kongnoo, and Chantaraporn Phalakornkule. 2015. "Alternative PSA process cycle with combined vacuum regeneration and nitrogen purging for CH4/CO2 separation." *Fuel* 140:171-177. doi: http://dx.doi.org/10.1016/j.fuel.2014.09.100.

Kim, Young Jun, Young Suk Nam, and Yong Tae Kang. 2015. "Study on a numerical model and PSA (pressure swing adsorption) process experiment for CH4/CO2 separation from biogas." *Energy* 91:732-741. doi: http://dx.doi.org/10.1016/j.energy.2015.08.086.

Kitagawa, Susumu, Ryo Kitaura, and Shin-ichiro Noro. 2004. "Functional Porous Coordination Polymers." *Angewandte Chemie International Edition* 43 (18):2334-2375. doi: 10.1002/anie.200300610.

Klinowski, Jacek, Filipe A. Almeida Paz, Patricia Silva, and Joao Rocha. 2011. "Microwave-Assisted Synthesis of Metal-Organic Frameworks." *Dalton Transactions* 40 (2):321-330. doi: 10.1039/C0DT00708K.

Kumar, Pawan, Akash Deep, and Ki-Hyun Kim. 2015. "Metal organic frameworks for sensing applications." *TrAC Trends in Analytical Chemistry* 73:39-53. doi: http://dx.doi.org/10.1016/j.trac.2015.04.009.

Lee, J. Y, D. H Olson, L. Pan, T. J Emge, and J. Li. 2007. "Microporous Metal–Organic Frameworks with High Gas Sorption and Separation Capacity." *Advanced Functional Materials* 17 (8):1255-1262. doi: 10.1002/adfm.200600944.

Lee, Yu-Ri, Jun Kim, and Wha-Seung Ahn. 2013. "Synthesis of metal-organic frameworks: A mini review." *Korean Journal of Chemical Engineering* 30 (9):1667-1680. doi: 10.1007/s11814-013-0140-6.

Li, Jian-Rong, Ryan J. Kuppler, and Hong-Cai Zhou. 2009. "Selective gas adsorption and separation in metal-organic frameworks." *Chemical Society Reviews* 38 (5):1477-1504. doi: 10.1039/B802426J.

Li, Junmin, Jiangfeng Yang, Libo Li, and Jinping Li. 2014. "Separation of CO2/CH4 and CH4/N2 mixtures using MOF-5 and Cu3(BTC)2." *Journal of Energy Chemistry* 23 (4):453-460. doi: http://dx.doi.org/10.1016/S2095-4956(14)60171-6.

Li, Lei, Shenglin Xiang, Shuqi Cao, Jianyong Zhang, Gangfeng Ouyang, Liuping Chen, and Cheng-Yong Su. 2013. "A synthetic route to ultralight hierarchically micro/mesoporous Al(III)-carboxylate metal-organic aerogels." *Nature Communications* 4:1774. doi: 10.1038/ncomms2757

http://www.nature.com/articles/ncomms2757#supplementary-information.

Li, Siqing, Yifa Chen, Xiaokun Pei, Shenghan Zhang, Xiao Feng, Junwen Zhou, and Bo Wang. 2016. "Water Purification: Adsorption over Metal-Organic Frameworks." *Chinese Journal of Chemistry* 34 (2):175-185. doi: 10.1002/cjoc.201500761.

Lin, Kuen-Song, Abhijit Krishna Adhikari, Chi-Nan Ku, Chao-Lung Chiang, and Hua Kuo. 2012. "Synthesis and characterization of porous HKUST-1 metal organic frameworks for hydrogen storage." *International Journal of Hydrogen Energy* 37 (18):13865-13871. doi: http://dx.doi.org/10.1016/j.ijhydene.2012.04.105.

Ling, Yun, Zhen-Xia Chen, Fu-Peng Zhai, Ya-Ming Zhou, Lin-Hong Weng, and Dong-Yuan Zhao. 2011. "A zinc(ii) metal-organic framework based on triazole and dicarboxylate ligands for selective adsorption of hexane isomers." *Chemical Communications* 47 (25):7197-7199. doi: 10.1039/C1CC12253C.

Littlefield, Scott R. 2013. "Security, independence, and sustainability: Imprecise language and the manipulation of energy policy in the United States." *Energy Policy* 52:779-788. doi: http://dx.doi.org/10.1016/j.enpol.2012.10.040.

Liu, Wei, and Xue-Bo Yin. 2016. "Metal–organic frameworks for electrochemical applications." *TrAC Trends in Analytical Chemistry* 75:86-96. doi: http://dx.doi.org/10.1016/j.trac.2015.07.011.

Loiseau, Thierry, Hervé Muguerra, Gérard Férey, Mohamed Haouas, and Francis Taulelle. 2005. "Synthesis and structural characterization of a new open-framework zinc terephthalate Zn3(OH)2(bdc)2·2DEF, with infinite Zn–(μ3-OH)–Zn chains." *Journal of Solid State Chemistry* 178 (3):621-628. doi: http://dx.doi.org/10.1016/j.jssc.2004.12.004.

Loiseau, Thierry, Christian Serre, Clarisse Huguenard, Gerhard Fink, Francis Taulelle, Marc Henry, Thierry Bataille, and Gérard Férey. 2004. "A Rationale for the Large Breathing of the Porous Aluminum Terephthalate (MIL-53) Upon Hydration." *Chemistry – A European Journal* 10 (6):1373-1382. doi: 10.1002/chem.200305413.

Lopes, Filipe V. S., Carlos A. Grande, and Alírio E. Rodrigues. 2011. "Activated carbon for hydrogen purification by pressure swing adsorption: Multicomponent breakthrough curves and PSA performance." *Chemical Engineering Science* 66 (3):303-317. doi: http://dx.doi.org/10.1016/j.ces.2010.10.034.

Luo, Xi-Ping, Sheng-Yuan Fu, Yi-Ming Du, Jian-Zhong Guo, and Bing Li. 2017. "Adsorption of methylene blue and malachite green from aqueous solution by sulfonic acid group modified MIL-101." *Microporous and Mesoporous Materials* 237:268-274. doi: http://dx.doi.org/10.1016/j.micromeso.2016.09.032.

M. A. S. D. Barros, P. A. Arroyo and E. A. Silva   2013. "General Aspects of Aqueous Sorption Process in Fixed Beds." *InTech Journals*. doi: 10.5772/51954.

Ma, Liqing, and Wenbin Lin. 2008. "Chirality-Controlled and Solvent-Templated Catenation Isomerism in Metal−Organic Frameworks." *Journal of the American Chemical Society* 130 (42):13834-13835. doi: 10.1021/ja804944r.

Masel, R.I. 1996. *Principles of Adsorption and Reaction on Solid Surfaces*: Wiley.

Maurer, S., A. Mersmann, and W. Peukert. 2001. "Henry coefficients of adsorption predicted from solid Hamaker constants." *Chemical Engineering Science* 56 (11):3443-3453. doi: http://dx.doi.org/10.1016/S0009-2509(01)00033-1.

McCabe, W.L., J.C. Smith, and P. Harriott. 1985. *Unit operations of chemical engineering*: McGraw-Hill.

McKay, Gordon, Alireza Mesdaghinia, Simin Nasseri, Mahdi Hadi, and Mehri Solaimany Aminabad. 2014. "Optimum isotherms of dyes sorption by activated carbon: Fractional theoretical capacity & error analysis." *Chemical Engineering Journal* 251:236-247. doi: http://dx.doi.org/10.1016/j.cej.2014.04.054.

McNamara, Nicholas D., Gregory T. Neumann, Erin T. Masko, Jacqueline A. Urban, and Jason C. Hicks. 2013. "Catalytic performance and stability of (V) MIL-47 and (Ti) MIL-125 in the oxidative desulfurization of heterocyclic aromatic sulfur compounds." *Journal of Catalysis* 305:217-226. doi: http://dx.doi.org/10.1016/j.jcat.2013.05.021.

Miller, Richard G., and Steven R. Sorrell. 2014. "The future of oil supply." *Philosophical transactions. Series A, Mathematical, physical, and engineering sciences* 372 (2006):20130179. doi: 10.1098/rsta.2013.0179.

Millward, Andrew R., and Omar M. Yaghi. 2005. "Metal−Organic Frameworks with Exceptionally High Capacity for Storage of Carbon Dioxide at Room Temperature." *Journal of the American Chemical Society* 127 (51):17998-17999. doi: 10.1021/ja0570032.

Mishra, Prashant, Samuel Mekala, Freider Dreisbach, Bishnupada Mandal, and Sasidhar Gumma. 2012. "Adsorption of CO2, CO, CH4 and N2 on a zinc based metal organic framework." *Separation and Purification Technology* 94:124-130. doi: http://dx.doi.org/10.1016/j.seppur.2011.09.041.

Mohammadi, Nima, Mohammad I. Hossain, Armin D. Ebner, and James A. Ritter. 2016. "New Pressure Swing Adsorption Cycle Schedules for Producing High-Purity Oxygen Using Carbon Molecular Sieve." *Industrial & Engineering Chemistry Research* 55 (40):10758-10770. doi: 10.1021/acs.iecr.6b02570.

Moreira, Mariana A., João C. Santos, Alexandre F. P. Ferreira, José M. Loureiro, Florence Ragon, Patricia Horcajada, Pascal G. Yot, Christian Serre, and Alírio E. Rodrigues. 2012. "Toward Understanding the Influence of Ethylbenzene in p-Xylene Selectivity of the Porous Titanium Amino Terephthalate MIL-125(Ti): Adsorption Equilibrium and Separation of Xylene Isomers." *Langmuir* 28 (7):3494-3502. doi: 10.1021/la204969t.

Mounfield Iii, William P., Uma Tumuluri, Yang Jiao, Meijun Li, Sheng Dai, Zili Wu, and Krista S. Walton. 2016. "Role of defects and metal coordination on adsorption of acid gases in MOFs and metal oxides: An in situ IR spectroscopic study." *Microporous and Mesoporous Materials* 227:65-75. doi: http://dx.doi.org/10.1016/j.micromeso.2016.02.023.

Mueller, U., M. Schubert, F. Teich, H. Puetter, K. Schierle-Arndt, and J. Pastre. 2006. "Metal-organic frameworks-prospective industrial applications." *Journal of Materials Chemistry* 16 (7):626-636. doi: 10.1039/B511962F.

Nowotny, J., C. C. Sorrell, L. R. Sheppard, and T. Bak. 2005. "Solar-hydrogen: Environmentally safe fuel for the future." *International Journal of Hydrogen Energy* 30 (5):521-544. doi: http://dx.doi.org/10.1016/j.ijhydene.2004.06.012.

Oriňáková, Renáta, and Andrej Oriňák. 2011. "Recent applications of carbon nanotubes in hydrogen production and storage." *Fuel* 90 (11):3123-3140. doi: http://dx.doi.org/10.1016/j.fuel.2011.06.051.

Panella, B., and M. Hirscher. 2005. "Hydrogen Physisorption in Metal–Organic Porous Crystals." *Advanced Materials* 17 (5):538-541. doi: 10.1002/adma.200400946.

Panella, B., M. Hirscher, H. Pütter, and U. Müller. 2006. "Hydrogen Adsorption in Metal–Organic Frameworks: Cu-MOFs and Zn-MOFs Compared." *Advanced Functional Materials* 16 (4):520-524. doi: 10.1002/adfm.200500561.

Peter, Sunil A., Gino V. Baron, Jorge Gascon, Freek Kapteijn, and Joeri F. M. Denayer. 2013. "Dynamic desorption of CO2 and CH4 from amino-MIL-53(Al) adsorbent." *Adsorption* 19 (6):1235-1244. doi: 10.1007/s10450-013-9564-x.

Phan, Nam T. S., Tung T. Nguyen, Khoa D. Nguyen, and Anh X. T. Vo. 2013. "An open metal site metal–organic framework Cu(BDC) as a promising heterogeneous catalyst for the modified Friedländer reaction." *Applied Catalysis A: General* 464–465:128-135. doi: http://dx.doi.org/10.1016/j.apcata.2013.05.034.

Rada, Zana Hassan, Hussein Rasool Abid, Jin Shang, Yingdian He, Paul Webley, Shaomin Liu, Hongqi Sun, and Shaobin Wang. 2015. "Effects of amino functionality on uptake of CO2, CH4 and selectivity of CO2/CH4 on titanium based MOFs." *Fuel* 160:318-327. doi: http://dx.doi.org/10.1016/j.fuel.2015.07.088.

Rallapalli, Phani, K. P. Prasanth, Dinesh Patil, Rajesh S. Somani, R. V. Jasra, and H. C. Bajaj. 2011. "Sorption studies of CO2, CH4, N2, CO, O2 and Ar on nanoporous aluminum terephthalate [MIL-53(Al)]." *Journal of Porous Materials* 18 (2):205-210. doi: 10.1007/s10934-010-9371-7.

Ramaswamy, S., H.J. Huang, and B.V. Ramarao. 2013. *Separation and Purification Technologies in Biorefineries*: Wiley.

Ramsahye, Naseem A., Philippe Trens, Céline Shepherd, Philippe Gonzalez, Thuy Khuong Trung, Florence Ragon, and Christian Serre. 2014. "The effect of pore shape on hydrocarbon selectivity on UiO-66(Zr), HKUST-1 and MIL-125(Ti) metal organic frameworks: Insights from molecular simulations and chromatography." *Microporous and Mesoporous Materials* 189:222-231. doi: http://dx.doi.org/10.1016/j.micromeso.2013.09.005.

Ranocchiari, Marco, and Jeroen Anton van Bokhoven. 2011. "Catalysis by metal-organic frameworks: fundamentals and opportunities." *Physical Chemistry Chemical Physics* 13 (14):6388-6396. doi: 10.1039/C0CP02394A.

Regufe, Maria João, Javier Tamajon, Ana M. Ribeiro, Alexandre Ferreira, U. Hwang Lee, Young Kyu Hwang, Jong-San Chang, Christian Serre, José M. Loureiro, and Alírio E. Rodrigues. 2015. "Syngas Purification by Porous Amino-Functionalized Titanium Terephthalate MIL-125." *Energy & Fuels* 29 (7):4654-4664. doi: 10.1021/acs.energyfuels.5b00975.

Ren, Xiao-Yan, and Le-Hui Lu. 2015. "Luminescent nanoscale metal–organic frameworks for chemical sensing." *Chinese Chemical Letters* 26 (12):1439-1445. doi: http://dx.doi.org/10.1016/j.cclet.2015.10.014.

Rezaei, F., and P. Webley. 2010. "Structured adsorbents in gas separation processes." *Separation and Purification Technology* 70 (3):243-256. doi: http://dx.doi.org/10.1016/j.seppur.2009.10.004.

Rezaei, Fateme, and Paul Webley. 2009. "Optimum structured adsorbents for gas separation processes." *Chemical Engineering Science* 64 (24):5182-5191. doi: http://dx.doi.org/10.1016/j.ces.2009.08.029.

Rosi, Nathaniel L., Juergen Eckert, Mohamed Eddaoudi, David T. Vodak, Jaheon Kim, Michael O'Keeffe, and Omar M. Yaghi. 2003. "Hydrogen Storage in Microporous Metal-Organic Frameworks." *Science* 300 (5622):1127-1129. doi: 10.1126/science.1083440.

Rowsell, Jesse L. C., and Omar M. Yaghi. 2004. "Metal–organic frameworks: a new class of porous materials." *Microporous and Mesoporous Materials* 73 (1–2):3-14. doi: http://dx.doi.org/10.1016/j.micromeso.2004.03.034.

Ruthven, D.M. 1984. *Principles of Adsorption and Adsorption Processes*: Wiley.

Ruthven, D.M., S. Farooq, and K.S. Knaebel. 1994. *Pressure swing adsorption*: VCH Publishers.

Safarifard, Vahid, and Ali Morsali. 2015. "Applications of ultrasound to the synthesis of nanoscale metal–organic coordination polymers." *Coordination Chemistry Reviews* 292:1-14. doi: http://dx.doi.org/10.1016/j.ccr.2015.02.014.

Saha, Dipendu, Zuojun Wei, and Shuguang Deng. 2009. "Hydrogen adsorption equilibrium and kinetics in metal–organic framework (MOF-5) synthesized with DEF approach." *Separation and Purification Technology* 64 (3):280-287. doi: http://dx.doi.org/10.1016/j.seppur.2008.10.022.

Sahiner, Nurettin, Kivanc Sel, Omer Faruk Ozturk, Sahin Demirci, and Gozde Terzi. 2014. "Facile synthesis and characterization of trimesic acid-Cu based metal organic frameworks." *Applied Surface Science* 314:663-669. doi: http://dx.doi.org/10.1016/j.apsusc.2014.07.023.

Sanchez-Sanchez, Manuel, Negash Getachew, Kenya Diaz, Manuel Diaz-Garcia, Yonas Chebude, and Isabel Diaz. 2015. "Synthesis of metal-organic frameworks in water at room temperature: salts as linker sources." *Green Chemistry* 17 (3):1500-1509. doi: 10.1039/C4GC01861C.

Segakweng, Tshiamo, Nicholas M. Musyoka, Jianwei Ren, Philip Crouse, and Henrietta W. Langmi. 2016. "Comparison of MOF-5- and Cr-MOF-derived carbons for hydrogen storage application." *Research on Chemical Intermediates* 42 (5):4951-4961. doi: 10.1007/s11164-015-2338-1.

Seki, K., and W. Mori. 2002. "Syntheses and Characterization of Microporous Coordination Polymers with Open Frameworks." *The Journal of Physical Chemistry B* 106 (6):1380-1385. doi: 10.1021/jp0130416.

Sherif, Fawzy G. 1970. "Heavy Metal Terephthalates." *Product R&D* 9 (3):408-412. doi: 10.1021/i360035a026.

Sigot, Léa, Marta Fontseré Obis, Hassen Benbelkacem, Patrick Germain, and Gaëlle Ducom. 2016. "Comparing the performance of a 13X zeolite and an impregnated activated carbon for H2S removal from biogas to fuel an SOFC: Influence of water." *International Journal of Hydrogen Energy* 41 (41):18533-18541. doi: http://dx.doi.org/10.1016/j.ijhydene.2016.08.100.

Silva, Bruna, Ioan Solomon, Ana M. Ribeiro, U. Hwang Lee, Young Kyu Hwang, Jong-San Chang, José M. Loureiro, and Alírio E. Rodrigues. 2013. "H2 purification by pressure swing adsorption using CuBTC." *Separation and Purification Technology* 118:744-756. doi: http://dx.doi.org/10.1016/j.seppur.2013.08.024.

Silva, José A. C., Adelino F. Cunha, Kristin Schumann, and Alírio E. Rodrigues. 2014. "Binary adsorption of CO2/CH4 in binderless beads of 13X zeolite." *Microporous and Mesoporous Materials* 187:100-107. doi: http://dx.doi.org/10.1016/j.micromeso.2013.12.017.

Silva, José A. C., Francisco A. Da Silva, and Alírio E. Rodrigues. 2000. "Separation of n/iso paraffins by PSA." *Separation and Purification Technology* 20 (1):97-110. doi: http://dx.doi.org/10.1016/S1383-5866(00)00064-2.

Singh, Niraj K., Meenakshi Hardi, and Viktor P. Balema. 2013. "Mechanochemical synthesis of an yttrium based metal-organic framework." *Chemical Communications* 49 (10):972-974. doi: 10.1039/C2CC36325A.

Sircar, S., and T. C. Golden. 2000. "Purification of Hydrogen by Pressure Swing Adsorption." *Separation Science and Technology* 35 (5):667-687. doi: 10.1081/SS-100100183.

Sircar, S., T. C. Golden, and M. B. Rao. 1996. "Activated carbon for gas separation and storage." *Carbon* 34 (1):1-12. doi: http://dx.doi.org/10.1016/0008-6223(95)00128-X.

Skogestad, S. 2008. *Chemical and Energy Process Engineering*: CRC Press.

Smithson, M. 2003. *Confidence Intervals*: SAGE Publications.

Songolzadeh, Mohammad, Mansooreh Soleimani, and Maryam Takht Ravanchi. 2015. "Using modified Avrami kinetic and two component isotherm equation for modeling of CO2/N2 adsorption over a 13X zeolite bed." *Journal of Natural Gas Science and Engineering* 27, Part 2:831-841. doi: http://dx.doi.org/10.1016/j.jngse.2015.09.029.

Stock, Norbert, and Shyam Biswas. 2012. "Synthesis of Metal-Organic Frameworks (MOFs): Routes to Various MOF Topologies, Morphologies, and Composites." *Chemical Reviews* 112 (2):933-969. doi: 10.1021/cr200304e.

Subramanyam, B., and A. Das. 2009. "Linearized and non-linearized isotherm models comparative study on adsorption of aqueous phenol solution in soil." *International Journal of Environmental Science & Technology* 6 (4):633-640. doi: 10.1007/bf03326104.

Subramanyam, Busetty, and Ashutosh Das. 2014. "Linearised and non-linearised isotherm models optimization analysis by error functions and statistical means." *Journal of Environmental Health Science and Engineering* 12:92-92. doi: 10.1186/2052-336X-12-92.

Sun, Daofeng, Shengqian Ma, Yanxiong Ke, David J. Collins, and Hong-Cai Zhou. 2006. "An Interweaving MOF with High Hydrogen Uptake." *Journal of the American Chemical Society* 128 (12):3896-3897. doi: 10.1021/ja058777l.

Taqvi, Syed M., and M. Douglas LeVan. 1997. "Virial Description of Two-Component Adsorption on Homogeneous and Heterogeneous Surfaces." *Industrial & Engineering Chemistry Research* 36 (6):2197-2206. doi: 10.1021/ie960456i.

Tari, Nesa Esmaeilian, Azadeh Tadjarodi, Javad Tamnanloo, and Shohreh Fatemi. 2015. "Facile and fast, one pot microwave synthesis of metal organic framework copper terephthalate and study CO2 and CH4 adsorption on it." *Journal of Porous Materials* 22 (5):1161-1169. doi: 10.1007/s10934-015-9992-y.

Tari, Nesa Esmaeilian, Azadeh Tadjarodi, Javad Tamnanloo, and Shohreh Fatemi. 2016a. "One pot microwave synthesis of MCM-41/Cu based MOF composite with improved CO2 adsorption and selectivity." *Microporous and Mesoporous Materials* 231:154-162. doi: http://dx.doi.org/10.1016/j.micromeso.2016.05.027.

Tari, Nesa Esmaeilian, Azadeh Tadjarodi, Javad Tamnanloo, and Shohreh Fatemi. 2016b. "Synthesis and property modification of MCM-41 composited with Cu(BDC) MOF for improvement of CO2 adsorption Selectivity." *Journal of CO2 Utilization* 14:126-134. doi: http://dx.doi.org/10.1016/j.jcou.2016.04.008.

Thomas, W.J., and B.D. Crittenden. 1998. *Adsorption Technology and Design*: Butterworth-Heinemann.

Todd, Richard S., and Paul A. Webley. 2006. "Mass-transfer models for rapid pressure swing adsorption simulation." *AIChE Journal* 52 (9):3126-3145. doi: 10.1002/aic.10948.

Tranchemontagne, David J., Joseph R. Hunt, and Omar M. Yaghi. 2008. "Room temperature synthesis of metal-organic frameworks: MOF-5, MOF-74, MOF-177, MOF-199, and IRMOF-0." *Tetrahedron* 64 (36):8553-8557. doi: http://dx.doi.org/10.1016/j.tet.2008.06.036.

Trung, Thuy Khuong, Philippe Trens, Nathalie Tanchoux, Sandrine Bourrelly, Philip L. Llewellyn, Sandra Loera-Serna, Christian Serre, Thierry Loiseau, François Fajula, and Gérard Férey. 2008. "Hydrocarbon Adsorption in the Flexible Metal Organic Frameworks MIL-53(Al, Cr)." *Journal of the American Chemical Society* 130 (50):16926-16932. doi: 10.1021/ja8039579.

Tykodi, R. J. 1958. "Adsorption at low coverage." *Transactions of the Faraday Society* 54 (0):918-921. doi: 10.1039/TF9585400918.

Wang, Bin, Xiu-Liang Lv, Dawei Feng, Lin-Hua Xie, Jian Zhang, Ming Li, Yabo Xie, Jian-Rong Li, and Hong-Cai Zhou. 2016. "Highly Stable Zr(IV)-Based Metal–Organic Frameworks for the Detection and Removal of Antibiotics and Organic Explosives in Water." *Journal of the American Chemical Society* 138 (19):6204-6216. doi: 10.1021/jacs.6b01663.

Wang, Lu, Yuzhen Han, Xiao Feng, Junwen Zhou, Pengfei Qi, and Bo Wang. 2016. "Metal–organic frameworks for energy storage: Batteries and supercapacitors." *Coordination Chemistry Reviews* 307, Part 2:361-381. doi: http://dx.doi.org/10.1016/j.ccr.2015.09.002.

Wang, Qiang, Jizhong Luo, Ziyi Zhong, and Armando Borgna. 2011. "CO2 capture by solid adsorbents and their applications: current status and new trends." *Energy & Environmental Science* 4 (1):42-55. doi: 10.1039/C0EE00064G.

Wiersum, Andrew D., Jong-San Chang, Christian Serre, and Philip L. Llewellyn. 2013. "An Adsorbent Performance Indicator as a First Step Evaluation of Novel Sorbents for Gas Separations: Application to Metal–Organic Frameworks." *Langmuir* 29 (10):3301-3309. doi: 10.1021/la3044329.

Wilcox, J. 2012. *Carbon Capture*: Springer New York.

Winter, Carl-Jochen. 2009. "Hydrogen energy — Abundant, efficient, clean: A debate over the energy-system-of-change." *International Journal of Hydrogen Energy* 34 (14, Supplement 1):S1-S52. doi: http://dx.doi.org/10.1016/j.ijhydene.2009.05.063.

Wu, Hui, Wei Zhou, and Taner Yildirim. 2009. "High-Capacity Methane Storage in Metal−Organic Frameworks M2(dhtp): The Important Role of Open Metal Sites." *Journal of the American Chemical Society* 131 (13):4995-5000. doi: 10.1021/ja900258t.

Wu, Xiaofei, Bin Yuan, Zongbi Bao, and Shuguang Deng. 2014. "Adsorption of carbon dioxide, methane and nitrogen on an ultramicroporous copper metal–organic framework." *Journal of Colloid and Interface Science* 430:78-84. doi: http://dx.doi.org/10.1016/j.jcis.2014.05.021.

Yaghi, Omar M., Hailian Li, Charles Davis, David Richardson, and Thomas L. Groy. 1998. "Synthetic Strategies, Structure Patterns, and Emerging Properties in the Chemistry of Modular Porous Solids." *Accounts of Chemical Research* 31 (8):474-484. doi: 10.1021/ar970151f.

Yan, Yong, Xiang Lin, Sihai Yang, Alexander J. Blake, Anne Dailly, Neil R. Champness, Peter Hubberstey, and Martin Schroder. 2009. "Exceptionally high H2storage by a metal-organic polyhedral framework." *Chemical Communications* (9):1025-1027. doi: 10.1039/B900013E.

Yang, Huimin, Haiyan Du, Liqin Zhang, Zhenhai Liang, and Wanjie Li. 2015. "Electrosynthesis and Electrochemical Mechanism of Zn-Based Metal-Organic Frameworks." *International Journal of Electrochemical Science* 10 (2).

Yang, Jaeyoung, Jang-Hoon Lee, Chang-Ha Lee, and Hanju Lee. 1997. "Hydrogen separation by two-bed PSA process." In *Studies in Surface Science and Catalysis*, edited by Son-Ki Ihm Hakze Chon and Uh Young Sun, 1883-1890. Elsevier.

Yang, Jiangfeng, Qiuhong Yu, Qiang Zhao, Jianming Liang, Jinxiang Dong, and Jinping Li. 2012. "Adsorption CO2, CH4 and N2 on two different spacing flexible layer MOFs." *Microporous and Mesoporous Materials* 161:154-159. doi: http://dx.doi.org/10.1016/j.micromeso.2012.01.008.

Yang, R.T. 1997. *Gas Separation by Adsorption Processes*: Imperial College Press.

Yang, Ying, Chatcharin Sitprasert, Thomas E. Rufford, Lei Ge, Pradeep Shukla, Shaobin Wang, Victor Rudolph, and Zhonghua Zhu. 2015. "An experimental and simulation study of binary adsorption in metal–organic frameworks." *Separation and Purification Technology* 146:136-142. doi: http://dx.doi.org/10.1016/j.seppur.2015.03.041.

Zhang, Guoqi, Guoqiang Yang, and Jin Shi Ma. 2006. "Versatile Framework Solids Constructed from Divalent Transition Metals and Citric Acid: Syntheses, Crystal Structures, and Thermal Behaviors." *Crystal Growth & Design* 6 (2):375-381. doi: 10.1021/cg0503245.

Zhang, Si Yang, Orhan Talu, and David T. Hayhurst. 1991. "High-pressure adsorption of methane in zeolites NaX, MgX, CaX, SrX and BaX." *The Journal of Physical Chemistry* 95 (4):1722-1726. doi: 10.1021/j100157a044.

Zhang, Zhangjing, Shengchang Xiang, Yu-Sheng Chen, Shengqian Ma, Yongwoo Lee, Thomas Phely-Bobin, and Banglin Chen. 2010. "A Robust Highly Interpenetrated Metal−Organic Framework Constructed from Pentanuclear Clusters for Selective Sorption of Gas Molecules." *Inorganic Chemistry* 49 (18):8444-8448. doi: 10.1021/ic1010083.

Zhao, Yang, Zhongxin Song, Xia Li, Qian Sun, Niancai Cheng, Stephen Lawes, and Xueliang Sun. 2016. "Metal organic frameworks for energy storage and conversion." *Energy Storage Materials* 2:35-62. doi: http://dx.doi.org/10.1016/j.ensm.2015.11.005.

Zou, Caineng, Qun Zhao, Guosheng Zhang, and Bo Xiong. 2016. "Energy revolution: From a fossil energy era to a new energy era." *Natural Gas Industry B* 3 (1):1-11. doi: http://dx.doi.org/10.1016/j.ngib.2016.02.001.

APPENDIX A
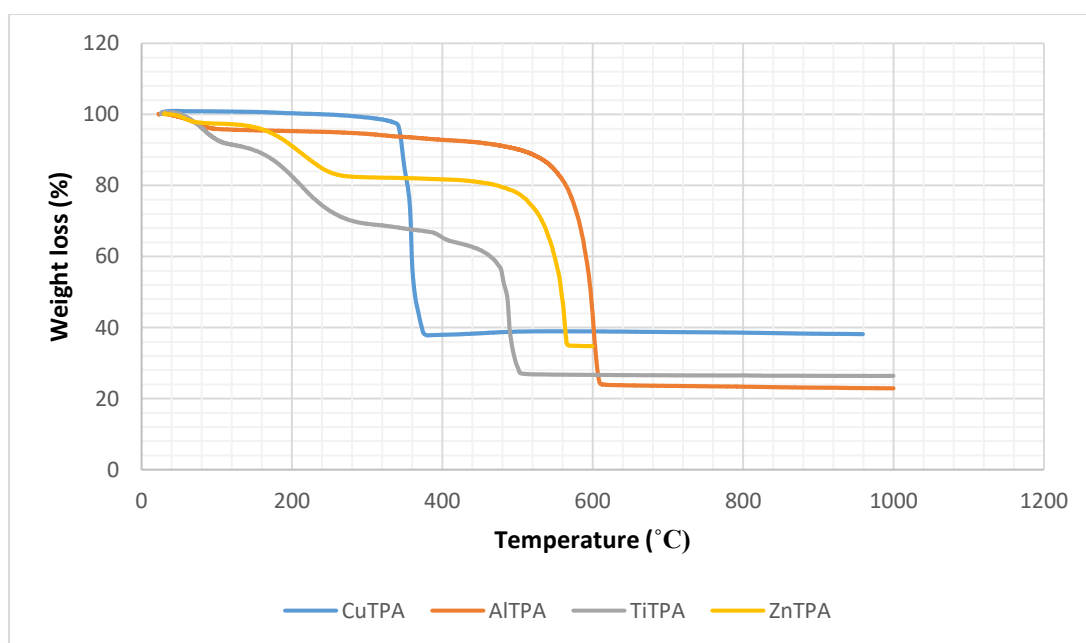
DETAILS ABOUT EXPERIMENTAL ADSORPTION STUDIES

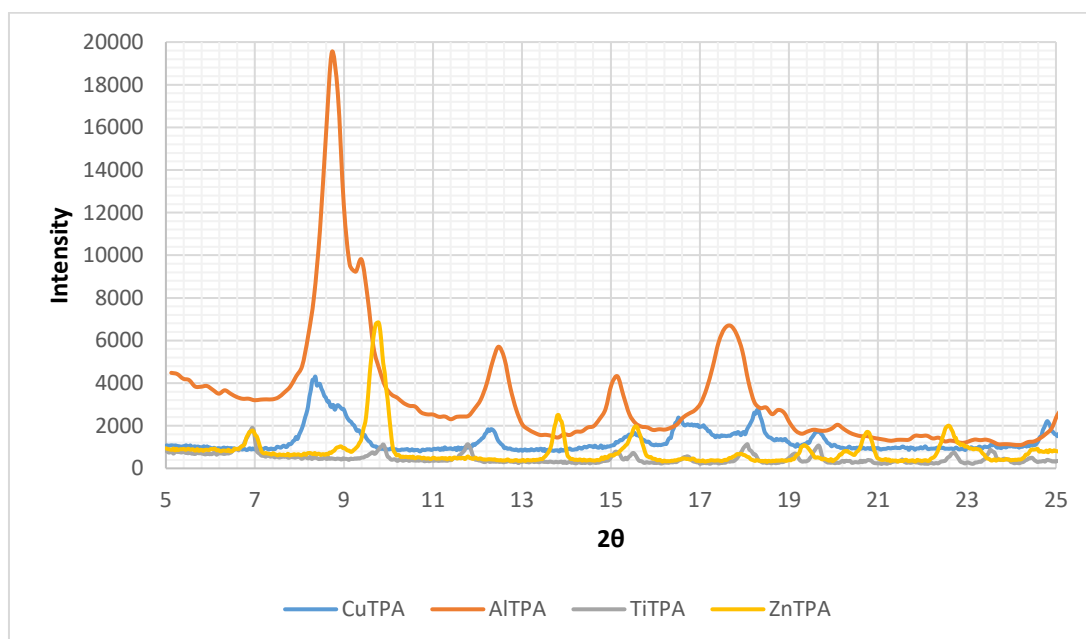Figure A.1. Thermogravimetric profiles of the CuTPA, AlTPA, TiTPA and ZnTPA.

Figure A.2. X-ray diffractometer patterns of CuTPA, AlTPA, TiTPA and ZnTPA
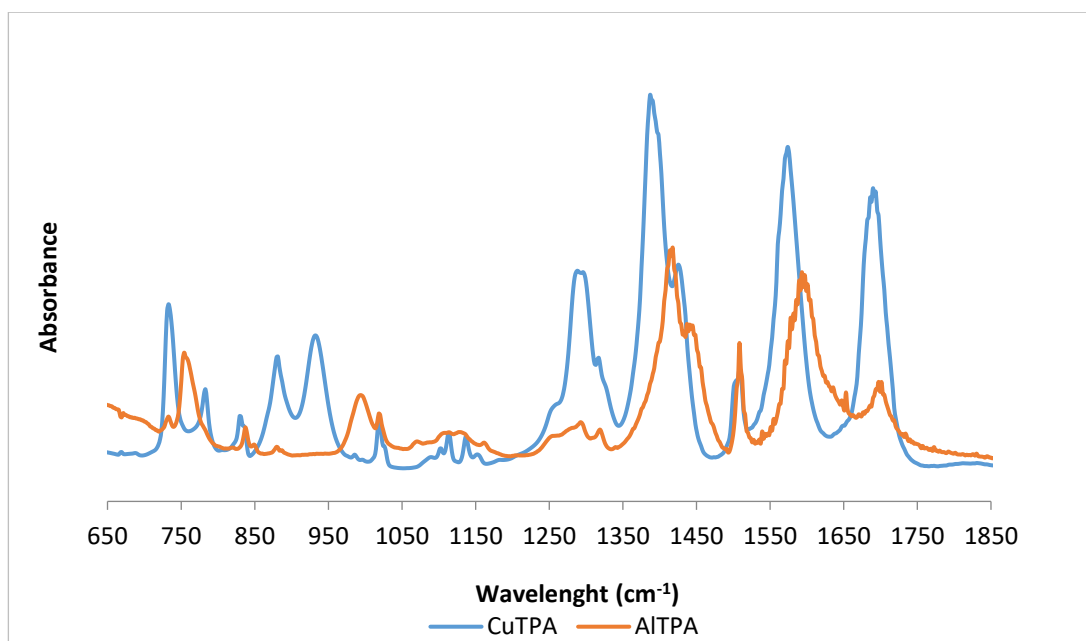
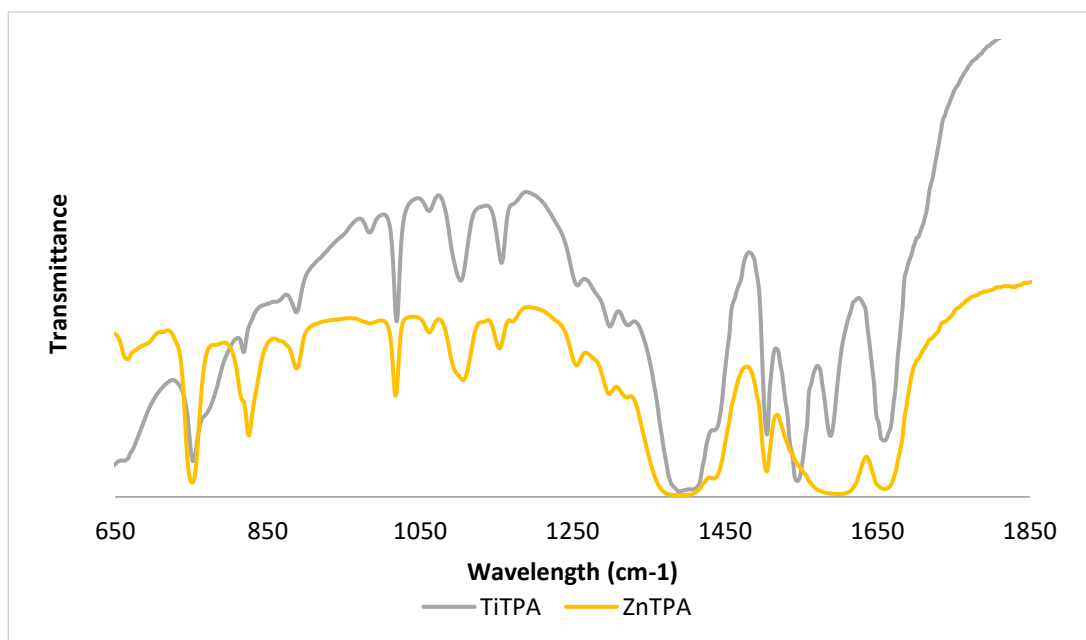Figure A.3. Infrared spectra of CuTPA and AlTPA.

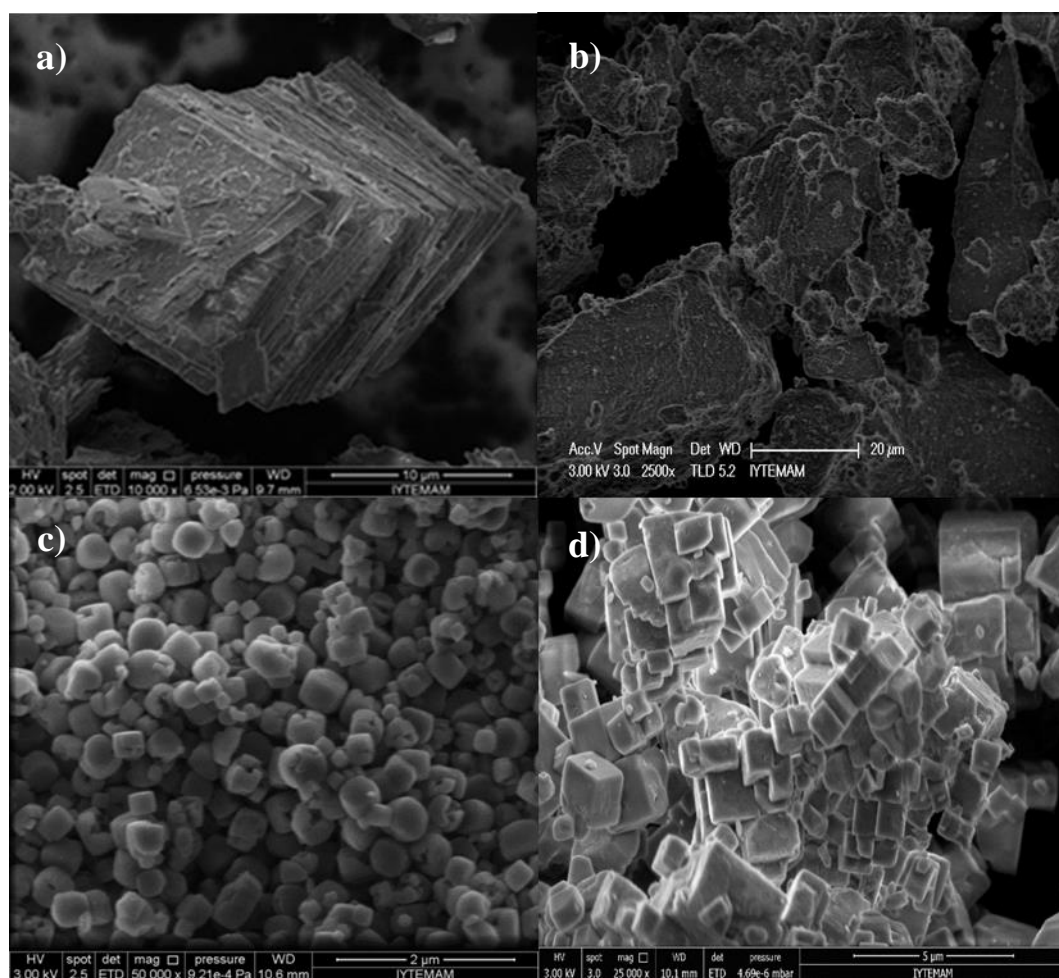Figure A.4. Infrared spectra of TiTPA and ZnTPA

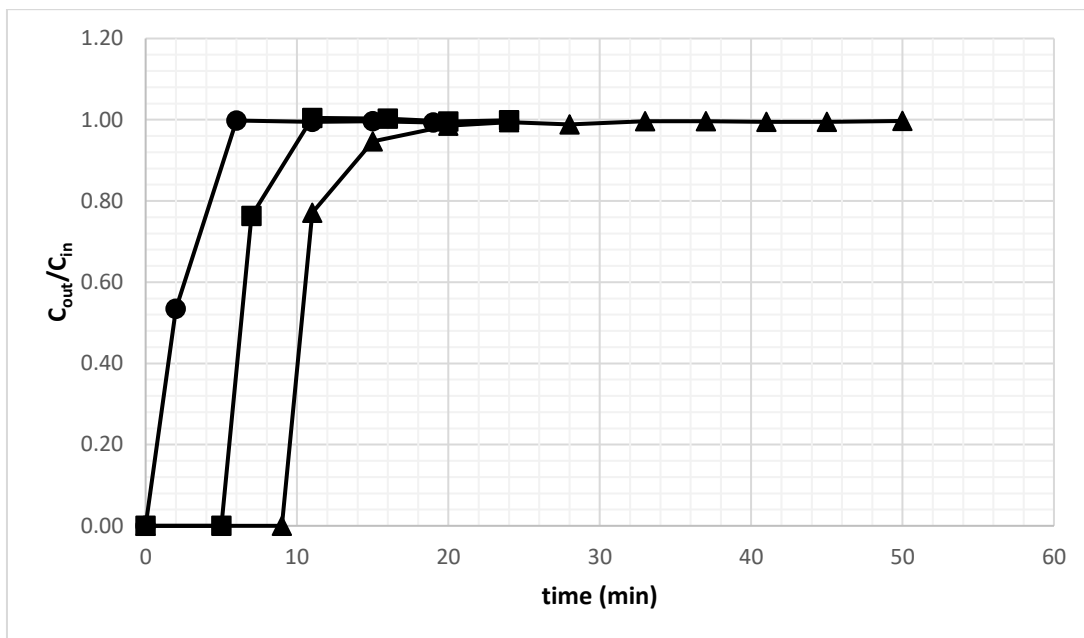Figure A.5. SEM images of a) CuTPA, b) AlTPA, c) TiTPA and d) ZnTPA.

Figure A.6. Effect of pressure on CO_2 adsorption breakthrough curves over CuTPA (Total CO_2/H_2 flow rate: 30 mL/min; Bed pressures: 1bar (●), 5bar (■) and 10 bar (▲))
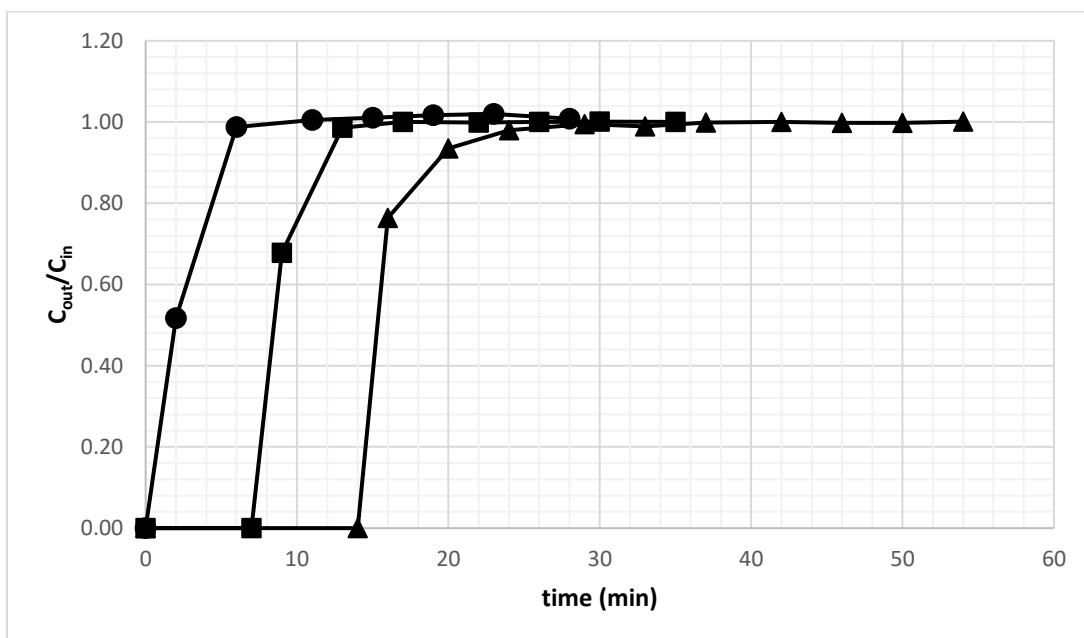

Figure A.7. Effect of pressure on CO_2 adsorption breakthrough curves over CuTPA (Total CO_2/H_2 flow rate: 20 mL/min; Bed pressures: 1bar (●), 5bar (■) and 10 bar (▲))
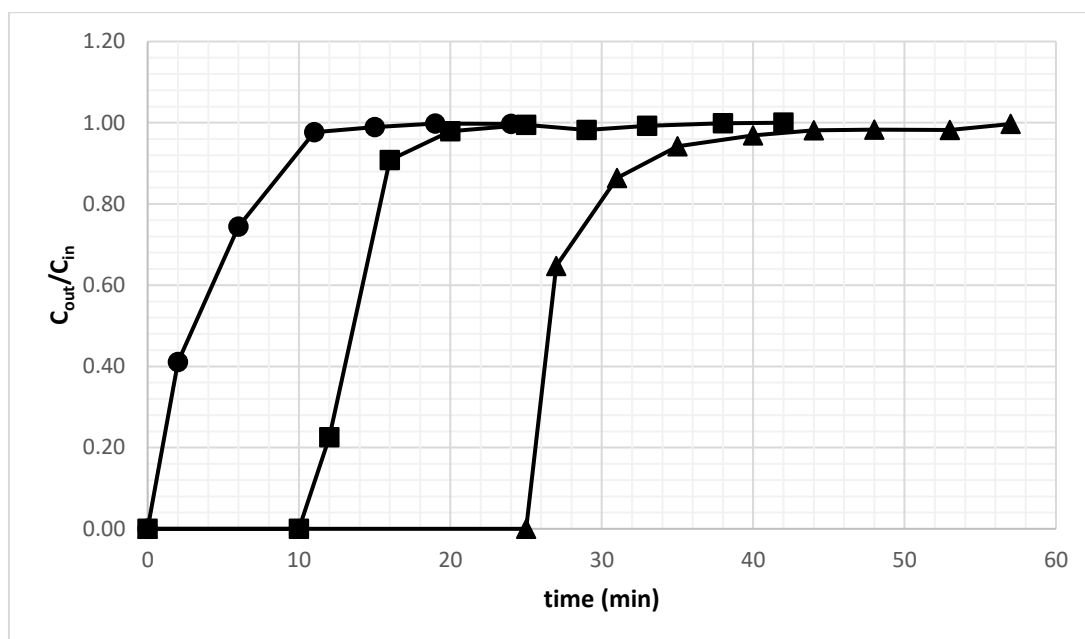
Figure A.8. Effect of pressure on CO_2 adsorption breakthrough curves over CuTPA (Total CO_2/H_2 flow rate: 10 mL/min; Bed pressures: 1bar (●), 5bar (■) and 10 bar (▲))
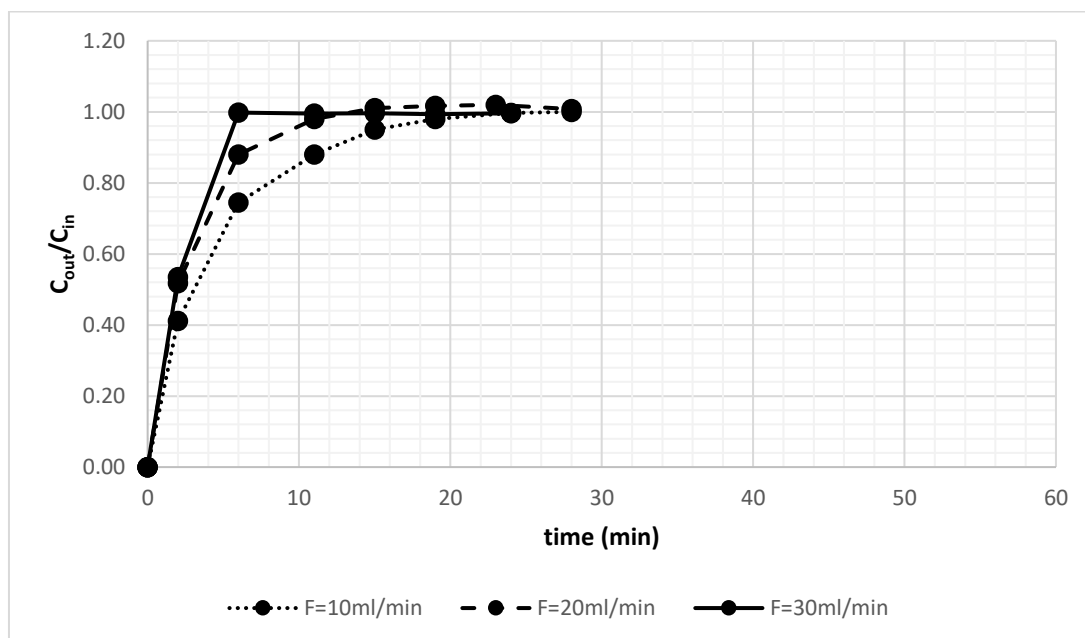

Figure A.9. Effect of feed flow rate on CO_2 adsorption breakthrough curves over CuTPA (Bed pressure: 1 bar; Total CO_2/H_2 flow rate: 30 mL/min (——), 20 mL/min (-----) and 10 mL/min (·········))
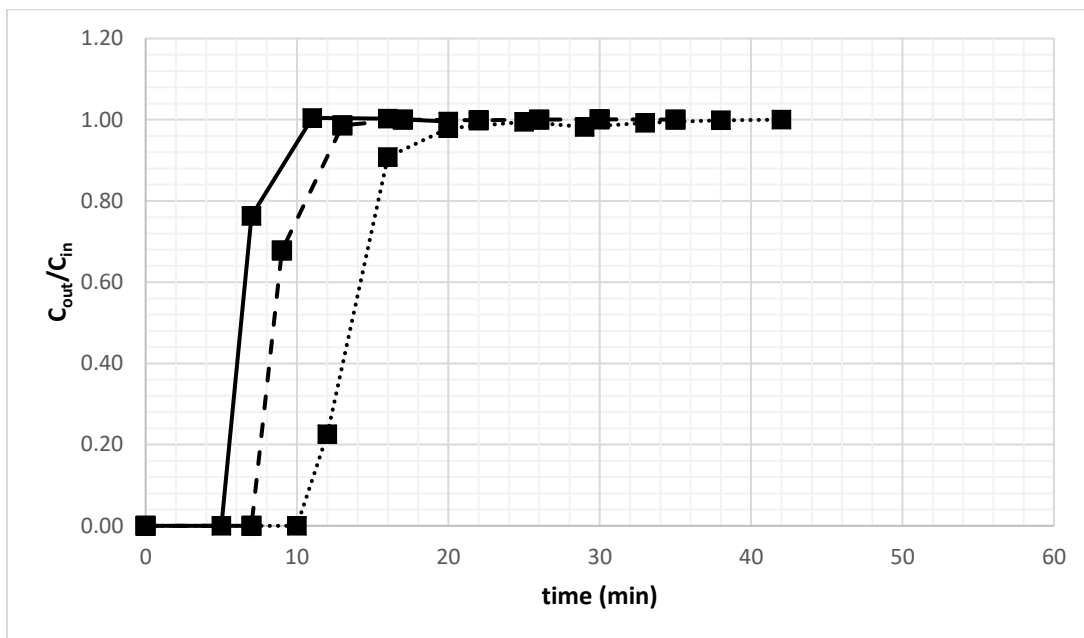
Figure A.10. Effect of feed flow rate on CO_2 adsorption breakthrough curves over CuTPA (Bed pressure: 5 bar; Total CO_2/H_2 flow rate: 30 mL/min (———), 20 mL/min (−−−−) and 10 mL/min (··········))
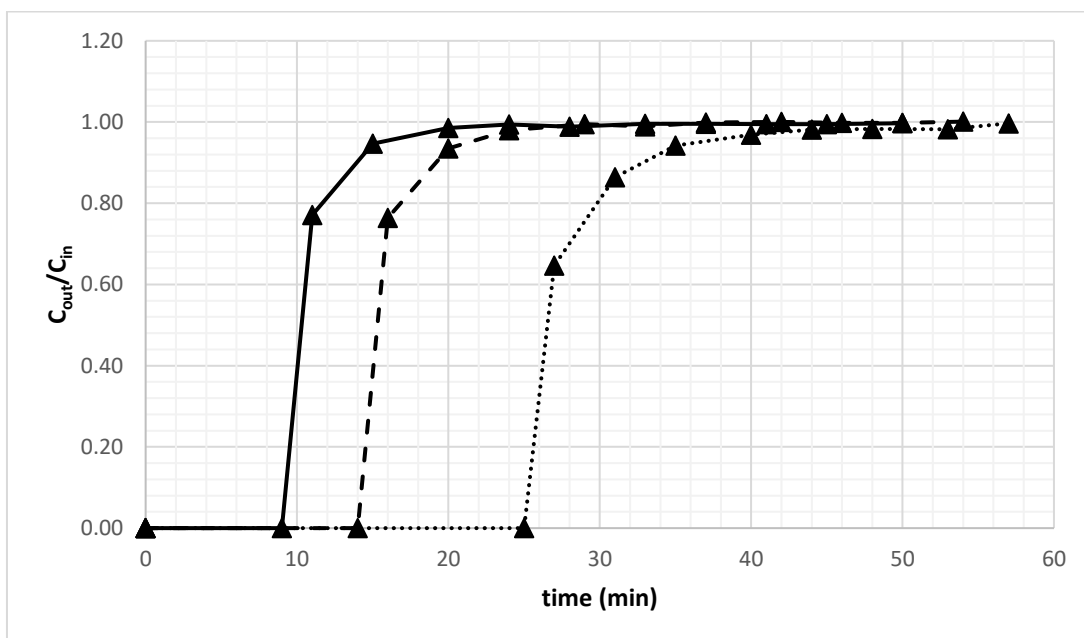

Figure A.11. Effect of feed flow rate on CO_2 adsorption breakthrough curves over CuTPA (Bed pressure: 10 bar; Total CO_2/H_2 flow rate: 30 mL/min (———), 20 mL/min (−−−−) and 10 mL/min (··········))

Figure A.12. CO_2 desorption curves over CuTPA (He purge flow rate: 30 mL/min (——),
20 mL/min (-----) and 10 mL/min (·······); Bed pressures: 1bar (●), 5bar
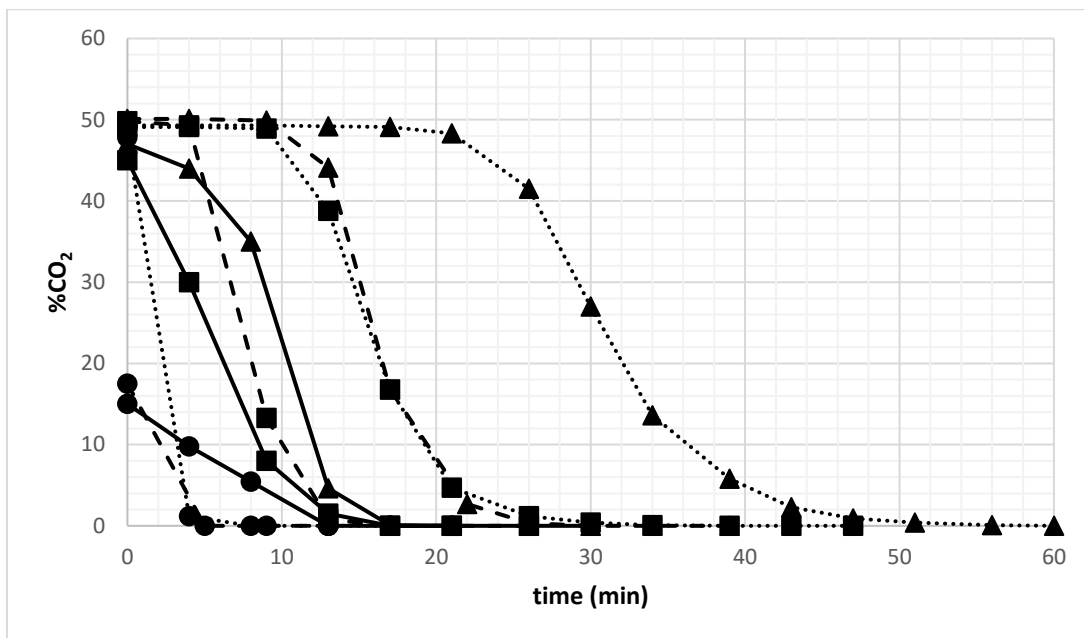(■) and 10 bar (▲))

Figure A.13. CO desorption curves over CuTPA (He purge flow rate: 30 mL/min (——),
20 mL/min (-----) and 10 mL/min (·······); Bed pressures: 1bar (●), 5bar (■)
and 10 bar (▲))
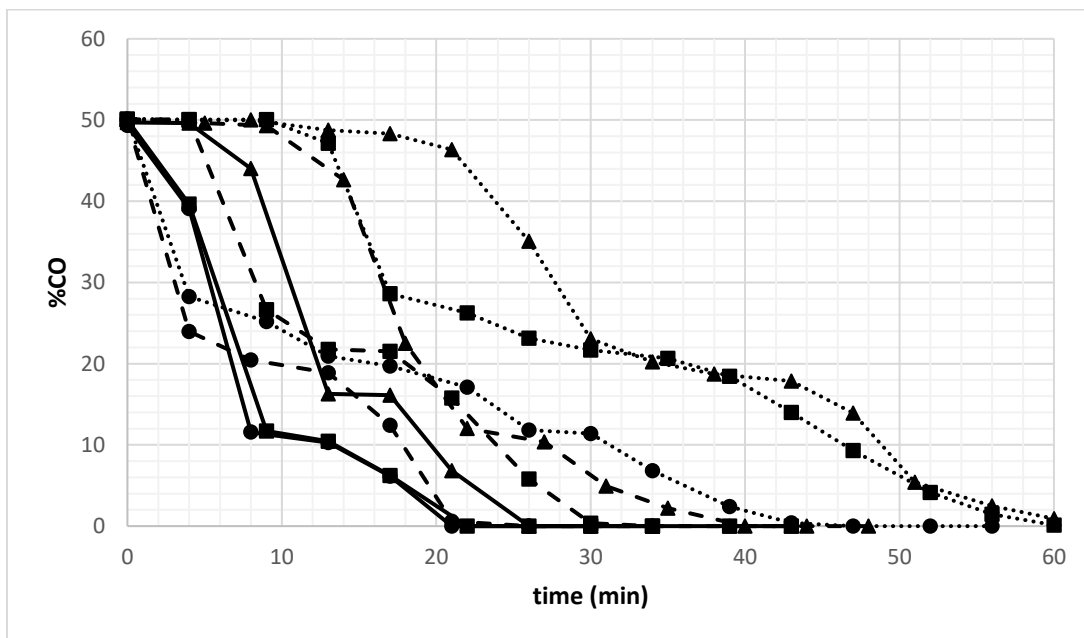
Table A.1. Ideal and real selectivities of CuTPA for CO_2 over CH_4 at 303 K.

Total flow rate (mL/min)	Pressure (bar)	Ideal Selectivity ($S_{CO2/CH4}$)	Real Selectivity ($S_{CO2/CH4}$)
10	1	1.1	3.1
	5	1.3	2.2
	10	1.2	1.7
20	1	1.4	1.7
	5	1.3	1.1
	10	1.1	1.1
30	1	2.3	1.2
	5	1.3	1.1
	10	1.1	1.1

Figure A.14. Molar percentages of CH_4 and He effluent over CuTPA at 303 K (Total CH_4/He flow rate: 20 mL/min, CH_4: ● and H_2:▲; Bed pressures: 1bar (——), 3bar (-----), 5bar (·········), 8bar (— · —) and 10bar (— —))
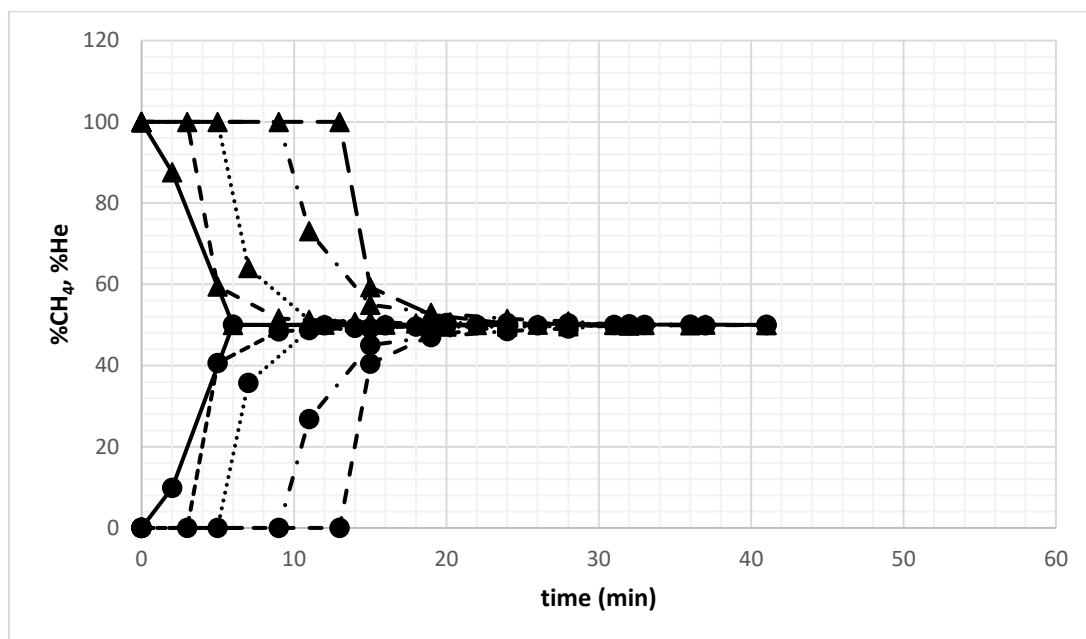
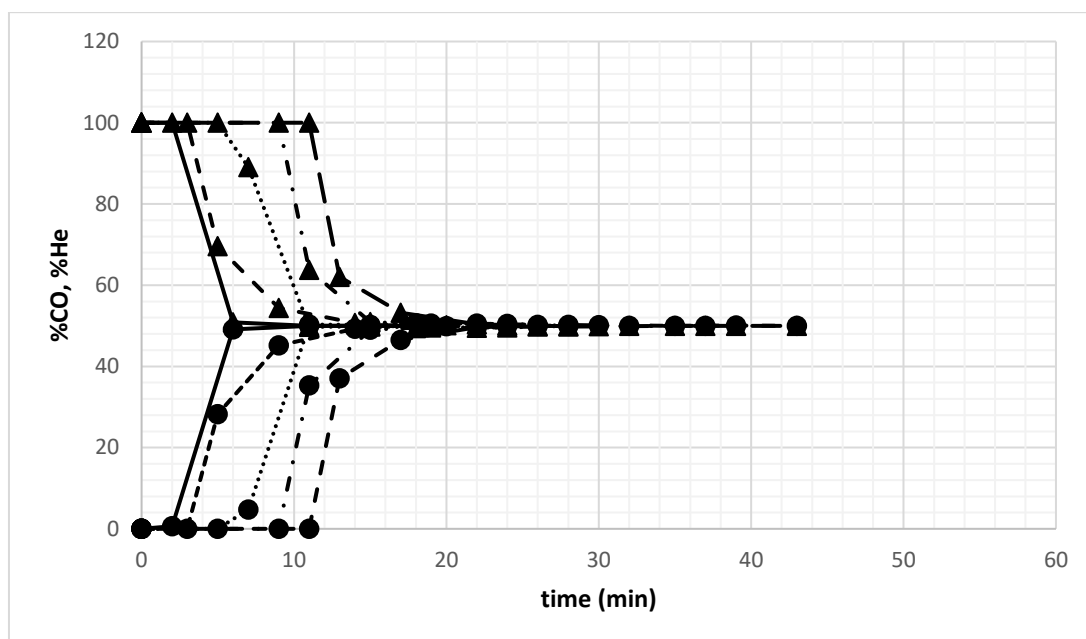Figure A.15. Molar percentages of CO and He effluent over CuTPA at 303 K (Total CO/He flow rate: 20 mL/min, CO: ● and H₂: ▲, Bed pressures: 1bar (———), 3bar (-----), 5bar (··········), 8bar (— · —) and 10bar (— —))
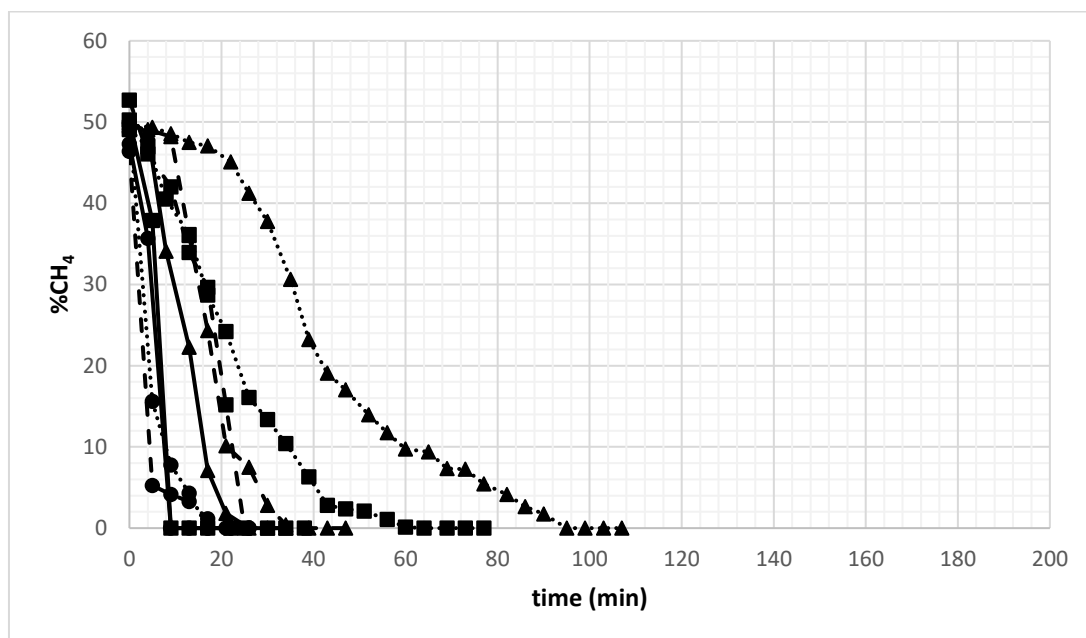

Figure A.16. CH₄ desorption curves over AlTPA (He purge flow rate: 30 mL/min (———), 20 mL/min (-----) and 10 mL/min (··········); Bed pressures: 1bar (●), 5bar (■) and 10 bar (▲))
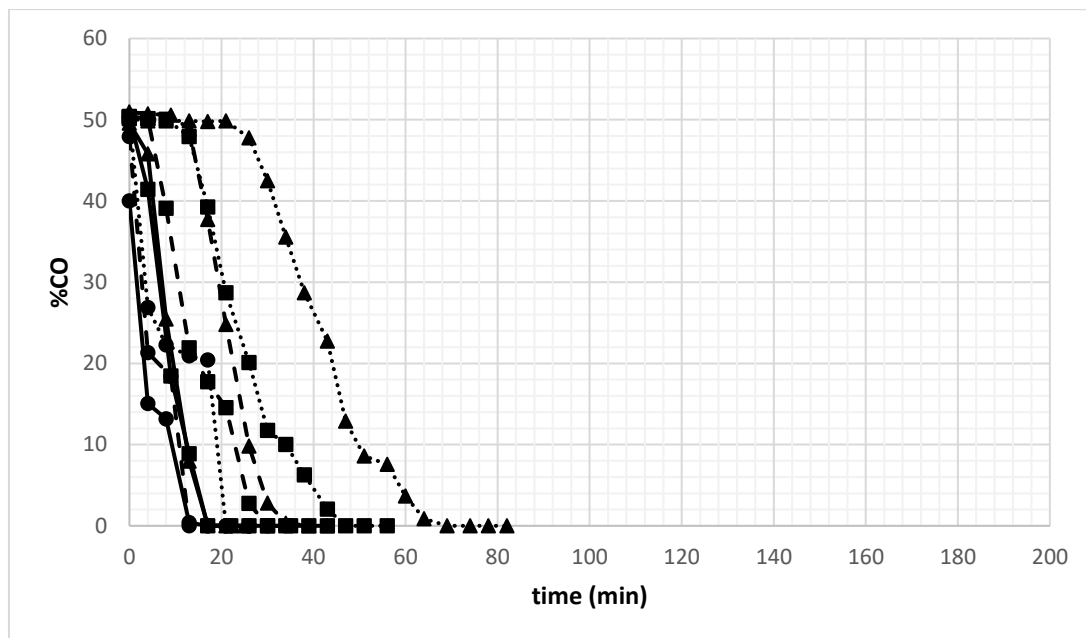
Figure A.17. CO desorption curves over AlTPA (He purge flow rate: 30 mL/min (——),
20 mL/min (- - - -) and 10 mL/min (·········); Bed pressures: 1bar ($\bullet$), 5bar
($\blacksquare$) and 10 bar ($\blacktriangle$))

Table A.2. The dynamic parameters of AlTPA packed bed and calculated adsorbed
amount of CO_2 from experimental breakthrough curves at different bed
operating conditions

Total flow rate (mL/min)	Pressure (bar)	t_{pres} (min)	t_{break} (min)	t_{sat} (min)	t_{des} (min)	t_{cycle} (min)	H_{UNB} (cm)	τ_{CO2} (min)	q_{CO2} (mmolCO$_2$/g)
10	**1**	0	11	28	38	66	6.7	14	0.80
	5	17	36	66	136	219	4.8	44	2.56
	10	37	60	116	245	398	5.2	73	4.19
20	**1**	0	6	23	21	44	8.0	8	1.14
	5	12	14	44	78	134	5.8	25	3.36
	10	20	32	88	98	206	6.5	41	5.47
30	**1**	0	2	19	13	32	9.3	5	1.19
	5	6	12	34	51	91	7.1	16	3.41
	10	14	21	42	84	140	5.5	27	5.54

Table A.3. The dynamic parameters of AlTPA packed bed and calculated adsorbed amount of CH_4 from experimental breakthrough curves at different bed operating conditions

Total flow rate (mL/min)	Pressure (bar)	t_{pres} (min)	t_{break} (min)	t_{sat} (min)	t_{des} (min)	t_{cycle} (min)	H_{UNB} (cm)	τ_{CH4} (min)	q_{CH4} (mmolCH$_4$/gAlTPA)
	1	0	0	6	17	23	10.6	6	0.22
10	5	14	14	37	64	115	6.9	18	1.15
	10	30	30	70	95	195	6.4	38	2.14
	1	0	0	6	22	28	10.6	2	0.41
20	5	9	9	32	25	66	7.8	14	1.62
	10	18	18	37	39	94	5.7	23	2.99
	1	0	0	6	9	15	10.6	2	0.45
30	5	6	6	12	9	27	5.5	8	1.73
	10	12	12	27	26	65	5.4	16	3.16

Table A.4. The dynamic parameters of AlTPA packed bed and calculated adsorbed amount of CO from experimental breakthrough curves at different bed operating conditions

Total flow rate (mL/min)	Pressure (bar)	t_{pres} (min)	t_{break} (min)	t_{sat} (min)	t_{des} (min)	t_{cycle} (min)	H_{UNB} (cm)	τ_{CO} (min)	q_{CO} (mmolCO/gAlTPA)
	1	0	0	6	21	27	10.4	3	0.14
10	5	12	12	23	47	82	5.4	15	0.75
	10	25	25	53	74	152	5.3	28	1.46
	1	0	0	6	13	19	10.6	2	0.22
20	5	7	7	18	30	55	6.7	9	1.13
	10	15	15	30	39	84	5.6	18	2.21
	1	0	0	6	17	23	10.6	2	0.31
30	5	5	5	12	17	34	6.4	6	1.26
	10	11	11	26	21	58	6.4	13	2.59

Table A.5. Langmuir and virial model parameters of pure CO_2, CH_4 and CO components on AlTPA at 303 K (Total feed flow: 30mL/min, bed pressure: 10 bar)

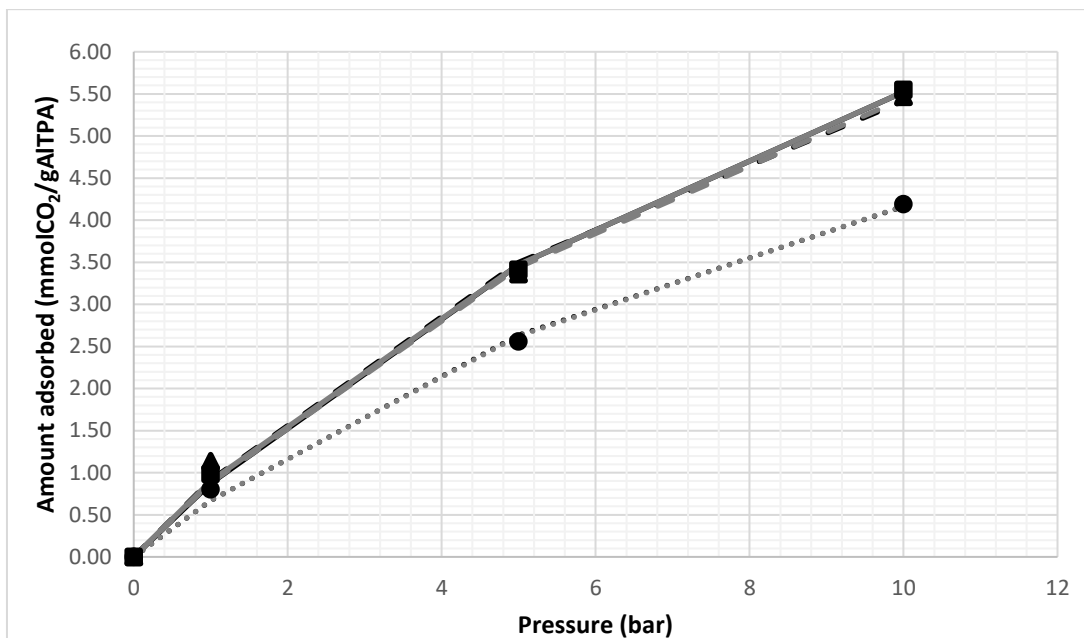|	Langmuir Model Parameters		
	CO_2	CH_4	CO
q_m (mmol/g)	13.475	30.08	117.8
$\propto$ (bar^{-1})	0.069	0.012	0.002
R^2	0.998	0.997	0.998
ERRSQ	0.017	0.022	0.0047
	Virial Model Parameters		
	CO_2	CH_4	CO
H (mmol/gbar)	0.754	0.347	0.267
b	0.142	0.009	0.0016
c	0	0	0.0044
R^2	0.999	0.998	0.999
ERRSQ	0.012	0.019	0.006

Figure A.18. Adsorption isotherms of CO_2 on AlTPA at 303 K (Symbols: experimental data at CO_2/H_2 total flow rate of 10 mL/min (●), 20 mL/min (▲) and 30 mL/min (■); black lines: Langmuir model, grey lines: virial model applied for total feed flow rates of 10 mL/min: (·········), 20 mL/min: (‹----›) and 30 mL/min: (———))
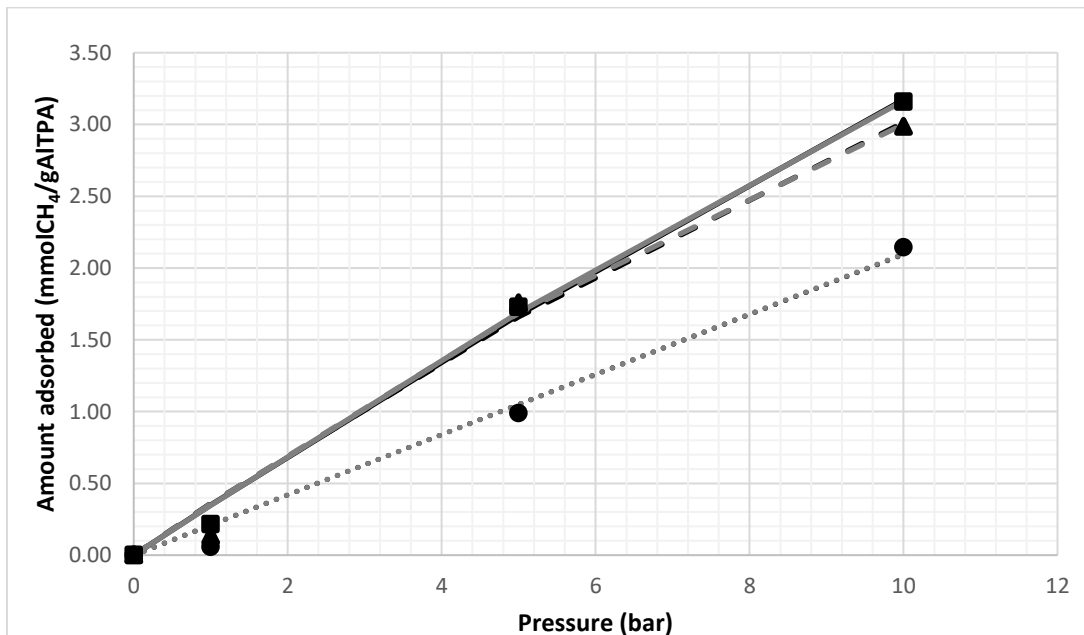

Figure A.19. Adsorption isotherms of CH_4 on AlTPA at 303 K (Symbols: experimental data at CH_4/H_2 total flow rate of 10 mL/min (●), 20 mL/min (▲) and 30 mL/min (■); black lines: Langmuir model, grey lines: virial model applied for total feed flow rates of 10 mL/min: (·········), 20 mL/min: (‹----›) and 30 mL/min: (———))
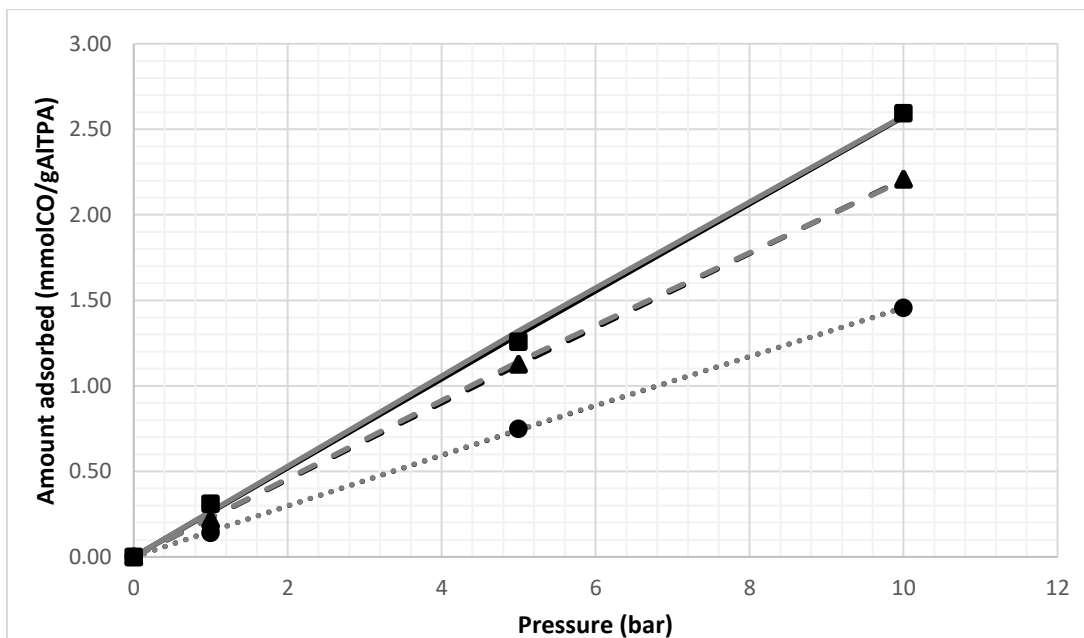
Figure A.20. Adsorption isotherms of CO on AlTPA at 303 K (Symbols: experimental data at CO/H$_2$ total flow rate of 10 mL/min (●), 20 mL/min (▲) and 30 mL/min (■); black lines: Langmuir model, grey lines: virial model applied for total feed flow rates of 10 mL/min (··········), 20 mL/min: (‒ ‒ ‒ ‒) and 30 mL/min: (————))
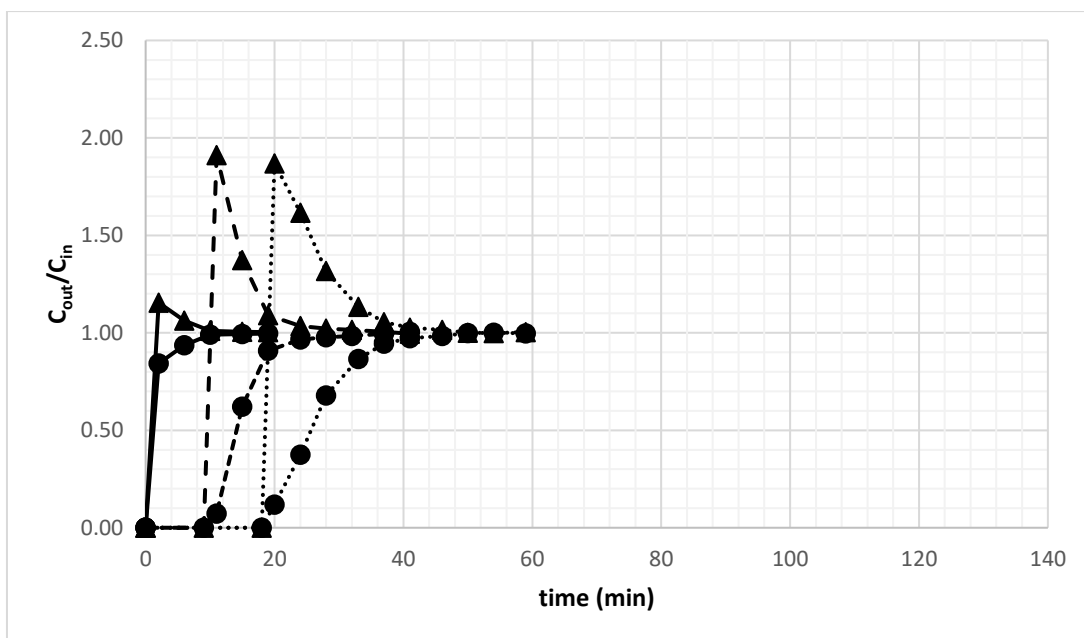

Figure A.21. Effect of pressure on CO$_2$ and CH$_4$ adsorption breakthrough curves over AlTPA (Total CO$_2$/CH$_4$ flow rate: 30 mL/min; CO$_2$: ● and CH$_4$: ▲; Bed pressures: 1bar (————), 5bar (‒ ‒ ‒ ‒) and 10bar (··········))
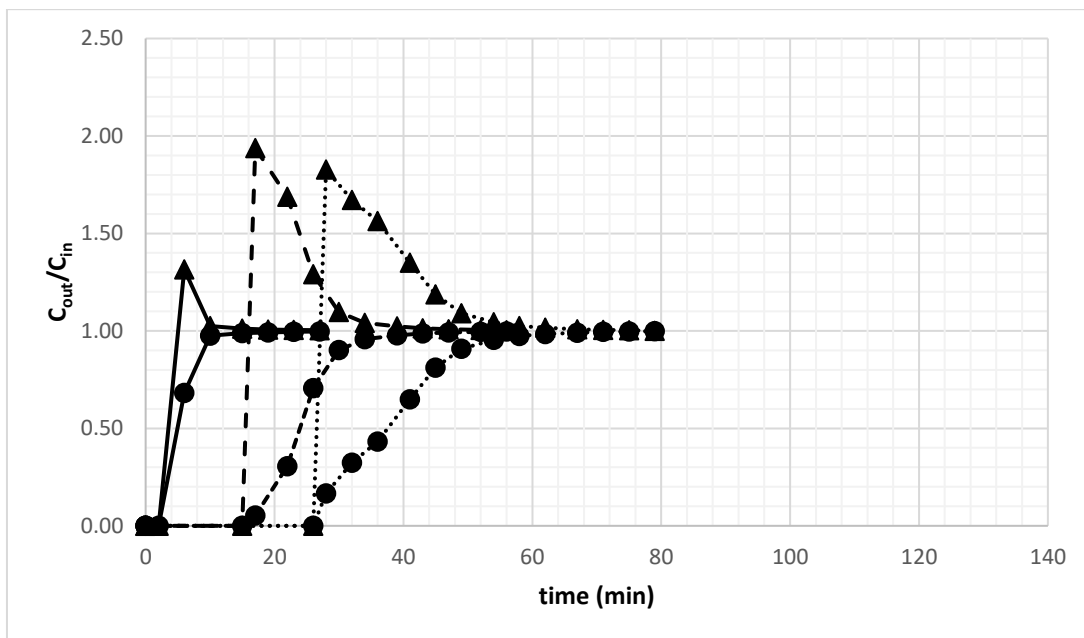
Figure A.22. Effect of pressure on CO_2 and CH_4 adsorption breakthrough curves over AlTPA (Total CO_2/CH_4 flow rate: 20 mL/min; CO_2: ● and CH_4:▲; Bed pressures: 1bar (———), 5bar (- - - -) and 10bar (··········))
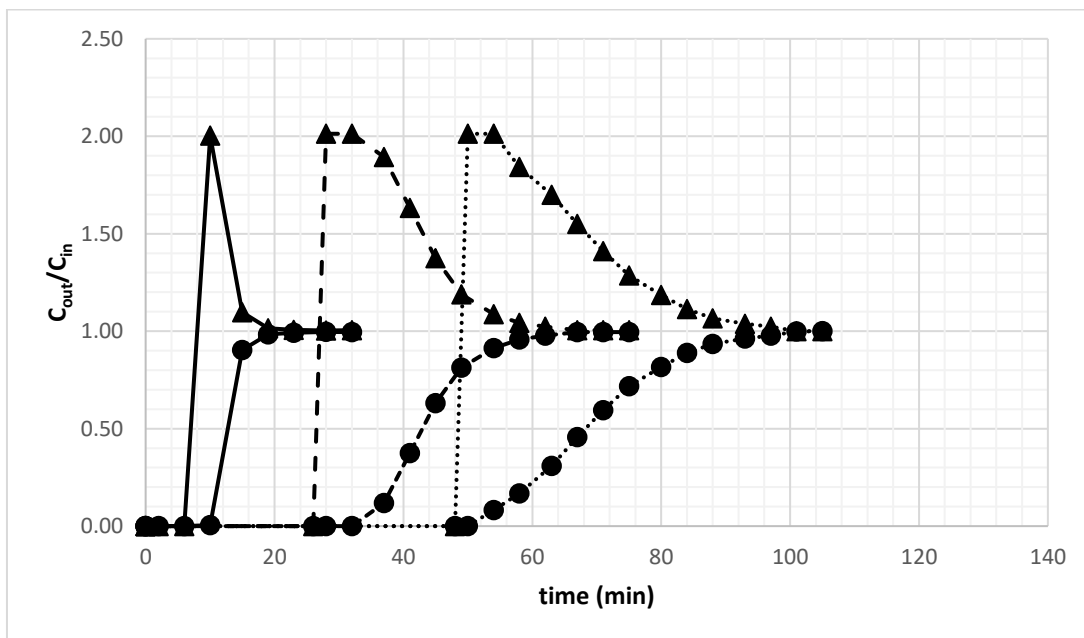

Figure A.23. Effect of pressure on CO_2 and CH_4 adsorption breakthrough curves over AlTPA (Total CO_2/CH_4 flow rate: 10 mL/min; CO_2: ● and CH_4:▲; Bed pressures: 1bar (———), 5bar (- - - -) and 10bar (··········))

Table A.6. Ideal and real selectivities of AlTPA for CO_2 over CH_4 at 303 K.

Total flow rate (mL/min)	Pressure (bar)	Ideal Selectivity ($S_{CO2/CH4}$)	Real Selectivity ($S_{CO2/CH4}$)
	1	3.6	7.5
10	5	2.2	5.2
	10	2.0	3.3
	1	2.8	5.9
20	5	2.1	3.6
	10	1.8	2.5
	1	2.6	3.9
30	5	2.0	2.7
	10	1.8	2.0

Figure A.24. Molar percentages of CO_2 and H_2 effluent over TiTPA at 303 K (Total CO_2/H_2 flow rate: 30 mL/min; CO_2: ● and H_2:▲; Bed pressures: 1bar (———), 5bar (- - - -), 10 bar (·········))

Figure A.25. Molar percentages of CH_4 and H_2 effluent over TiTPA at 303 K (Total CH_4/H_2 flow rate: 30 mL/min; CH_4: ● and H_2:▲; Bed pressures: 1bar (———), 5bar (-----), 10 bar (·········))
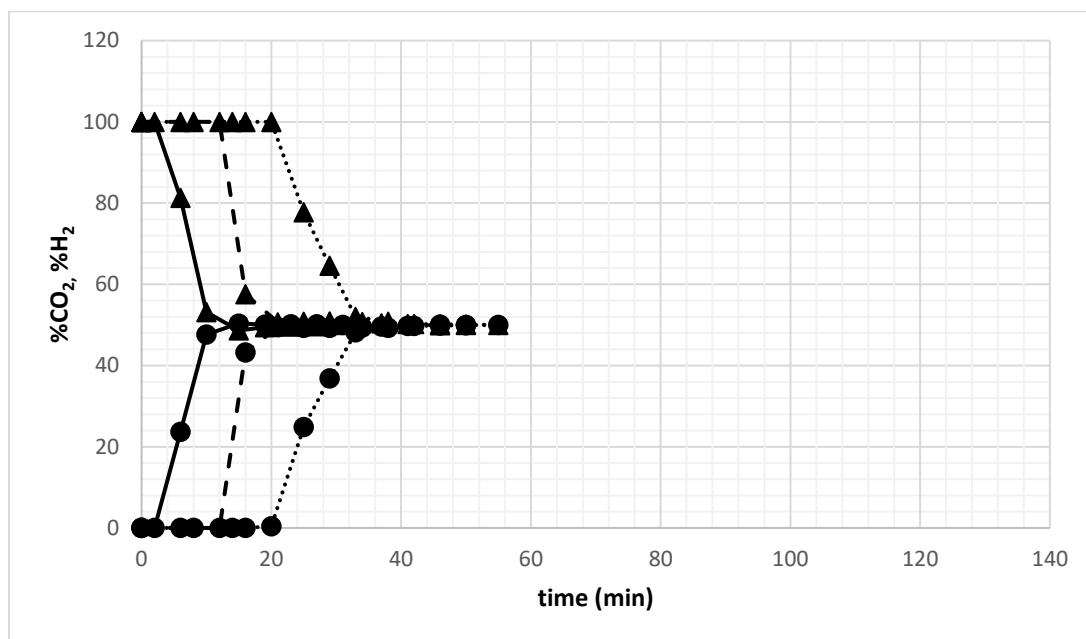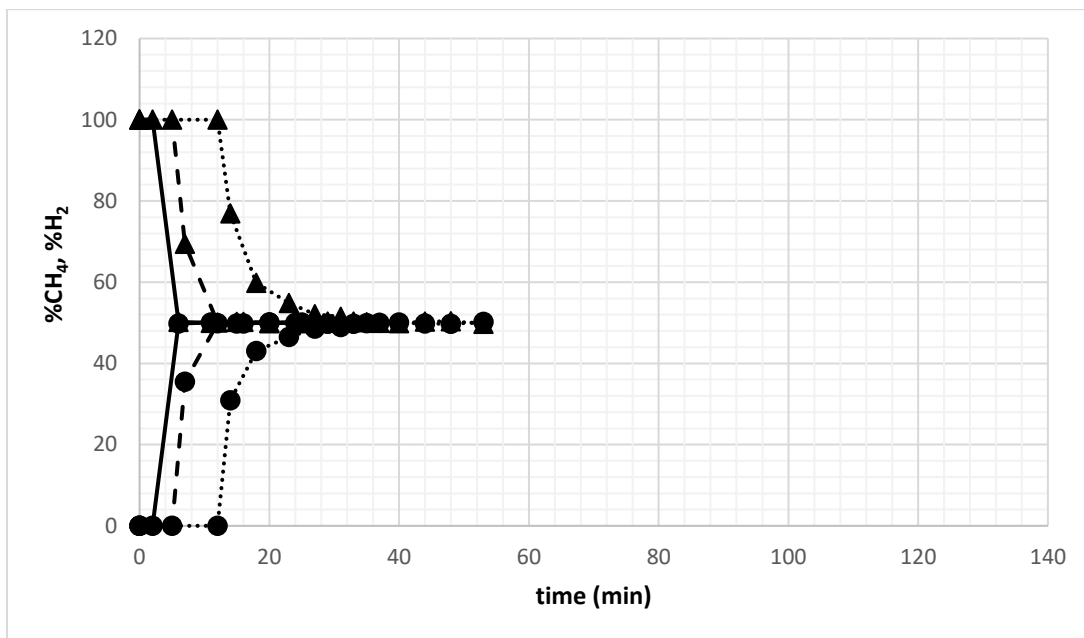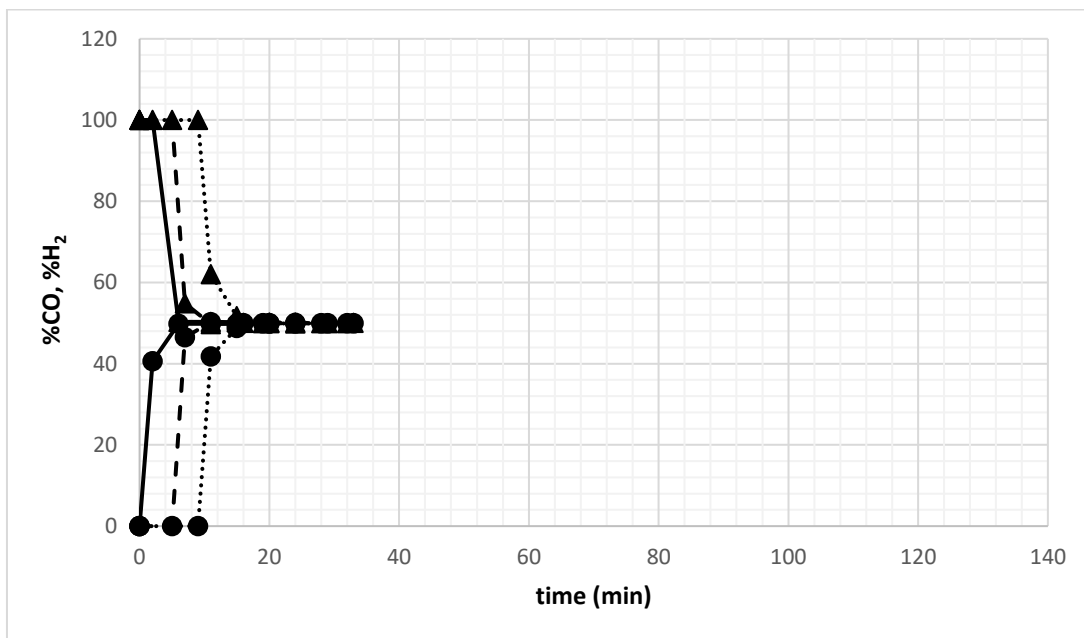

Figure A.26. Molar percentages of CO and H_2 effluent over TiTPA at 303 K (Total CO/H_2 flow rate: 30 mL/min; CO: ● and H_2:▲; Bed pressures: 1bar (———), 5bar (-----), 10 bar (·········))

Figure A.27. CO_2 desorption curves over TiTPA (He purge flow rate: 30 mL/min (———),
20 mL/min (-----) and 10 mL/min (·········); Bed pressures: 1bar (●), 5bar
(■) and 10 bar (▲))

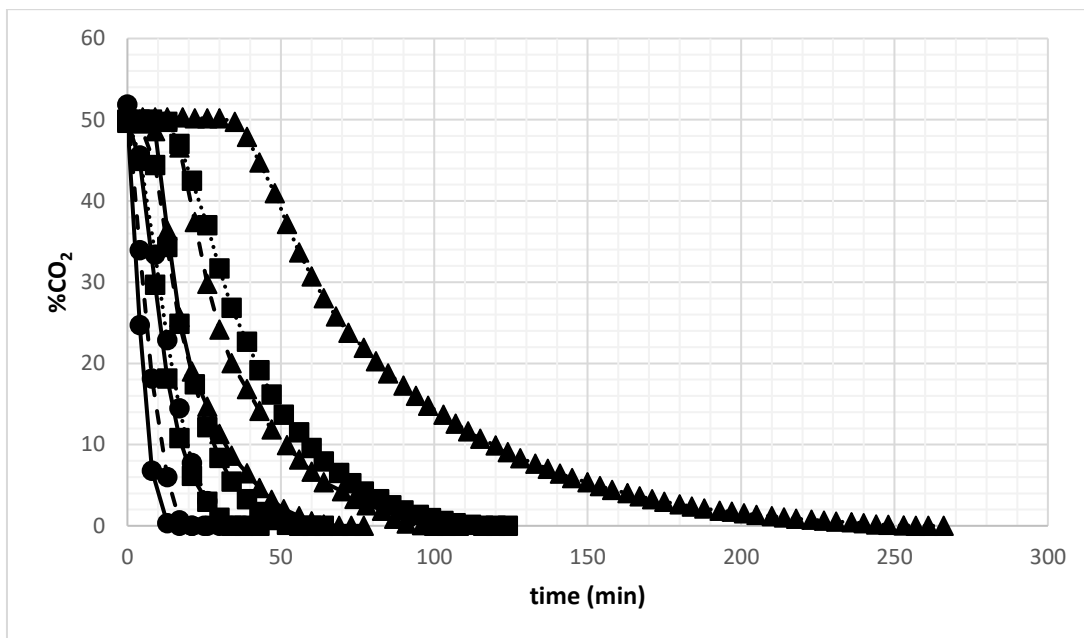Figure A.28. CH_4 desorption curves over TiTPA (He purge flow rate: 30 mL/min (———),
20 mL/min (-----) and 10 mL/min (·········); Bed pressures: 1bar (●), 5bar
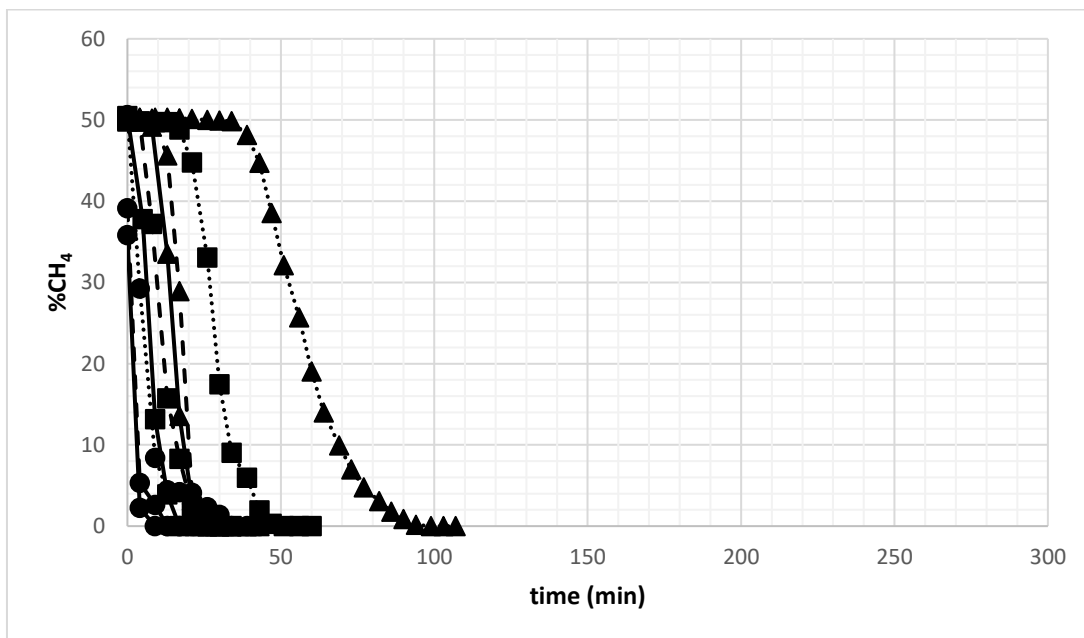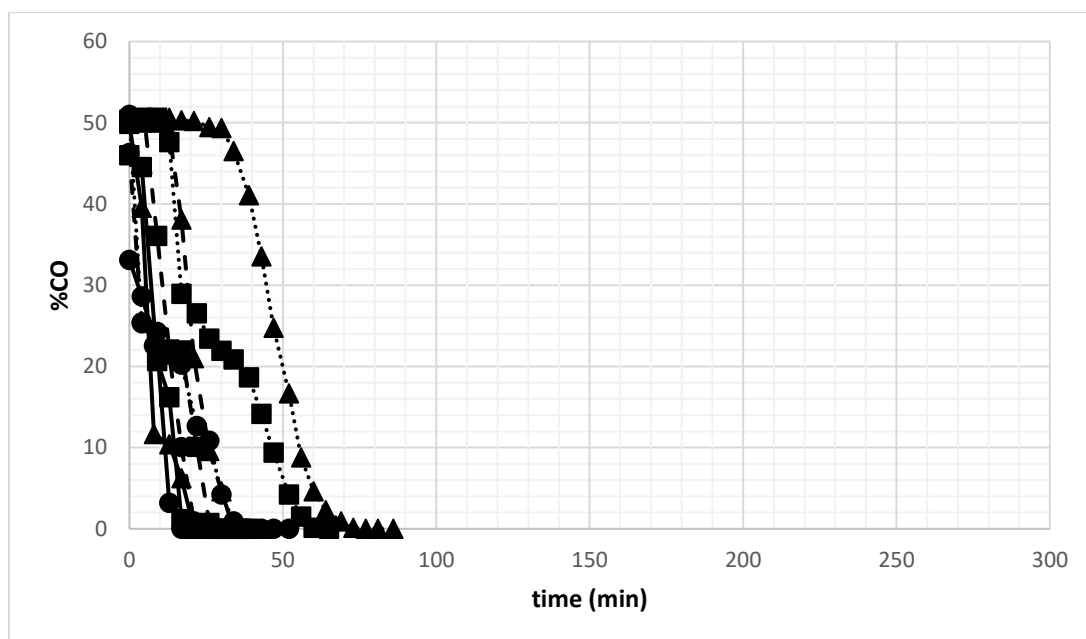(■) and 10 bar (▲))

115

Figure A.29. CO desorption curves over TiTPA (He purge flow rate: 30 mL/min (———),
20 mL/min (- - - -) and 10 mL/min (.........); Bed pressures: 1bar (●), 5bar
(■) and 10 bar (▲))

Table A.7. The dynamic parameters of TiTPA packed bed and calculated adsorbed
amount of CO_2 from experimental breakthrough curves at different bed
operating conditions

Total flow rate (mL/min)	Pressure (bar)	t_{pres} (min)	t_{break} (min)	t_{sat} (min)	t_{des} (min)	t_{cycle} (min)	H_{UNB} (cm)	τ_{CO2} (min)	q_{CO2} (mmolCO2/g)
10	**1**	0	11	23	34	57	5.8	14	0.80
	5	16	35	70	116	202	5.4	43	2.47
	10	46	65	104	207	357	4.0	84	4.71
20	**1**	0	6	23	21	44	8.0	9	1.18
	5	9	15	37	56	102	5.7	22	2.88
	10	23	34	64	100	187	5.2	40	5.17
30	**1**	0	0	15	17	32	10.2	6	1.25
	5	6	12	34	34	74	7.1	15	3.01
	10	14	16	50	69	133	6.6	26	5.20

Table A.8. The dynamic parameters of TiTPA packed bed and calculated adsorbed amount of CH_4 from experimental breakthrough curves at different bed operating conditions

Total flow rate (mL/min)	Pressure (bar)	t_{pres} (min)	t_{break} (min)	t_{sat} (min)	t_{des} (min)	t_{cycle} (min)	H_{UNB} (cm)	τ_{CH4} (min)	q_{CH4} (mmolCH4/gTiTPA)
10	1	0	2	15	34	50	10.7	5	0.26
	5	14	14	24	51	93	4.7	18	0.89
	10	34	34	66	99	159	4.6	40	2.08
20	1	0	2	10	13	32	10.8	4	0.51
	5	7	7	17	26	48	6.5	9	1.51
	10	17	17	36	30	73	5.9	22	2.9
30	1	0	2	6	9	23	10.9	4	0.62
	5	5	5	12	17	37	6.6	7	1.78
	10	12	12	35	26	59	6.2	15	3.25

Table A.9. The dynamic parameters of TiTPA packed bed and calculated adsorbed amount of CO from experimental breakthrough curves at different bed operating conditions

Total flow rate (mL/min)	Pressure (bar)	t_{pres} (min)	t_{break} (min)	t_{sat} (min)	t_{des} (min)	t_{cycle} (min)	H_{UNB} (cm)	τ_{CO} (min)	q_{CO} (mmolCO/gTiTPA)
10	1	0	2	15	34	49	9.3	4	0.17
	5	14	14	24	51	89	6.0	13	0.56
	10	34	34	66	99	199	6.6	30	1.40
20	1	0	2	10	13	23	10.7	4	0.49
	5	7	7	17	26	50	7.1	8	0.90
	10	17	17	36	30	83	6.8	16	1.80
30	1	0	2	6	9	15	10.7	4	0.80
	5	5	5	12	17	34	7.2	6	1.15
	10	12	12	35	26	73	8.1	11	1.91

Table A.10. Langmuir and virial model parameters of pure CO_2, CH_4 and CO components on TiTPA at 303 K (Total feed flow: 30mL/min, bed pressure: 10 bar)

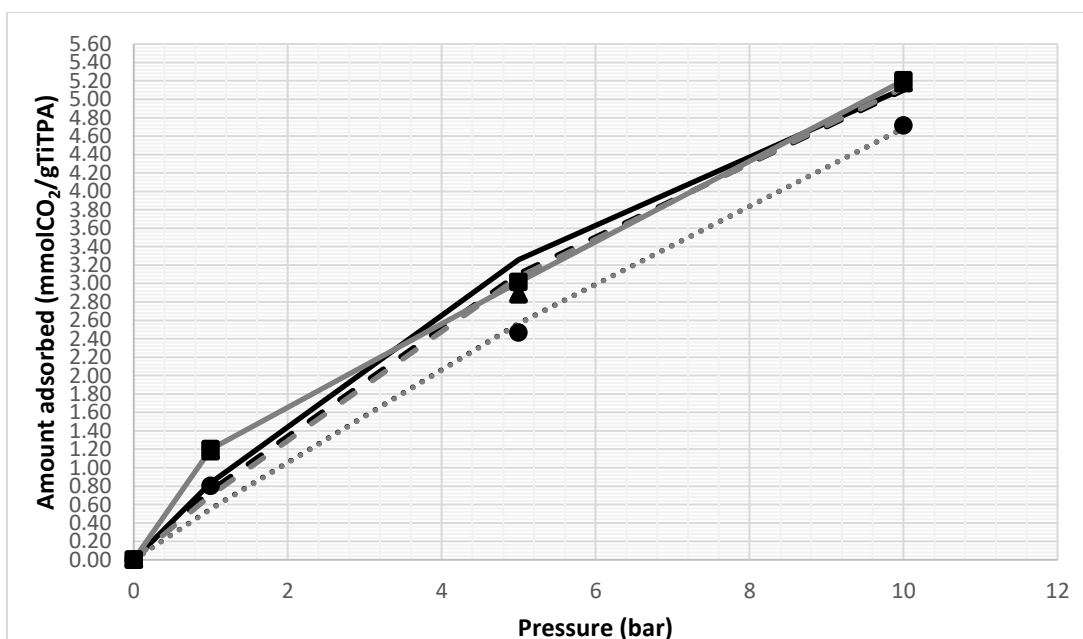|	Langmuir Model Parameters		
	CO_2	CH_4	CO
q_m (mmol/g)	11.872	11.640	6.404
$\propto$ (bar^{-1})	0.076	0.038	0.034
R^2	0.993	0.997	0.910
ERRSQ	0.239	0.208	0.151
	Virial Model Parameters		
	CO_2	CH_4	CO
H (mmol/gbar)	0.878	0.374	0.219
b	0.103	0.008	0.011
c	0	0.011	0
R^2	0.999	0.998	0.930
ERRSQ	0.02	0.003	0.273

Figure A.30. Adsorption isotherms of CO_2 on TiTPA at 303 K (Symbols: experimental data at CO_2/H_2 total flow rate of 10 mL/min (●), 20 mL/min (▲) and 30 mL/min (■); black lines: Langmuir model, grey lines: virial model applied for total feed flow rates of 10 mL/min: (·········), 20 mL/min: (-----) and 30 mL/min: (——))
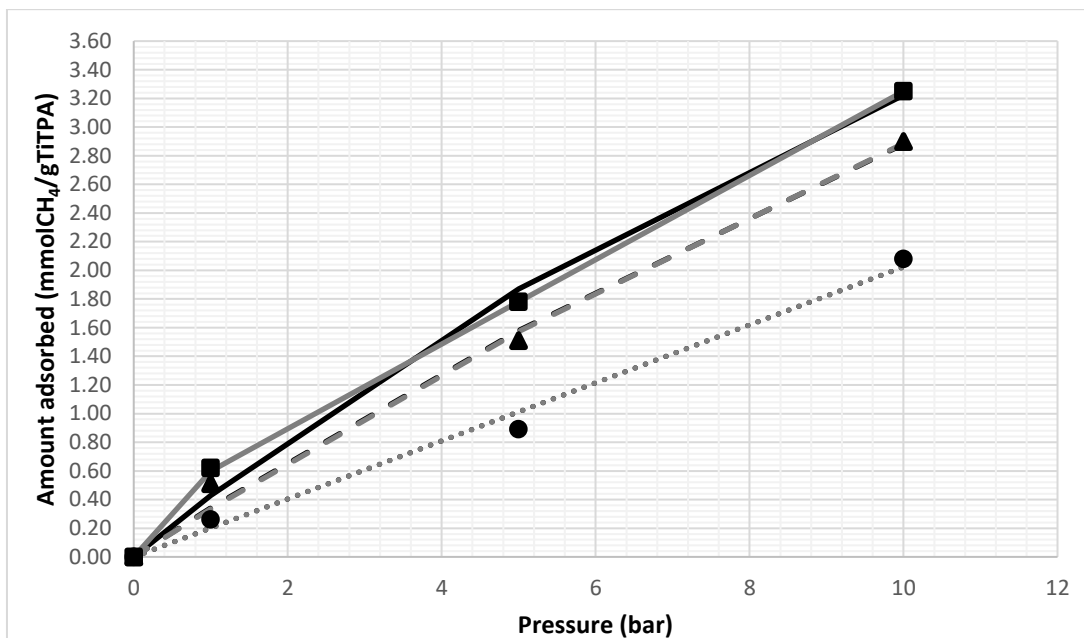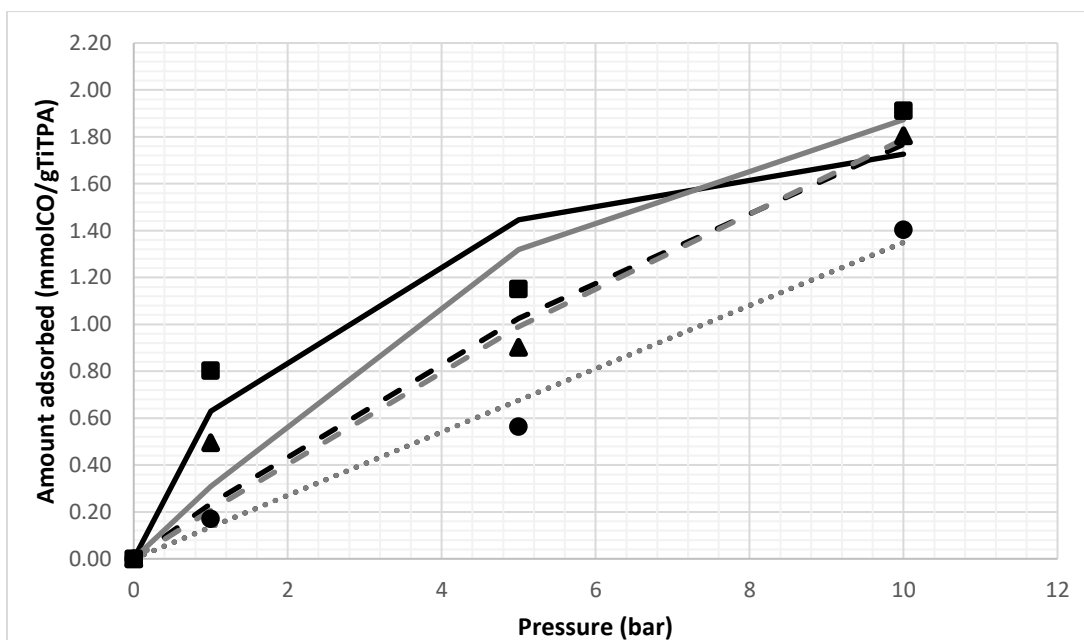
Figure A.31. Adsorption isotherms of CH₄ on TiTPA at 303 K (Symbols: experimental data at CH₄/H₂ total flow rate of 10 mL/min (●), 20 mL/min (▲) and 30 mL/min (■); black lines: Langmuir model, grey lines: virial model applied for total feed flow rates of 10 mL/min: (··········), 20 mL/min: (‐ ‐ ‐ ‐ ‐) and 30 mL/min: (——))

Figure A.32. Adsorption isotherms of CO on TiTPA at 303 K (Symbols: experimental data at CO/H₂ total flow rate of 10 mL/min (●), 20 mL/min (▲) and 30 mL/min (■); black lines: Langmuir model, grey lines: virial model applied for total feed flow rates of 10 mL/min (··········), 20 mL/min: (‐ ‐ ‐ ‐ ‐) and 30 mL/min: (——))
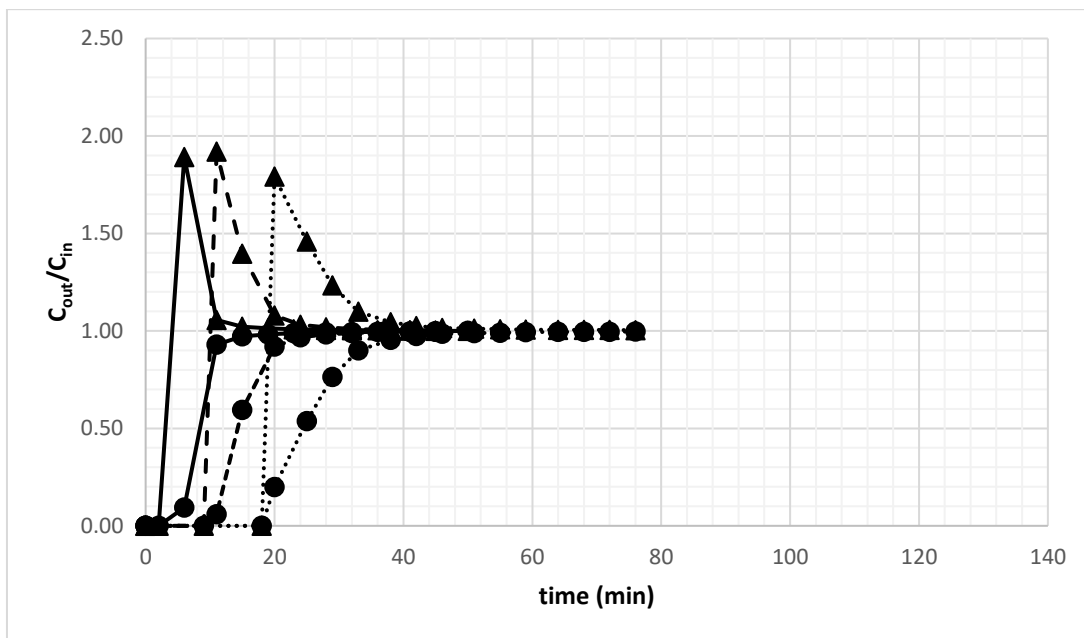
Figure A.33. Effect of pressure on CO_2 and CH_4 adsorption breakthrough curves over TiTPA (Total CO_2/CH_4 flow rate: 30 mL/min; CO_2: ● and CH_4: ▲; Bed pressures: 1bar (———), 5bar (-----) and 10bar (··········))

Figure A.34. Effect of pressure on CO_2 and CH_4 adsorption breakthrough curves over TiTPA (Total CO_2/CH_4 flow rate: 20 mL/min; CO_2: ● and CH4: ▲; Bed pressures: 1bar (———), 5bar (-----) and 10bar (··········))
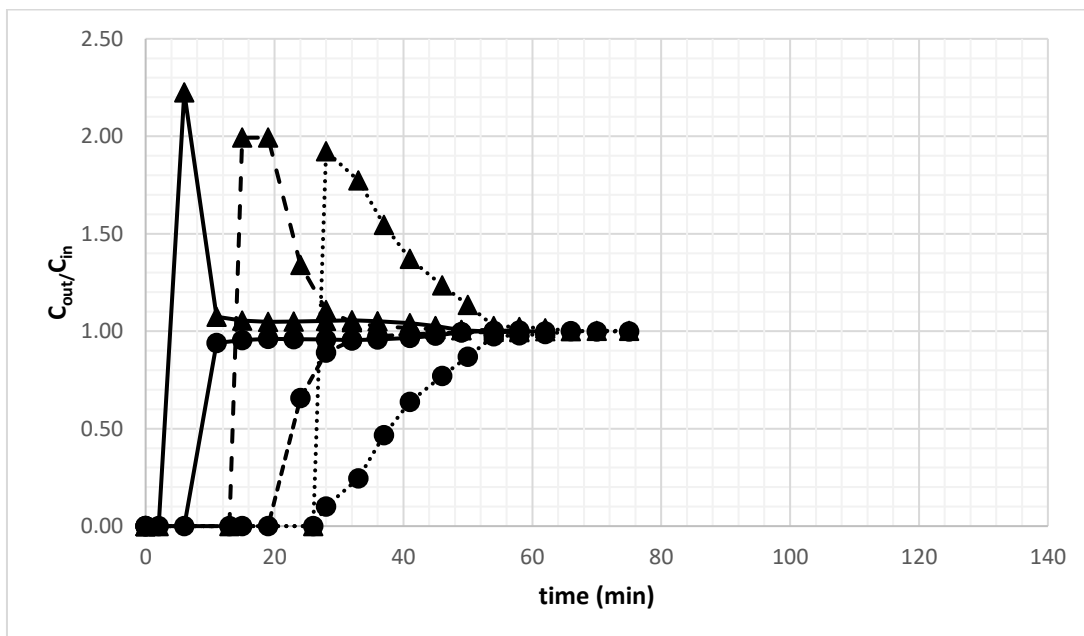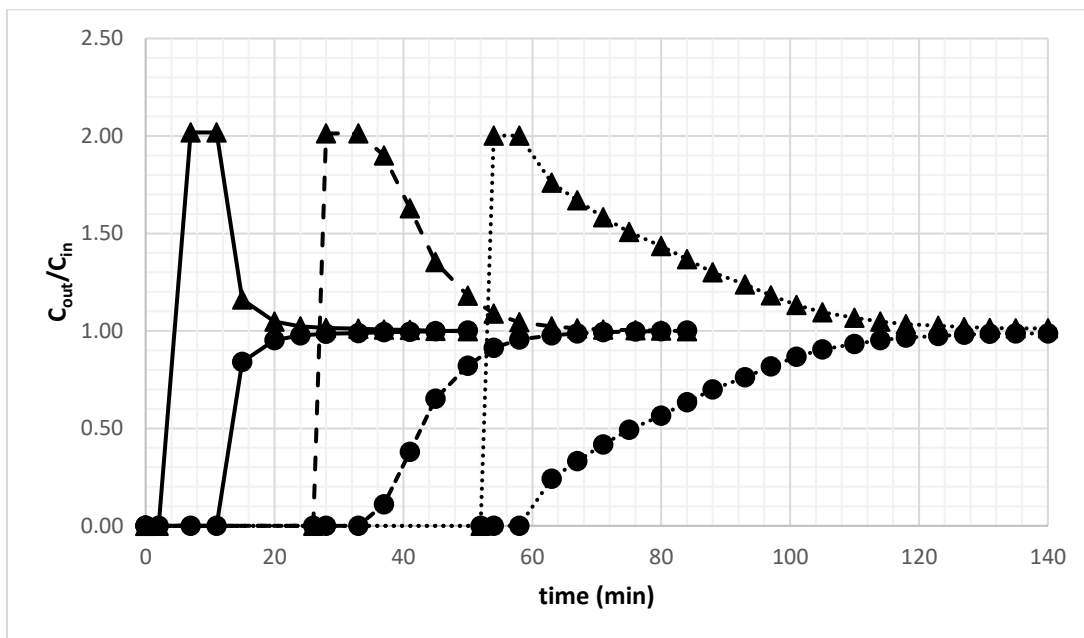
Figure A.35. Effect of pressure on CO_2 and CH_4 adsorption breakthrough curves over TiTPA (Total CO_2/CH_4 flow rate: 10 mL/min; CO_2: ● and CH_4: ▲, Bed pressures: 1bar (———), 5bar (- - - - -) and 10bar (··········))

Figure A.36. Effect of flow rate on CO_2 and CH_4 adsorption breakthrough curves over TiTPA (Bed pressure: 1 bar; Total CO_2/CH_4 flow rate: 30 mL/min (———), 20 mL/min (- - - - -) and 10 mL/min (··········))
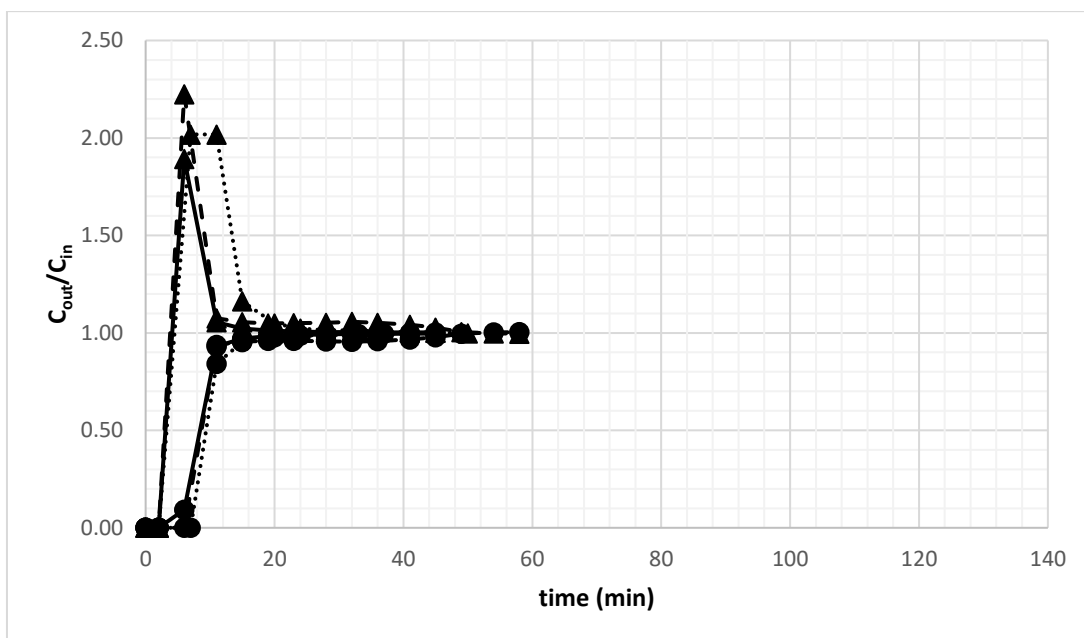
Figure A.37. Effect of flow rate on CO_2 and CH_4 adsorption breakthrough curves over TiTPA (Bed pressure: 5 bar; Total CO_2/CH_4 flow rate: 30 mL/min (———), 20 mL/min (‑ ‑ ‑ ‑) and 10 mL/min (··········))
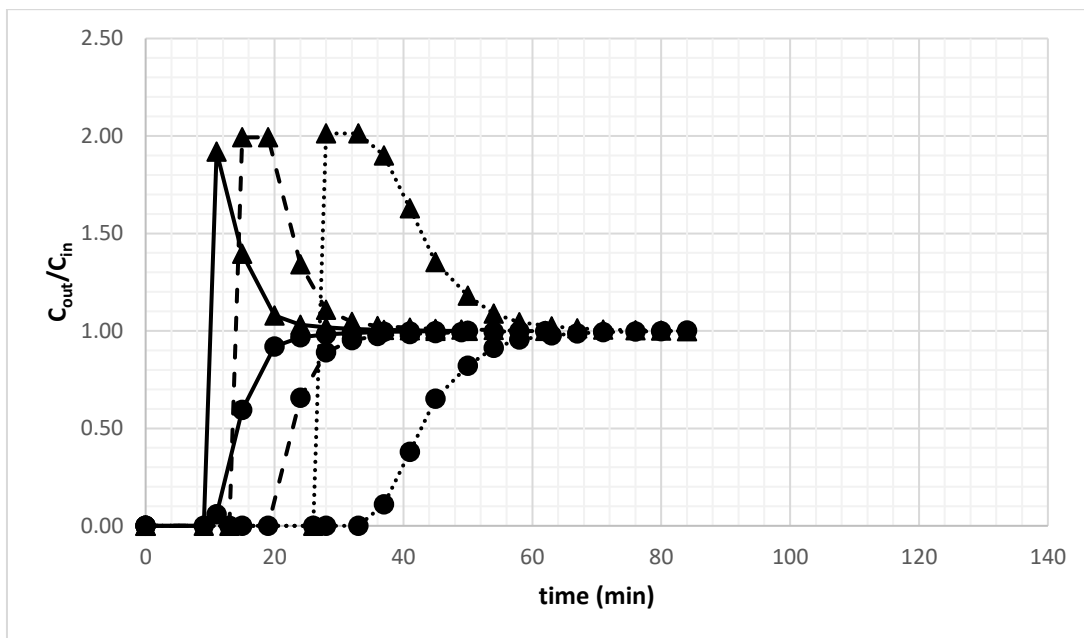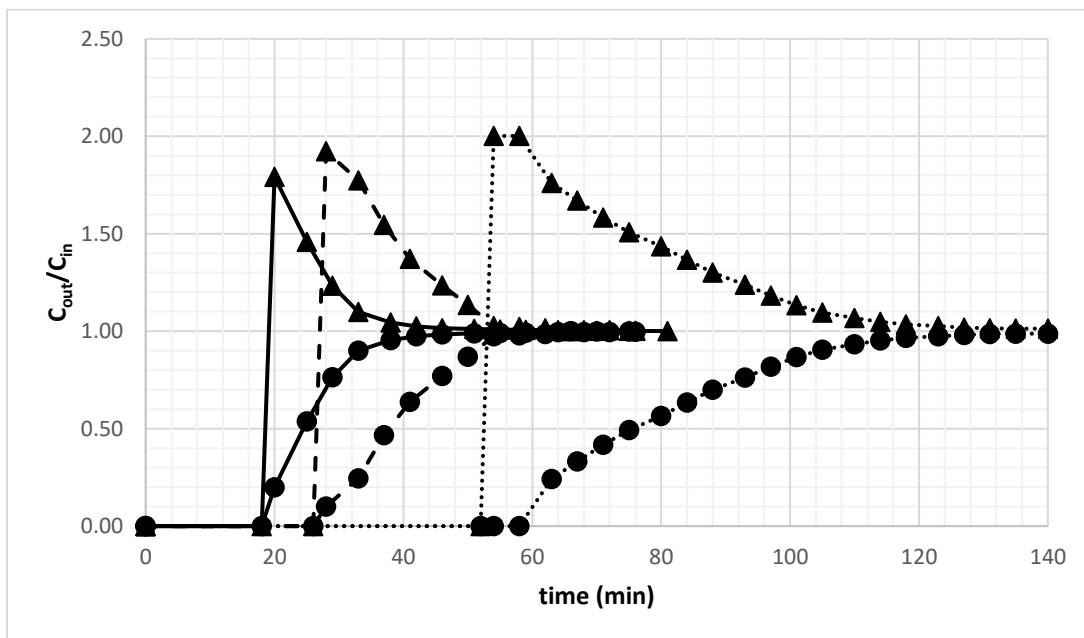

Figure A.38. Effect of flow rate on CO_2 and CH_4 adsorption breakthrough curves over TiTPA (Bed pressure: 10 bar; Total CO_2/CH_4 flow rate: 30 mL/min (———), 20 mL/min (‑ ‑ ‑ ‑) and 10 mL/min (··········))

Table A.11. Ideal and real selectivities of TiTPA for CO_2 over CH_4 at 303 K

Total flow rate (mL/min)	Pressure (bar)	Ideal Selectivity ($S_{CO2/CH4}$)	Real Selectivity ($S_{CO2/CH4}$)
10	1	3.1	8.0
	5	2.8	5.5
	10	2.3	3.7
20	1	2.3	6.9
	5	1.9	3.9
	10	1.8	2.6
30	1	2.0	5.3
	5	1.7	2.8
	10	1.6	2.1

Figure A.39. Molar percentages of CO_2 and H_2 effluent over ZnTPA at 303 K (Total CO_2/H_2 flow rate: 30 mL/min; CO_2: ● and H_2:▲; Bed pressures: 1bar (——), 5bar (- - - -), 10 bar (·········))

Figure A.40. Molar percentages of CH$_4$ and H$_2$ effluent over ZnTPA at 303 K (Total CH$_4$/H$_2$ flow rate: 30 mL/min; CH$_4$: ● and H$_2$:▲; Bed pressures: 1bar (———), 5bar (-----), 10 bar (·········))
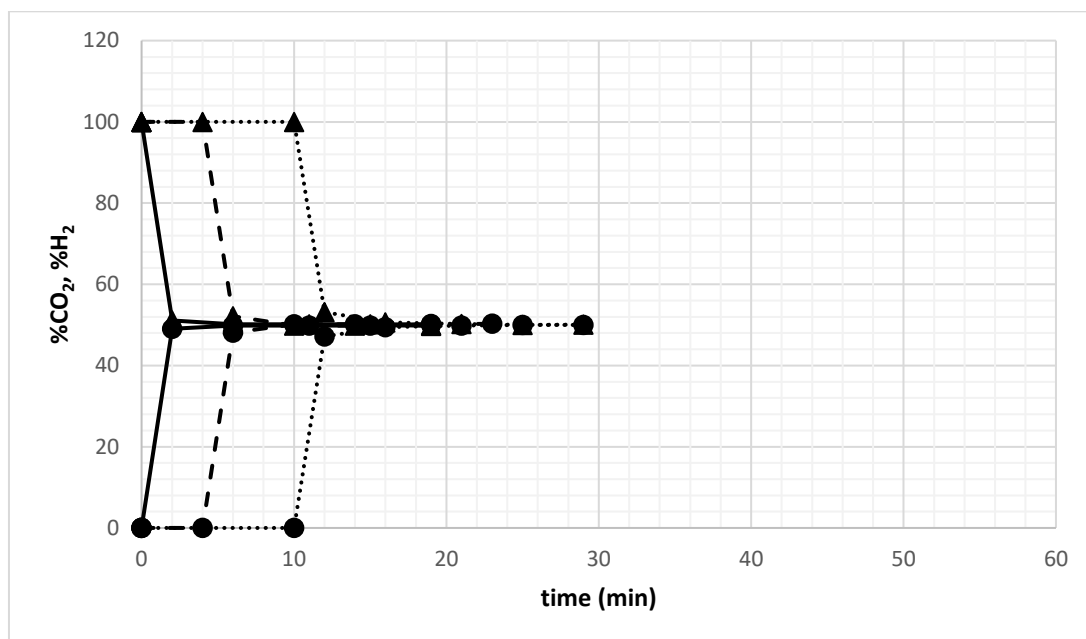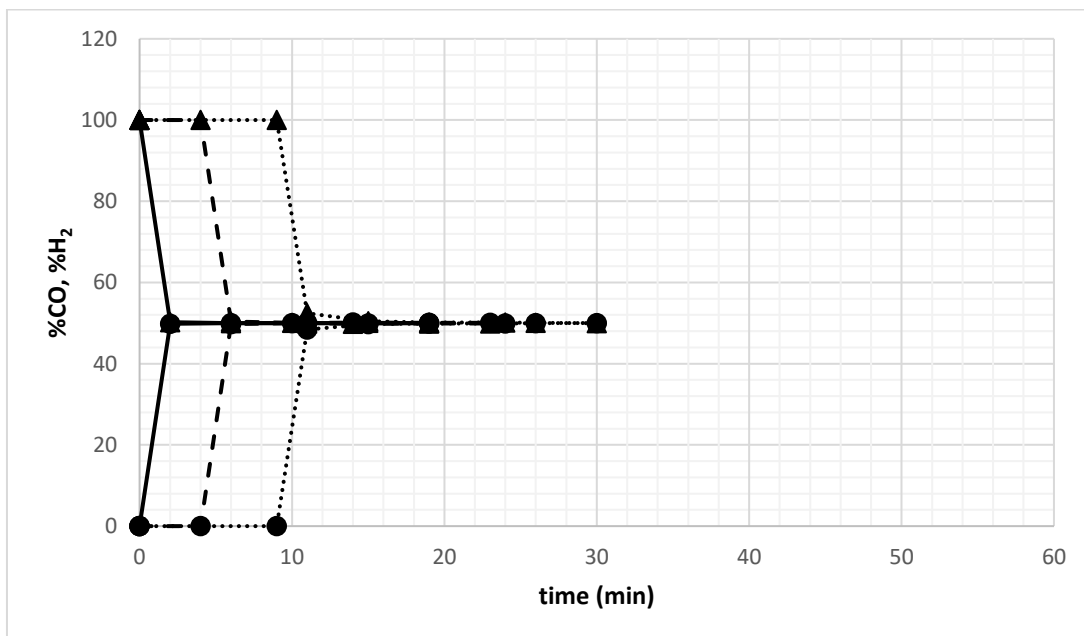

Figure A.41. Molar percentages of CO and H$_2$ effluent over ZnTPA at 303 K (Total CO/H$_2$ flow rate: 30 mL/min; CO: ● and H$_2$: ▲; Bed pressures: 1bar (———), 5bar (-----), 10 bar (·········))
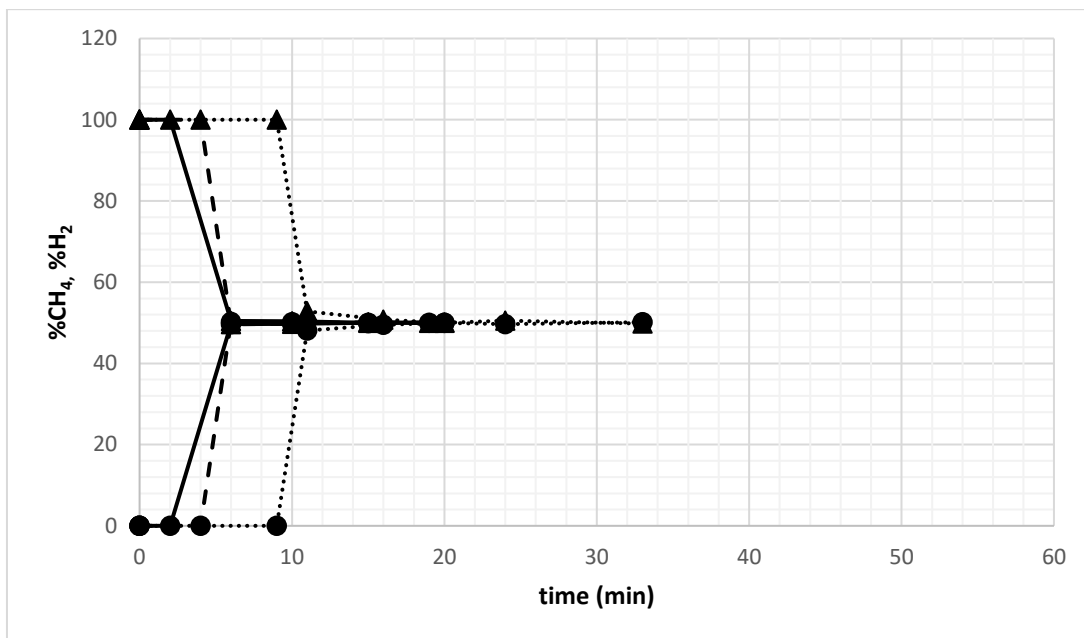
Figure A.42. CO$_2$ desorption curves over ZnTPA (He purge flow rate: 30 mL/min
(——), 20 mL/min (-----) and 10 mL/min (·········); Bed pressures: 1bar
(●), 5bar (■) and 10 bar (▲))

Figure A.43. CO desorption curves over ZnTPA (He purge flow rate: 30 mL/min
(——), 20 mL/min (-----) and 10 mL/min (·········); Bed pressures: 1bar
(●), 5bar (■) and 10 bar (▲))

Table A.12. The dynamic parameters of ZnTPA packed bed and calculated adsorbed amount of CO_2 from experimental breakthrough curves at different bed operating conditions
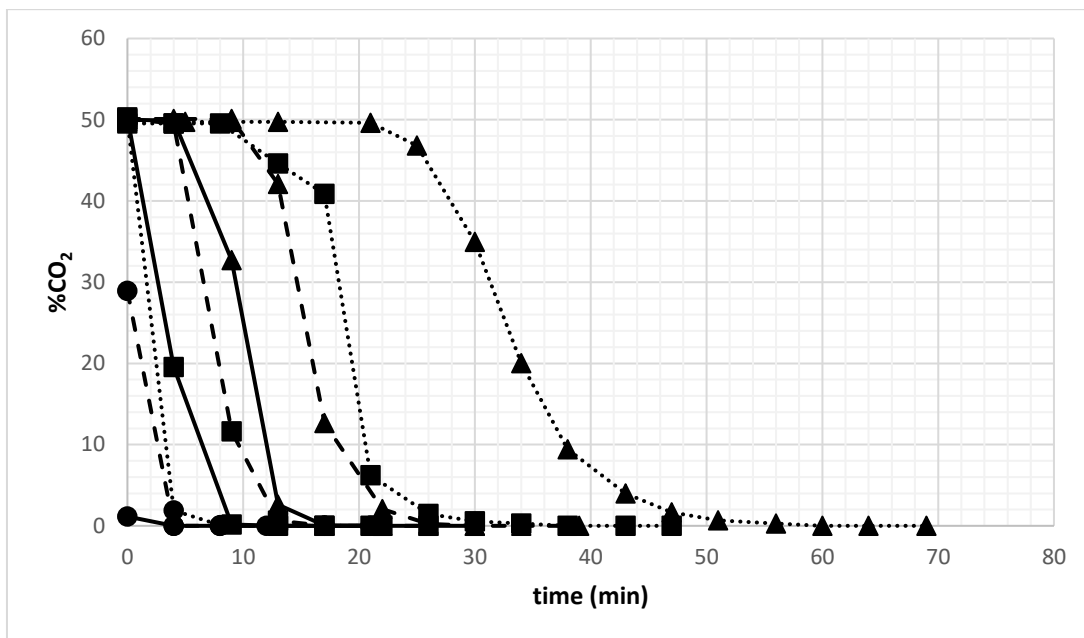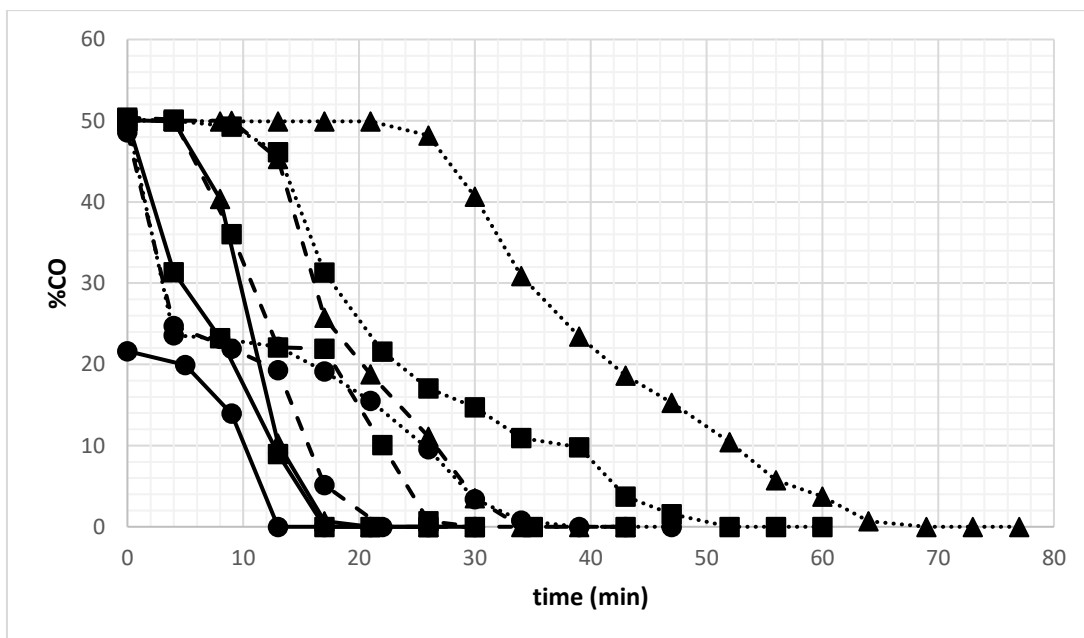
Total flow rate (mL/min)	Pressure (bar)	t_{pres} (min)	t_{break} (min)	t_{sat} (min)	t_{des} (min)	t_{cycle} (min)	H_{UNB} (cm)	τ_{CO2} (min)	q_{CO2} (mmolCO2/g)
	1	0	0	11	13	24	10.4	3	0.18
10	5	11	11	26	38	75	6.4	13	0.64
	10	22	22	41	60	123	5.3	19	0.90
	1	0	0	6	4	10	10.6	2	0.19
20	5	9	9	19	17	45	5.9	11	1.34
	10	14	14	25	30	69	5.0	15	1.81
	1	0	0	6	4	10	10.6	1	0.20
30	5	4	4	14	13	31	7.8	5	1.84
	10	10	10	21	22	53	5.9	11	2.11

Table A.13. The dynamic parameters of ZnTPA packed bed and calculated adsorbed amount of CH_4 from experimental breakthrough curves at different bed operating conditions

Total flow rate (mL/min)	Pressure (bar)	t_{pres} (min)	t_{break} (min)	t_{sat} (min)	H_{UNB} (cm)	τ_{CH4} (min)	q_{CH4} (mmolCH4/gZnTPA)
	1	0	0	6	7.3	4	0.16
10	5	10	10	20	5.6	12	0.59
	10	22	22	28	2.7	24	0.85
	1	0	0	6	10.6	1	0.15
20	5	6	6	17	7.1	7	0.85
	10	12	12	22	5.1	13	1.56
	1	0	0	2	10.8	1	0.19
30	5	4	4	6	3.8	5	1.82
	10	9	9	16	5.0	10	1.90

Table A.14. The dynamic parameters of ZnTPA packed bed and calculated adsorbed amount of CO from experimental breakthrough curves at different bed operating conditions

Total flow rate (mL/min)	Pressure (bar)	t_{pres} (min)	t_{break} (min)	t_{sat} (min)	t_{des} (min)	t_{cycle} (min)	H_{UNB} (cm)	τ_{CO} (min)	q_{CO} (mmolCO/gZnTPA)
10	**1**	0	0	6	39	45	10.6	2	0.08
	5	8	8	19	52	79	6.4	10	0.42
	10	27	27	37	69	133	3.3	32	0.73
20	**1**	0	0	6	22	28	10.7	1	0.13
	5	5	5	11	30	46	6.6	7	0.79
	10	13	13	19	34	66	3.7	14	1.46
30	**1**	0	0	2	13	15	10.8	1	0.18
	5	4	0	6	17	27	6.8	5	1.77
	10	9	9	15	21	45	4.6	10	1.83

Table A.15. Ideal selectivity of ZnTPA for CO_2 over CH_4 at 303 K

Total flow rate (mL/min)	Pressure (bar)	Ideal Selectivity ($S_{CO2/CH4}$)
10	**1**	1.20
	5	1.08
	10	1.38
20	**1**	1.27
	5	1.37
	10	1.16
30	**1**	1.05
	5	1.00
	10	1.11

Table A.16. Langmuir and virial model parameters of pure CO_2, CH_4 and CO components on ZnTPA at 303 K (Total feed flow: 30mL/min, bed pressure: 10 bar)

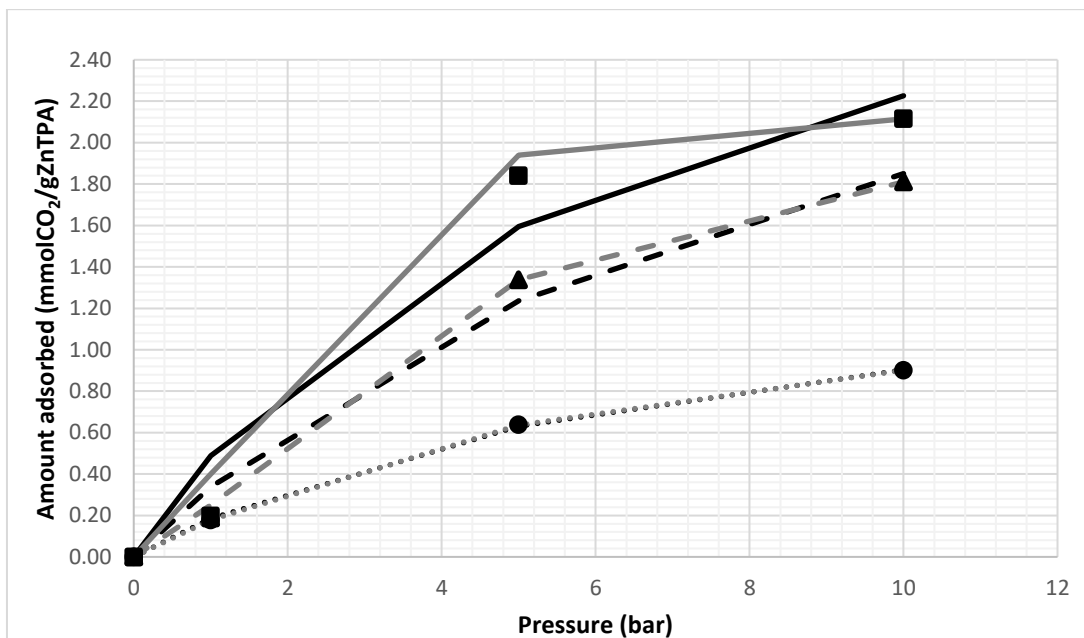|	**Langmuir Model Parameters**		
	CO_2	**CH_4**	**CO**
q_m (mmol/g)	3.664	3.112	3.004
$\propto$ (bar^{-1})	0.154	0.190	0.192
R^2	0.980	0.967	0.967
ERRSQ	0.157	0.220	0.224
	Virial Model Parameters		
	CO_2	**CH_4**	**CO**
H (mmol/gbar)	0.680	0.403	0.189
b	0.125	0.017	0.005
c	0.138	0.340	0.007
R^2	0.996	0.995	0.994
ERRSQ	0.050	0.055	0.060

Figure A.44. Adsorption isotherms of CO_2 on ZnTPA at 303 K (Symbols: experimental data at CO_2/H_2 total flow rate of 10 mL/min (●), 20 mL/min (▲) and 30 mL/min (■); black lines: Langmuir model, grey lines: virial model applied for total feed flow rates of 10 mL/min: (⋯⋯⋯), 20 mL/min: (−−−−) and 30 mL/min: (———))
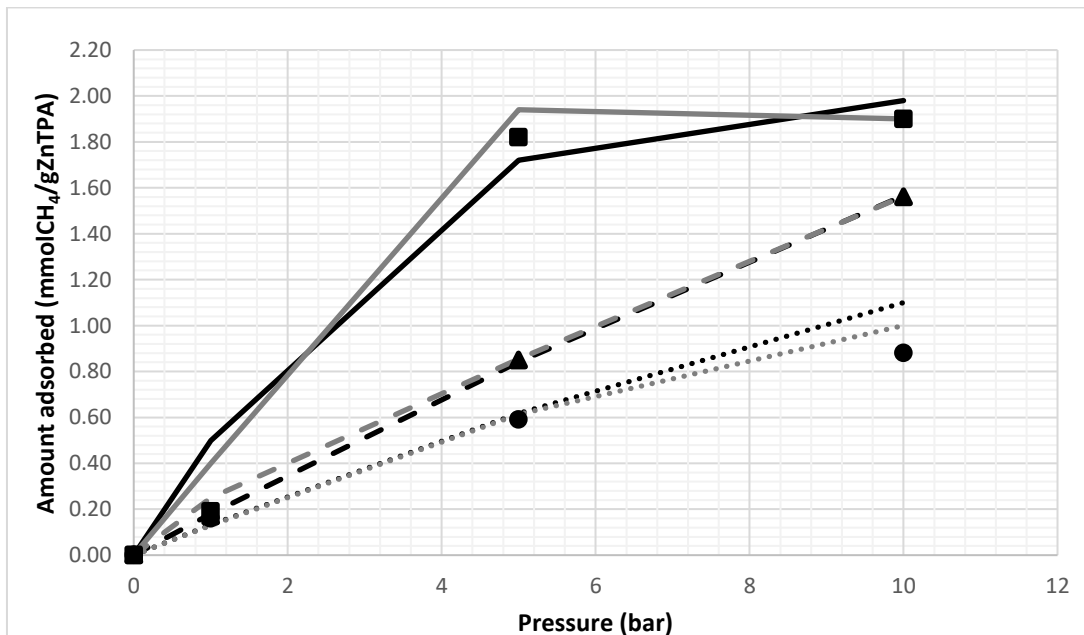

Figure A.45. Adsorption isotherms of CH_4 on ZnTPA at 303 K (Symbols: experimental data at CH_4/H_2 total flow rate of 10 mL/min (●), 20 mL/min (▲) and 30 mL/min (■); black lines: Langmuir model, grey lines: virial model applied for total feed flow rates of 10 mL/min: (⋯⋯⋯), 20 mL/min: (−−−−) and 30 mL/min: (———))
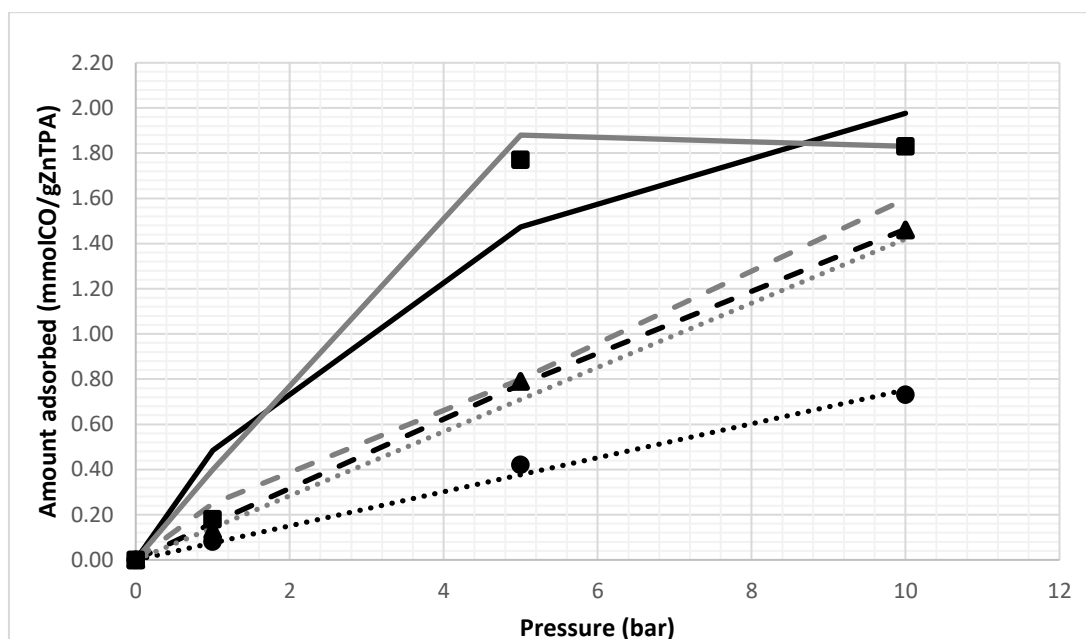
Figure A.46. Adsorption isotherms of CO on TiTPA at 303 K (Symbols: experimental data at CO/H$_2$ total flow rate of 10 mL/min (●), 20 mL/min (▲) and 30 mL/min (■); black lines: Langmuir model, grey lines: virial model applied for total feed flow rates of 10 mL/min (·········), 20 mL/min: (------) and 30 mL/min: (———))